4

MEMS& BioMEMS

Table of Contents

Superhydrophilic and Superhydrophobic Nanostructured Surfaces for Microfluidics and Thermal Management

R. Xiao, K. Chu, E.N.Wang

Nanostructured features can be used to magnify the intrinsic hydrophobicity or hydrophilicity of a material to create superhydrophobic and superhydrophilic surfaces [1, 2]. There has been particular interest in these surfaces for a variety of applications including self-cleaning and drag reduction with superhydrophobic surfaces [3-5]. Superhydrophilic surfaces are of interest in anti-fogging and thermal management [6-8]. Past work has demonstrated significant changes in contact angle with minimal hysteresis with the introduction of nanostructured surface features [9]. Current efforts, however, focus on the dynamic robustness and spreading of liquids on such surfaces

We have fabricated silicon pillar arrays with cross sections of 500 nm × 500 nm, spacings between pillars of 800 nm, and heights of 5 μm (Figure 1). The pillar arrays are naturally oxidized in air to make them hydrophilic. The interaction of the spreading liquid with the fabricated pillars was studied using diffraction limited microscopy and with an environmental scanning electron microscope (Figure 2). The preliminary data (Figure 2) shows that the liquid-air interface is pinned diagonally. Using an energy minimization approach, theory is currently being developed to understand the effect of pillar spacing, height, and diameter on spreading dynamics. We have also concurrently coated the silicon pillars with a silane chemistry to create superhydrophobic surfaces. The effect of shape and size of the nanostructures on hydrophobic robustness is currently being investigated.

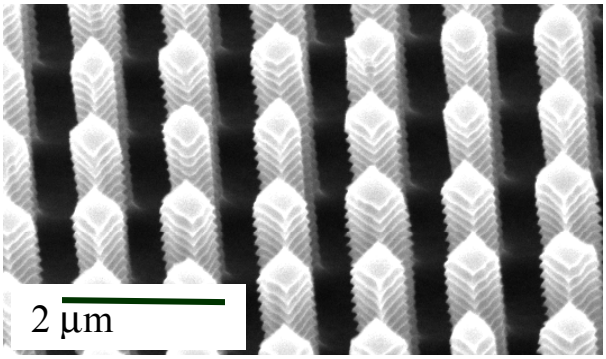

▲ Figure 1: Scanning electron micrograph of a silicon nanopillar array where the side length of the pillars is 500 nm, spacing between pillars is 800 nm, and height of the pillar is 5 μm. Due to the deep reactive etching process, scallops of tens of nanometers are present along the side walls of the pillars.

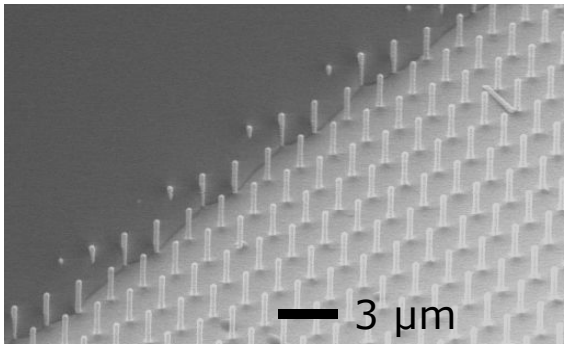

▲ Figure 2: Scanning electron micrograph of liquid spreading on a superhydrophilic surface. The contact line is pinned diagonally.

References

[1] W. Barthlott, C. Neinhuis, "Purity of the sacred lotus, or escape from contamination in biological surfaces," *Planta*, vol. 202, no. 1, pp. 1-8, 1997.
[2] R.D. Hazlett, "Fractal applications: Wettability and contact angle," *Journal of Colloid Interface Sci*ence, vol. 137, no. 2, pp. 527, 1990.
[3] N.A. Patankar, "Transition between superhydrophobic states on rough surfaces," *Langmuir*, vol. 20, no. 17, pp. 7097-7102, 2004.
[4] Z. Yoshimitsu, A. Nakajima, T. Watanabe, K. Hashimoto, "Effects of surface structure on the hydrophobicity and sliding behavior of water droplets," *Langmuir*, vol. 18, no. 15, pp. 5818-5822, 2002.
[5] J. Jopp, H. Grull, and R. Yerushalmi-Rozen, "Wetting behavior of water droplets on hydrophobic microtextures of comparable size," *Langmuir*, vol. 20, no. 23, pp. 10015-10019, 2004.
[6] A. Fujishima, D.A. Tryk, T. Watanabe, and K. Hashimoto, "Self-cleaning glass," *International Glass Review—Flat Glass Processing*, no. 2, pp. 114-6, 1998.
[7] Y. Takata, K. Tanaka, K. Kaijima, T. Ito, T. Watanabe, and M. Shimohigoshi, "Enhancement of heat transfer with liquid-vapor phase change by photo-induced hydrophilicity, " in *Proc. of the 33rd National Heat Transfer Conference (CD-ROM)*. Albuquerque, NM, 1999.
[8] Y. Takata, K. Tanaka, K. Kaijima, T. Ito, T. Watanabe, and M. Shimohigoshi, "Enhancement of boiling and evaporation heat transfer by superhydrophilic photocatalyst," in *Proc. of the 6th UK National Conference on Heat Transfer*, Edinburgh, UK. 1999, pp. 323-8.
[9] C. Extrand, "Model for contact angles and hysteresis on rough and ultraphobic surfaces," *Langmuir*, vol. 18, pp. 7991-7999, 2002.

Design of a Micro-breather for Venting Vapor Slugs in Two-phase Microchannels

B. Alexander, E. Wang

Sponsorship: Department of Mechanical Engineering, Intel Higher Education grant, Northrop Grumman Corporation

Boiling is currently used in a variety of industries as an efficient method of cooling. Boiling, and phase-change in general, are attractive because the latent heat of vaporization can be used to carry and dissipate large heat fluxes. Two-phase microchannels have been of recent interest because they promise compact and efficient solutions [1].

However, phase-change in microchannels leads to challenges that are not present in macroscale counterparts because the governing forces are different. Surface tension forces become dominant at the microscale whereas buoyancy forces can be neglected. As a result, flow instabilities, large pressure fluctuations, and local liquid dry-out occur in microchannels, which severely limits the overall thermal performance.

To address these problems, a few solutions have been proposed [2, 3], including the use of porous membranes or hydrophobic ports that allow vapor bubbles to escape from the microchannels as they form. The proposed solutions have drawbacks, including the inability to sufficiently remove vapor bubbles effectively and eliminate dry-out within the channels.

We propose a design for a microscale breathing device that uses the combination of surface chemistry and geometry to separate vapor from a liquid flow. To better understand the physics and governing parameters for the microscale breather, we designed a test device that allows for cross-sectional visualization of a breathing microchannel (Figure 1). We have conducted various experiments and collected image data to help direct our vapor breather design to achieve high vapor removal efficiencies with minimal fabrication effort and control requirements (Figure 2).

The successful implementation of a microchannel with an efficient breather will allow for new cooling technologies with higher heat removal capacities that can be effectively used by the semiconductor industry. The breathers also have significant promise as liquid vapor separators for use in micro-fuel cells and other applications that require phase separation at the microscale.

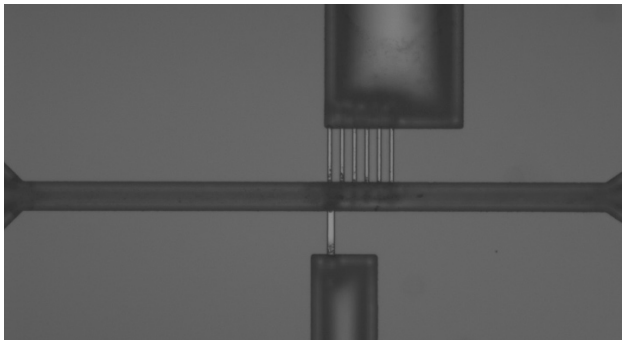

▲ Figure 1: Image of the entire breathing test device under low magnification. The entry and exit portions of the channel are visible at both ends of the picture. The breathing structure is above the main channel near the center of the image, and the air inlet is below the main channel near the center of the image.

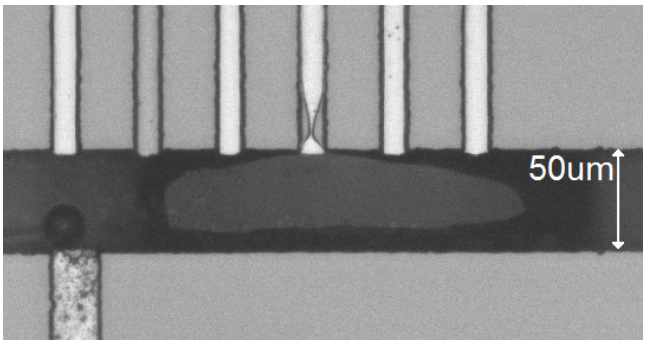

▲ Figure 2: Image of a gas bubble breathing in the channel. The gas slug is attached to the breathing structure and venting as more gas is added from the air inlet port just upstream (bottom left of image).

References

[1] J. Thome, "The new frontier in heat transfer: Microscale and nanoscale technologies," *Heat Transfer Engineering*, vol. 27, no. 9, pp. 1-3, 2006.

[2] D. Meng and C. Kim, "Self-aligned micro bubble arrays by using surface tension," in *Proc. of ASME International Mechanical Engineering Congress and Exposition*, 2004.

[3] A. Kosar, C. Kuo, and Y. Peles, "Suppression of boiling flow oscillations in parallel microchannels by inlet restrictors," *Journal of Heat Transfer*, vol. 128, pp. 251-260, Mar. 2006.

Microfluidic Patterning of P-Selectin for Cell Separation through Rolling

S. Bose, S. Hong, R.S. Langer, J.M. Karp, R. Karnik
Sponsorship: NIH

Cell separation based on markers present on the cell surface has extensive biological applications. However, current separation methods involve labeling cells and label removal steps that are often slow and intrusive. Recently, we discovered that it is possible to steer cells interacting transiently with the surface through patterning of receptors on the surface [1]. In this paper we report microfluidic patterning of P-selectin receptors to control cell rolling for label-free separation of cells. We envision a microfluidic device that would perform label-free separation of cells by rolling them on receptor patterned surfaces (Figure 1). The present work is the first step towards realizing these devices.

A microchannel defining the pattern was fabricated in PDMS and reversibly bonded onto a polystyrene substrate. Human P-Selectin was filled inside the microchannel and left overnight for physisorbtion to complete. Later the PDMS mask was removed, and the surface was washed with PBS and finally incubated in Fetal Bovine Serum to block non-specific interactions. HL-60 myeloid cell suspension was flowed over the surface to verify patterning of P-selectin. We observed that cells interacted selectively with the P-selectin region, showing that the patterning technique was successful (Figure 2). Rolling was clearly observed on the selectin-coated bands and some deflection of cells at the edge was also observed. A few cells were also seen to detach from one band and reattach at another selectin band downstream.

This work demonstrates microfluidic patterning of P-selectin that is essential for a device for cell separation based on cell rolling. In the future, these patterns will be incorporated in a smaller microfluidic flow chamber with multiple inlets and outlets for label-free, continuous-flow cell separation.

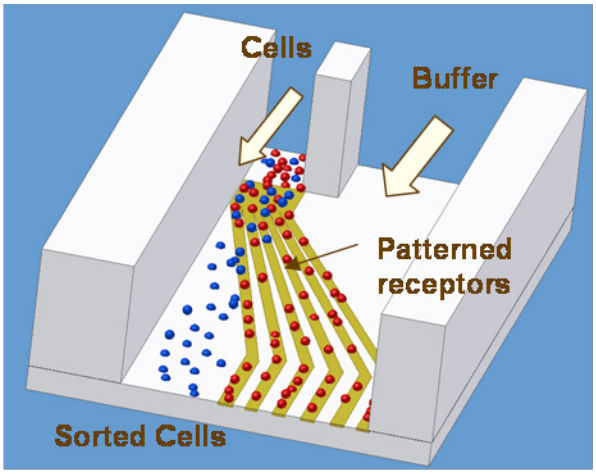

▲ Figure 1: Schematic of the proposed cell separation device. Cells are introduced from one side in a buffer flow. Rolling of cells on patterned receptors causes them to separate laterally, from where they can be collected in different conduits.

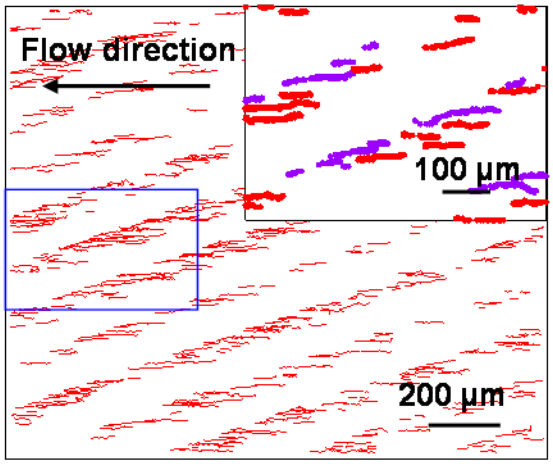

▲ Figure 2: Tracks of HL-60 cells rolling on P-selectin patterns. Closer observation (magnified inset showing selected tracks) shows that some cells get slightly deflected before detaching from the P-selectin regions.

References

[1] R. Karnik, S. Hong, H. Zang, Y. Mei, D. Anderson, J. Karp, and R. Langer, "Nanomechanical control of cell rolling in two dimensions through surface patterning of receptors," *Nano Letters 8*, 2008, to be published.

Electrical Detection of Fast Reaction Kinetics in Nanochannels with an Induced Flow

L.F. Cheow, R.B. Schoch, J. Han

Sponsorship: DuPont-MIT Alliance, NIH

Nanofluidic channels can be used to enhance surface binding reactions, since the target molecules are closely confined to the surfaces that are coated with specific binding partners. Moreover, diffusion-limited binding can be significantly enhanced if the molecules are steered into the nanochannels via either pressure-driven or electrokinetic flow. Monitoring the nanochannel impedance, which is sensitive to surface binding, has led to electrical detection of low analyte concentrations in nanofluidic channels within response times of 1-2 h [1]. This finding represents a ~54 fold reduction in the response time using convective flow compared to diffusion-limited binding [2]. At high flow velocities, the presented method of reaction kinetics enhancement is potentially limited by force-induced dissociations of the receptor-ligand bonds [3]. Optimization of this scheme could be useful for label-free, electrical detection of biomolecule binding reactions within nanochannels on a chip.

We acknowledge MTL for support during the fabrication process.

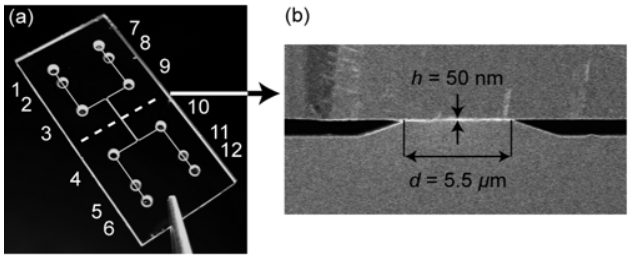

▲ Figure 1: Design of the device, consisting of two microchannels joined by nanochannels. (a) Photograph of the 12 × 25 mm chip showing the two microchannels and access holes. (b) The cross-sectional view along the dotted line, with a scanning electron microscope image showing two microchannels (with electrodes at their bottom) which are connected by nanochannels with height h = 50 nm and length d = 5.5 μm.

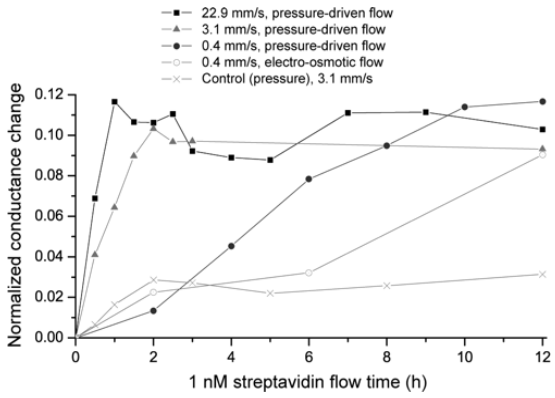

▲ Figure 2: Decrease of the response time of 1 nM streptavidin from ~12 to ~1 h by increasing the flow velocity through the nano-channel, presented by the normalized conductance change vs. streptavidin flow time. The control measurement was made with a 1-nM streptavidin solution and a protein-resistant channel coating under pressure-driven flow. The connecting lines are for guidance only.

References

[1] R.B. Schoch, L.F. Cheow, and J. Han, "Electrical detection of fast reaction kinetics in nanochannels with an induced flow," *Nano Letters*, vol. 7, no. 12, pp. 3895-3900, Nov. 2007.

[2] R. Karnik, K. Castelio, R. Fan, P. Yang, and A. Majumdar, "Effects of biological reactions and modifications on conductance of nanofluidic channels," *Nano Letters*, vol. 5, no. 9, pp. 1638-1642, July 2005.

[3] A. Pierres, D. Touchard, A.M. Benoliel, and P. Bongrand, "Dissecting Streptavidin-biotin interaction with a laminar flow chamber," *Biophysics Journal*, vol. 82, no. 6, pp. 3214-3223, June 2002.

Integration of Actuated Membranes in Thermoplastic Microfluidic Devices

K.S. Lee, R.J. Ram
Sponsorship: NSF

PolyDiMethylSiloxane (PDMS) is a common material for fabrication of microfluidic devices. Elasticity provided by PDMS enables the creation of active devices that utilize pressurized membranes such as pumps and mixers. However, for structures requiring dimensional stability, rigidity, or disposability, plastics have the required properties [1]. Plastics can be manufactured using mass fabrication technologies such as injection molding and hot embossing with established bonding processes [2], but at the cost of sacrificing active device functionality. A new fabrication process combining plastic substrates with PDMS membranes enables the creation of active microfluidic devices inside dimensionally stable systems, merging the functionality of PDMS with established plastic fabrication technologies.

Irreversible bonding between PDMS and plastics for fluidics requires interfaces that can handle high pressure and harsh chemical environments. Hydrolytic stability under acidic or basic conditions is particularly important. Direct bonding between PMMA and PDMS has been explored [3], but interfaces withstood only 2.5 psi before failure. Surface modification of polycarbonate and PMMA surfaces with AminoPropylTriEthoxySilane (APTES) [4] has also been shown to enable PDMS plasma bonding [5], but no data on hydrolytic stability was shown.

To improve hydrolytic stability, two additional silanes were explored, BisTriEthoxySilylEthane (BTESE) and Bis(TriMethoxySilylPropyl) Amine (BTMSPA), for thin and thick primer coatings, respectively. Devices with PDMS membranes suspended over 25-µL fluid reservoirs were fabricated in PC and PMMA to test interface robustness. For all devices, membrane ruptures occurred instead of delamination at 60 psi, making the devices suitable for active valves. Blisters were then subjected to NaOH and HCl solutions from the PDMS side at 70 C for 2 hours, followed by pressure testing. Figure 1 shows that hydrolytic stability improves over APTES with addition of BTMSPA to the primer solution for thick coatings or BTESE for monolayer coatings. A test chip containing peristaltic pumps and mixers was then fabricated, and pump rate versus frequency was measured as shown in Figure 2.

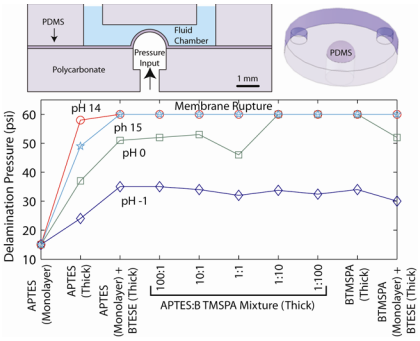

▲ Figure 1: Schematic of the aqueous blister test structure utilized to test hydrolytic bond failure. PDMS membranes were 70 µm thick over 915-µm-diameter circles. Plot of the delamination pressure versus primer type at pH extremes. Hydrolytic stability increases with addition of BTMSPA or protection by BTESE.

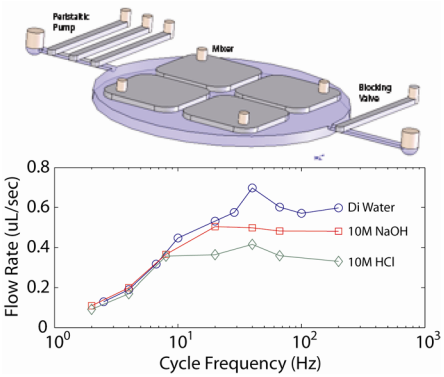

▲ Figure 2: Schematic of the test device fabricated in PC with a 70-µm PDMS membrane for pressure based actuation. Flow rate versus frequency for different pH at 15 psi for an 800x600 μm^2 cross-section membrane-based peristaltic pump is plotted. Performance degradation at higher frequencies most likely results from valve sticking due to acid/base induced modification of the PDMS and silane surfaces.

References

[1] H. Becker and C. Gartner, "Polymer microfabrication technologies for microfluidic systems," *Analytical Bioanalytical Chemistry*, vol. 390, pp. 89-111, 2008.

[2] L. Brown, T. Koerner, J.H. Horton, and R.D. Oleschuk, "Fabrication and characterization of poly(methylmethacrylate) microfluidic devices bonded using surface modifications and solvents," *Lab on a Chip*, vol. 6, pp. 66-73, 2006.

[3] W.W.Y. Chow, K.F. Lei, G. Shi, W.J. Li, and Q. Huang, "Micro fluidic channel fabriation by PDMS-interface bonding," *Smart Materials and Structures*, vol. 15, pp. S112-S116, 2006.

[4] C. Li and G.L. Wilkes, "The mechanism for 3-aminopropyltriethoxysilane to strengthen the interface of polycarbonate substrates with hybrid organic-inorganic sol-gel coatings," *Journal of Inorganic Organometallic Polymers*, vol. 7, pp. 203-215, 1997.

[5] M.E. Vlachopoulou, A. Tserepi, and K. Misiakos, "A novel process for irreversible bonding of PDMS and PMMA substrates," *MNE'06 Micro- and Nano- Engineering*, 2006.

Teflon Films for Chemically-inert Microfluidic Valves and Pumps

W.H. Grover, M.G. von Muhlen, S.R. Manalis
Sponsorship: NIH, ARO

Like transistors in electronic microprocessors, microfluidic valves and pumps are the fundamental elements of logic and control in many lab-on-a-chip devices. Flexible elastomers make good candidates for the moving parts in valves and pumps, and elastomers like polydimethylsiloxane (PDMS) have found widespread use in a variety of normally-open and normally-closed microfluidic valves. Unfortunately, the limited chemical compatibility of PDMS has complicated its use in many microfluidic applications. Many chemicals commonly used in organic synthesis readily swell PDMS devices or dissolve PDMS oligomers from the elastomer. Small hydrophobic molecules readily partition into and out of bulk PDMS, complicating the determination of their on-chip concentration. Some reusable glass microfluidic devices must be equipped with removable, disposable valves because the PDMS valves would be destroyed by the harsh acid used to clean the device before reuse. For these reasons, a large variety of interesting and useful chemistries may be unsuitable for use in native PDMS devices.

We have developed a simple alternative method for fabricating Teflon monolithic membrane valves and pumps in glass microfluidic devices [1]. We have found that inexpensive, commercially-available fluorinated ethylene-propylene (FEP) Teflon films can be bonded between etched glass wafers to form chemically-inert monolithic membrane valves and pumps. Both FEP and polytetrafluoroethylene (PTFE) are comprised entirely of carbon and fluorine and are similarly inert. But while PTFE is opaque and must be cut or skived to make rough thin sheets, FEP is transparent and available as a smooth, uniform thin film. Chemical compatibility data from nearly 50 years of use as a commercial product show that FEP is resistant to virtually all chemicals except "molten alkali metals, gaseous fluorine, and certain complex halogenated compounds such as chlorine trifluoride at elevated temperatures and pressures."[2] The resulting glass-FEP-glass devices are optically transparent and suitable for imaging or fluorescence applications (Figures 1, 2). The FEP Teflon valves permit unimpeded (0.9 µL/s) flow while open and negligible (< 250 pL/s) leakage while closed against 14 kPa fluid pressure. The FEP pumps can precisely meter nanoliter-scale volumes at up to microliter/second rates. The pumps also show excellent long-term durability with < 4% change in pumping rate after 13 days of continuous operation. By combining ease of fabrication with extreme chemical inertness, these Teflon monolithic membrane valves and pumps enable research involving a vast array of chemistries that are incompatible with native PDMS microfluidic devices.

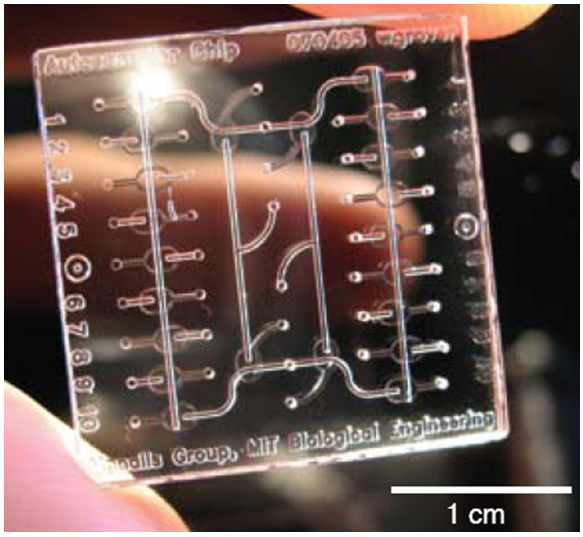

▲ Figure 1: Photograph of an Autosampler Chip containing 22 monolithic membrane FEP Teflon valves. The Autosampler Chip can deliver extremely caustic piranha solution (concentrated sulfuric acid and hydrogen peroxide) to clean an off-chip sensor without causing any detectable damage to the chip or its valves.

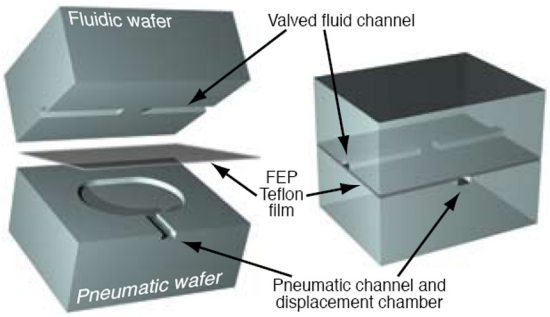

▲ Figure 2: Exploded and assembled illustrations of a single FEP valve.

References

[1] W.H. Grover, M.G. von Muhlen, and S.R. Manalis, "Teflon films for chemically-inert microfluidic valves and pumps," *Lab on a Chip*, vol. 8, pp. 913-918 May 2008.
[2] DuPont. (2008). FEP Fluorocarbon Film Properties Bulletin. [Online] Available: http://www2.dupont.com/Teflon_Industrial/en_US/assets/downloads/h55008.pdf.

Nanofluidic System for Single-particle Manipulation and Analysis

Y.H. Sen, R. Karnik
Sponsorship: MIT

Nanopores are versatile sensors for detection of single molecules and particles in solution. When a molecule passes through a nanopore with a voltage bias applied across it, the resulting transient blockage of the nanopore yields a detectable current change that enables single-molecule sensing [1, 2]. Different molecules may exhibit different current blockage and duration profiles, which may be used to characterize the molecules. However, the sensing ability of nanopores is often limited by the quick transit times of molecules through the nanopore that result in poor signal-to-noise ratio. To address this issue, we are developing a nanofluidic system to manipulate single particles and molecules that will enable multiple measurements on the same molecule (Figure 1). Nanofluidic channels will function as traps to localize the molecule in the system after its translocation (transit) through the nanopore. When the electric field across the nanopore is reversed, the same molecule will travel through the nanopore again. Feedback control will be used to reverse the applied voltage bias and thus ensure multiple translocations of a molecule through the nanopore. This technique will enable integration of a signal over multiple translocations, thereby improving the signal-to-noise ratio. For proof-of-concept, translocation signals of DNA molecules through a PDMS (polydimethylsiloxane) nanopore will be measured using a patch-clamp amplifier. Techniques of E-beam lithography and UV lithography are adopted to create a master mold of the device consisting of nanopores and reservoirs. Soft lithography with PDMS will be used for rapid and reproducible fabrication of nanopores connecting two reservoirs (Figure 2) [3]. This approach will demonstrate a new paradigm in sensing by using nanopores, and it may enable an unprecedented level of characterization of nanoparticles and biomolecules.

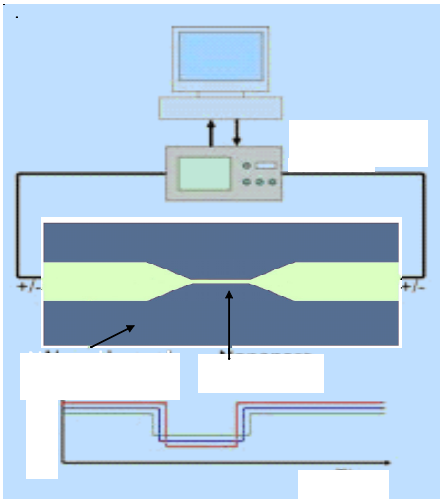

▲ Figure 1: Experiment setup and expected current signal profile for the passage of a molecule through the nanopore. The amplifier serves as a clamped voltage source and measures the corresponding current signal. Data will be obtained from multiple translocations of a single molecule through a nanopore enabled by feedback control. The nanochannel reservoir will prevent escape of the molecule of interest into the solution

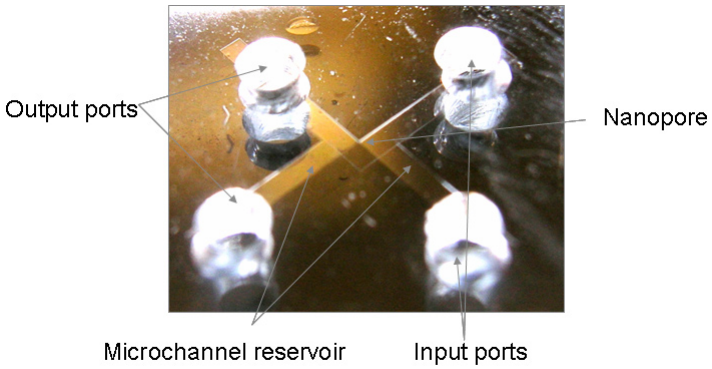

▲ Figure 2: Details of a nanopore molecule sensing device. The PDMS device is fabricated using E-beam lithography and UV lithography, followed by soft-lithography. Two reservoirs are connected with one nanopore.

References

[1] J.J. Kasianowicz, E. Brandin, D. Branton, and D.W. Deamer, "Characterization of individual polynucleotide molecules using a membrane channel,"in *Proc. National Academy of Sciences USA*, vol. 93, pp. 13770–13773, Nov. 1996.

[2] D. Fologea, J. Uplinger, B. Thomas, D.S. McNabb, and J.L. Li, "Slowing DNA transportation in a solid-state nanopore," *Nano Letters*, vol. 5, no. 9, pp. 1734-1737, 2005.

[3] A.O. Saleh and L.L. Sohn, "An artificial nanopore for molecular sensing," *Nano Letters*, vol. 3, no. 1, pp. 37-38, 2003.

Microfluidic Systems for Continuous Crystallization

M. Sultana, K.F. Jensen
Sponsorship: Merck, Lucent Technologies

Microfluidic systems offer a unique toolset for discovering new crystal polymorphs and for studying the growth kinetics of crystal systems because of well-defined laminar flow profiles and online optical access for measurements. Traditionally, crystallization has been achieved in batch processes that suffer from non-uniform process conditions across the reactors and chaotic, poorly controlled mixing of the reactants, resulting in polydisperse crystal size distributions (CSD) and impure polymorphs. This reduces reproducibility, increases difficulty in obtaining accurate kinetics data, and manufactures products with inhomogeneous properties. The short length scale in microfluidic devices allows for better control over the process parameters, such as the temperature and the contact mode of the reactants, creating uniform process conditions across the reactor channel. Thus, these devices have the potential to generate more accurate kinetics data and produce crystals with a single morphology and a more uniform size distribution. In addition, microfluidic systems decrease waste, provide safety advantages, and require only minute amounts of reactants, which is most important when dealing with expensive materials such as pharmaceutical drugs.

Figure 1 shows a microfluidic device used for crystallization and Figure 2 shows optical images of different polymorphs of glycine crystals grown in reactor channels. A key issue for achieving continuous crystallization in microsystems is to eliminate heterogeneous crystallization – irregular and uncontrolled formation and growth of crystals at the channel surface-- and aggregation of crystals, which ultimately clogs the reactor channel. We have developed a microcrystallizer using soft lithography techniques that introduces the reagents to the reactor channel in a controlled manner, preventing heterogeneous crystallization and aggregation. We have also integrated an online spectroscopy tool for *in situ* polymorph detection. Our ultimate goal is to develop an integrated microfluidic system for continuous crystallization with the ability to control and detect the crystal morphology, as well as obtain kinetics of crystallization through online detection.

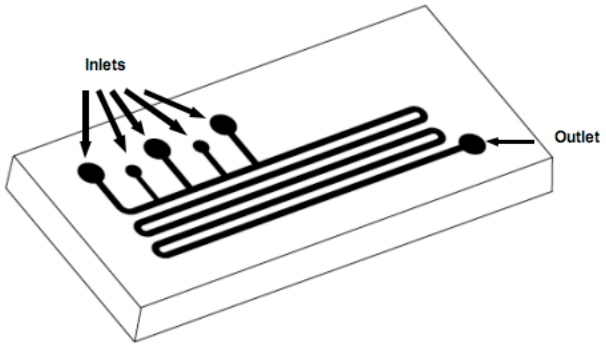

▲ Figure 1: Microfluidic device used for crystallization.

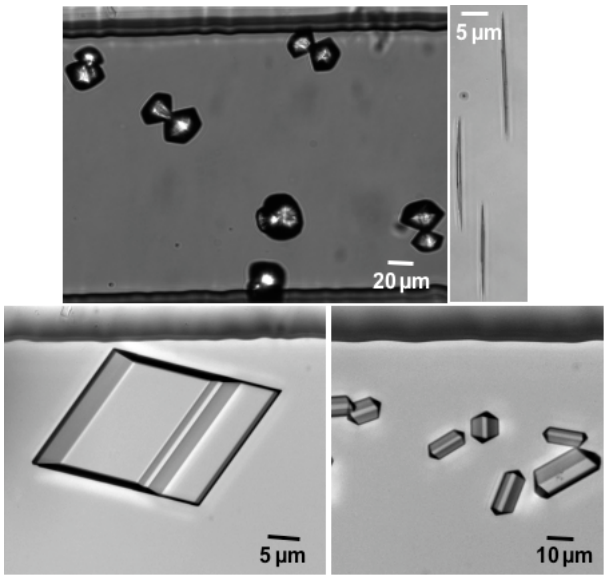

▲ Figure 2: Different sizes and shapes of glycine crystals produced in reactor channel.

Massively-parallel Ultra-high-aspect-ratio Nanochannels for High-throughput Biomolecule Separation

P. Mao, J. Han

Sponsorship: KIST IMC, NIH

Many bottom-up approaches have been used to build nano/mesoporous materials/filters with a good size control, but the integration of these systems into a microsystem format has been a challenge. Top-down nanofilter fabrications, on the other hand, suffered from small open volume and low throughput. For this paper, we developed a top-down fabrication strategy for massively-parallel, regular vertical nanochannel membranes with a uniform, well-controlled gap size of ~50 nm and a depth up to ~40 μm, by using only standard semiconductor fabrication techniques [1]. The vertical nanofilter membranes were fabricated into an anisotropic nanofilter array, which demonstrates the ability to integrate nanofilters and micron-sized channels/pores seamlessly. We demonstrated efficient continuous-flow separation of large DNAs in a two-dimensional vertical nanochannel array device as shown in Figure 2. Compared with planar nanofilter systems [2], an important feature of our device is a sample processing rate as high as ~ 1 μL hour^{-1}, and further improvement of throughput can be achieved simply by upscaling the channel depths. These ultrahigh-aspect-ratio nanochannels have the advantage of large open volume, enabling high-throughput applications.

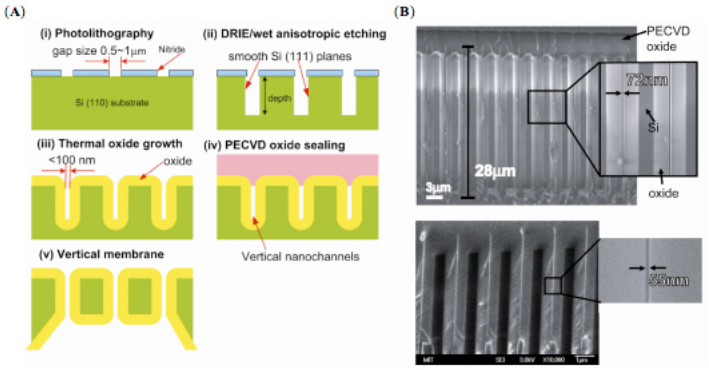

▶ Figure 1: (A) Schematic diagram of fabricating massively-parallel vertical nanofluidic channels. (B) Cross-sectional SEM micrograph of slit-like vertical nanochannels with a uniform gap size of 72 nm and 55 nm. The channels are etched by KOH etching and have a depth of 28 μm. The channels are completely sealed by depositing 3-μm-thick PECVD oxide.

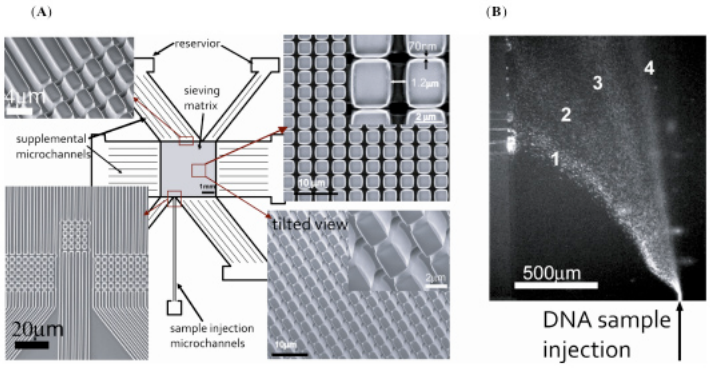

▶ Figure 2. Continuous fractionation of long DNAs through the two-dimensional anisotropic pillar array device. (A) The device includes a sieving matrix and surrounding microfluidic channels. The pillar array consists of horizontal nanochannels with a width of 70 nm and longitudinal channels with a width of 1.2 μm. Supplemental microchannels connecting sieving matrix and reservoirs are 1.5 μm in width. They are all 15 μm deep. (B) Fluorescence micrographs show separation of the mixture of λ-DNA Hind III digest. Electrical fields applied both in horizontal and longitudinal directions in sieving matrix are 80 V cm^{-1} and 30 V cm^{-1}, respectively. Band assignment: (1) 23.13 kbp; (2) 9.4 kbp; (3) 6.58 kbp; (4) 4.36 kbp.

References

[1] P. Mao and J. Han, "High-throughput continuous-flow separation of biomolecules in a high-aspect-ratio nanofilter array," in *Proc. Biomedical Engineering Society Annual Fall Meeting*, Chicago, IL, 2006.

[2] J. Fu, R.B. Schoch, A.L. Stevens, S.R. Tannenbaum, and J. Han, "A patterned anisotropic nanofluidic sieving structure for continuous-flow separation of DNA and proteins," *Nature Nanotechnology*, vol. 2, pp. 121-128, 2007.

Microfluidic Control of Cell Pairing and Fusion

A. Skelley, J. Voldman
Sponsorship: NIH

Currently, several different methods have been used to reprogram somatic cells to an embryonic stem cell-like state. Nuclear transfer and fusion methods [1] use either oocytes or embryonic stem cells (ESCs) as a source of reprogramming factors. Recently, defined factors have been identified that are capable of inducing pluripotency in somatic cells[2] [2]. While all three approaches can be used successfully for reprogramming, cell lines generated are not yet suitable for potential therapeutic applications in humans and many questions remain about the process of nuclear reprogramming.

We have developed a microfluidic system in which thousands of ESCs and somatic cells (SCs) are properly paired and immobilized, resulting in a high number of one-to-one fusions that can be clearly identified for further studies [3]. The device consists of thousands of cell traps in a millimeter-sized area, accessed by microfluidic channels (Figure 1). The traps consist of larger frontside and smaller backside capture cups made from a transparent biocompatible polymer. Cells are loaded sequentially in a 3-step loading protocol enabling capture and pairing of two different cell types. The geometry of the capture comb precisely positions the two cells, and flow through the capture area keeps the cells in tight contact in preparation for fusion. Pairing efficiencies of ~70% are possible over the entire device (Figure 2).

The device is compatible with both chemical and electrical fusion. The PEG-mediated fusion is initiated by flowing PEG past the cells for 3 minutes and then rinsing with warm media. With 4 doses of PEG, we have observed that 15 % of the traps contain cells that have exchanged fluorescent proteins, and 25 % of the traps contain cells whose membranes have reorganized. A control protocol done in a standard conical tube yielded only 6 ± 4 % fusion of the same fluorescent cells. Electrofusion is made possible by bonding the PDMS device to a glass slide with pre-patterned metal electrodes that are then connected to a standard fusion power supply. We have observed membrane fusion efficiencies up to 90% and can achieve > 50% properly paired and fused cells, based on exchange of fluorescence, over the entire device. Control fusion protocols, performed using the same power supply with a commercial electrofusion chamber, obtained only 11 +/- 9 % fusion. We have demonstrated pairing and fusion of mESCs and mEFs and are currently using the device to explore fusion-based reprogramming.

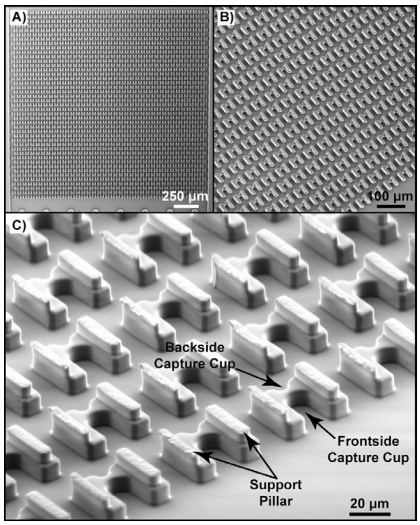

▲ Figure 1: A PDMS device for cell capture and pairing. (A) The device is 2 mm x 2 mm and contains ~ 1000 cell traps. (B,C) The traps are arrayed densely in the device, and each trap consists of frontside and backside capture cups along with support pillars.

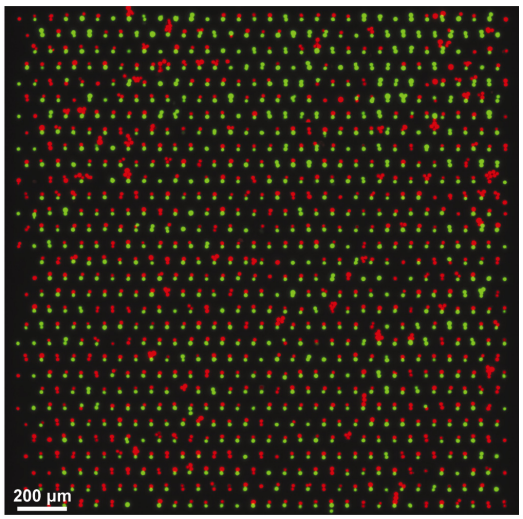

▲ Figure 2: Fluorescent overlay image of red and green fluorescent 3T3 mouse fibroblasts captured and paired in the device. Pairing efficiencies up to ~ 70% are possible.

References

[1] C.A. Cowan, J. Atienza, D.A. Melton, and K. Eggan, "Nuclear reprogramming of somatic cells after fusion with human embryonic stem cells," *Science*, vol. 309, pp.1369-1373, 2005.

[2] K. Takahashi, K. Tanabe, M. Ohnuki, M. Narita, T. Ichisaka, K. Tomoda, and S. Yamanaka, "Induction of pluripotent stem cells from adult human fibroblasts by defined factors," *Cell*, vol. 131, pp. 861-872, 2007.

[3] A.M. Skelley, O. Kirak, R. Jaenisch and J. Voldman, "Studying reprogramming of somatic cells via fusion with embryonic stem cells: A massively parallel device for cell fusion," *MicroTotal Analysis Systems*, vol. 1, pp. 581-582, 2007.

BioMEMS for Modulating Stem Cell Signaling

K Blagović, L.Y. Kim, N. Mittal, L. Przybyla, S. Sampattavanich, J. Voldman
Sponsorship: NIH, NSF Graduate Research Fellowship, SNSF Fellowship for Prospective Researchers

The stem cell microenvironment is influenced by several factors including cell-cell, cell-matrix, and cell-media interactions. Although conventional cell-culture techniques have been successful, they provide incomplete control of the cellular microenvironment. To enhance traditional techniques, we have developed several microscale systems for adherent cell culture of mouse embryonic stem cells (mESCs) while controlling the microenvironment in novel ways [1].

We are using stencil cell patterning and microscopic analytical tools to investigate cell-cell interactions, in particular the role of colony-colony interactions in self-renewal of mESCs. Since autocrine signaling in mESCs has not been thoroughly characterized, we validate our platform using a model autocrine cell line, A431 epidermoid carcinoma cells. By precisely controlling the colony size, spacing, and the medium replenishing frequency, we modulate the degree of colony-colony interactions (Figure 1). We are also using the Bio Flip Chip to investigate cell-cell signaling in mESCs. The chip is made from PDMS using replica molding, and it contains hundreds-to-thousands of microwells, each sized to hold either a single cell or small numbers of cells (Figure 1) [2]. A microscale cellular manipulation technique for cell-matrix interactions involves the patterning of specific protein signals around live mESC colonies in order to study the local effects of signal presentation. A photopolymerizable polymer (PEG-diacrylate) with attached proteins has been used to pattern structures around growing cell colonies in vitro, thereby exposing them to a very controlled microenvironment. Using these methods, we have patterned a known regulator of pluripotency, LIF, around mESC colonies and analyzed how far this signal propagated through the colony (Figure 1).

To control cell-media interactions we have developed a two-layer PDMS microfluidic device that contains two sets of triplicate chambers, allowing implementation of different culture conditions on the same chip. The device incorporates a valve architecture modeled after Irimia et al. [3], which enables different parts of the device to be fluidically isolated during different stages of the experiment. Using our system, we demonstrated that microfluidic perfusion can affect the soluble microenvironment. We showed that defined serum-free media (N2B27), sufficient for differentiating cells into neuronal precursors in static culture [4], did not allow cells to proliferate or differentiate on-chip. On the same chip we cultured cells in N2B27 that had been supplemented with media containing cell-secreted factors from a static culture. In this media, we were able to restore growth and differentiation (Figure 2).

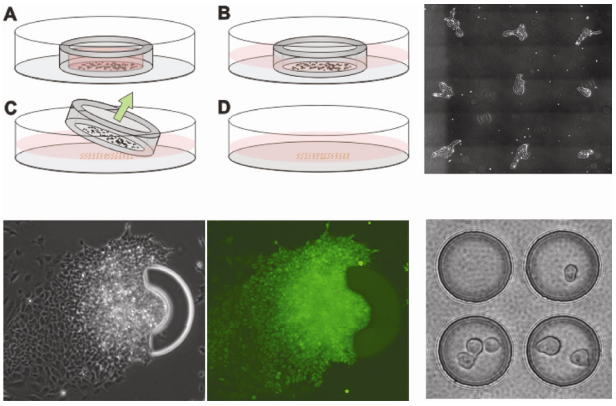

▲ Figure 1: Stencil patterning procedure: A) Load cells. B) Fill dish with media. C) Remove stencil. D) Rinse with medium to remove unattached cells (top, left). Patterned A431 colonies (top, right). PEGDA structures with attached LIF surrounding a mESC colony. Immunostaining is for Oct4, a stem cell pluripotency marker (bottom, left). Bio Flip Chip (bottom, right).

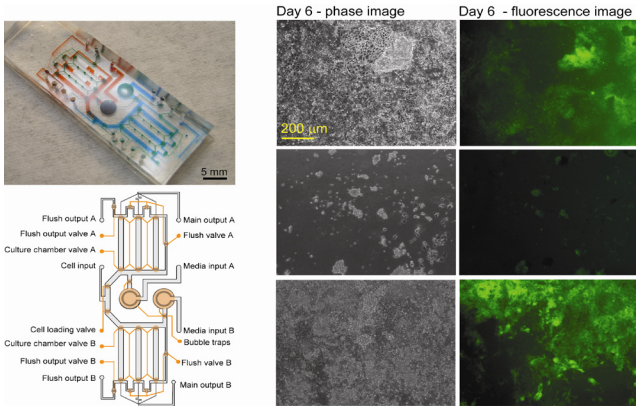

▲ Figure 2: Image of the perfusion device filled with dye to illustrate the different layers (top, left,). Schematic of the device (bottom, left). Images of cells in static N2B27 culture (top, right), in N2B27 on-chip culture (middle, right) and on-chip N2B27 culture supplemented with the media from a static culture (bottom, right). Green fluorescence indicates expression of an early neuronal differentiation marker Sox1.

References

[1] L. Kim, Y.C. Toh, J. Voldman, and H. Yu, "A practical guide to microfluidic perfusion culture of adherent mammalian cells," *Lab on a Chip*, vol. 7, pp. 681-694, June 2007.
[2] A. Rosenthal, A. Macdonald, and J. Voldman, "Cell patterning chip for controlling the stem cell microenvironment," *Biomaterials*, vol. 28, pp. 3208-3216, Mar. 2007.
[3] D. Irimia and M. Toner, "Cell handling using microstructured membranes," *Lab on a Chip*, vol. 6, pp. 345-352, Mar. 2006.
[4] Q.L. Ying, M. Stavridis, D. Griffiths, M. Li, and A. Smith, "Conversion of embryonic stem cells into neuroectodermal precursors in adherent monoculture," *Nature Biotechnology*, vol. 21, pp. 183-186, Feb. 2003.

Microfabricated Slits in Series: A Simple Platform to Probe Differences in Cell Deformability

H. Bow, P. Abgrall, J. Han
Sponsorship: Singapore-MIT Alliance

Change in cell stiffness is a characteristic of blood cell diseases, such as sickle cell anemia [1], malaria [2], and leukemia [3]. Often, increases in blood cell stiffness lead to loss of the cells' ability to squeeze through capillaries, resulting in organ failure, coma, and ultimately death [4]. The goal of this project is to create a microfluidic device that can quickly and accurately screen, diagnose, and treat disorders involving cell deformability. We report the creation of a microfabricated device consisting of a series of 1-2 μm wide polymeric slits, as Figures 1 and 2 show. This device can potentially be used to screen and diagnose disorders involving cell deformability.

The device fabrication process is depicted in Figure 1 and follows approaches similar to those in [5]. First, a 2-level negative PDMS stamp was made using soft lithography techniques from a silicon template, Figure 1a. A droplet of UV-sensitive prepolymer NOA 81 was stamped on a glass slide and exposed to UV, Figure 1b. Similarly, a droplet of NOA was stamped using a flat PDMS slab and exposed to UV on a PDMS cover sheet treated with oxygen plasma to improve the adhesion. After the stamps were peeled off , the two pieces were brought in contact and bonded by completing the crosslinking with a second exposure to UV, as in Figure 1C. Figure 1 details the device's operation and results of fabrication.

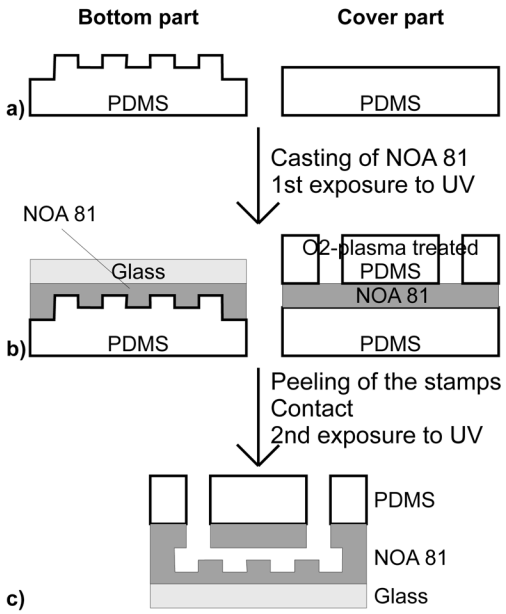

▲ Figure 1: Fabrication details.

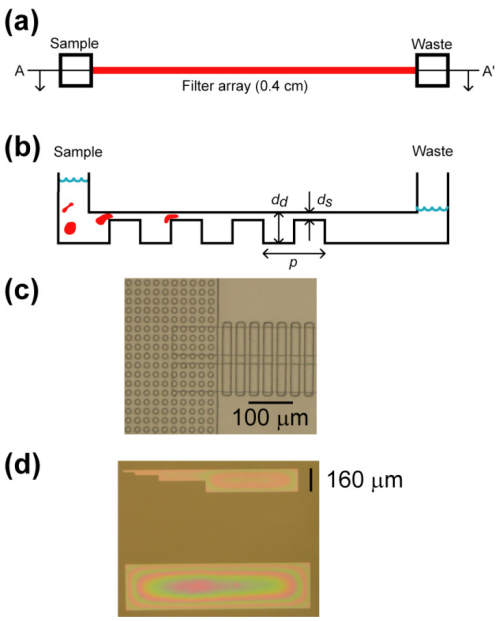

▲ Figure 2: (a) Device schematic. (b) Cross-section through A-A'. (c) Picture from top of actual device near entrance. (d) Test structures indicating 2-μm-deep features with aspect ratio of up to 2/320 did not collapse.

References

[1] E. Evans, N. Mohandas, and A. Leung, "Static and dynamic rigidities of normal and sickle erythrocytes," *Journal of Clinical Investigation*, vol. 73, pp. 477-488, 1984.
[2] J.P. Shelby, J. White, K. Ganesan, P.K. Rathod, and D. Chiu, "A microfluidic model for single-cell capillaryobstruction by plasmodium falciparum-infected erythrocytes," *Proc. National Academy of Sciences*, vol. 100, no. 25, pp. 14618-14622, 2003.
[3] M.J. Rosenbluth, W.A. Lam, and D.A. Fletcher, "Force microscopy of nonadherent cells: A comparison of leukemia cell deformability," *Biophysical Journal*. vol. 90, pp. 2994-3003, 2006.
[4] V. Kumar, A.K. Abbas, and N. Fausto, *Robbins and Cotran Pathologic Basis of Disease*, Philadelphia: Saunders, 2004.
[5] S.H. Kim, Y. Yang, M. Kim, S.W. Nam, K.M. Lee, N.Y. Lee, Y.S. Kim, and S. Park, "Simple route to hydrophilimicrofluidic chip fabrication using an ultraviolet (Uv)-cured polymer," *Advanced Functional Materials*. vol. 17, no. 17, pp. 3493-3498, Nov. 2007.

Microfluidic System for Screening Stem Cell Microenvironments

W.G. Lee, B.G. Chung, A. Khademhosseini
Sponsorship: NIH, CIMIT

Embryonic stem cell (ESC) differentiation is a potentially powerful approach for generating a renewable source of cells for regenerative medicine. It is known that the microenvironment greatly influences ESC differentiation and self-renewal. Most biological studies have aimed at identifying individual molecules and signals. However, it is becoming increasingly accepted that the many kinds of signals in the ESC microenvironment interact in a synergistic and antagonistic manner based on their temporal and spatial expression, dosage, and specific combinations. This interplay of microenvironmental factors regulates the ESC fate decisions to proliferate, self-renew, differentiate, and migrate. Despite this complexity, the systematic study of stem cell cues is technologically challenging, expensive, slow, and labor-intensive. Here we propose to develop a high-throughput microfluidic based system that overcomes many of these challenges. We will subsequently analyze the resulting high-throughput system in elucidating specific aspects of mesodermal and endodermal differentiation in a systematic manner.

A simple microfluidic screening device consisted of fluidic channels, control channels, and poly(ethylene glycol) (PEG) microwells has been developed (Figure 1). A microfluidic screening device was fabricated by multi-layer soft lithography technique [1]. The fluidic channel made by positive photoresist (AZ 4620) is 10-μm-thick pattern with a round shape and the pneumatically actuated control channel fabricated by negative photoresist (SU-8 2150) is a 40-μm-thick pattern. To obtain a round profile of a fluidic channel, the positive photoresist (AZ 4620) was reflowed at 200°C for 120 sec after development. A replica of the fluidic channel was obtained by spin-coating poly(dimethylsiloxane) (PDMS) at 1700 rpm for 1 min followed by baking at 70 °C for 1.5 hours. This process resulted in a 20-μm-thick PDMS membrane containing the fluidic channel. The crossing of the control channel over the fluidic channel formed the on-chip barrier valve. We used ES-green fluorescent protein (GFP) cells that can express Octamer-4 (Oct4), a homodomain transcription factor. The ES-GFP cells were seeded into a fluidic channel and localized within PEG microwells in a flow-based microfluidic screening device (Figure 2). The ES cells were well docked and patterned within a microwell, while cells that were not localized within a microwell were flowed into a reservoir. The ES cells expressed by Oct4 (green) maintained self-renewal during media perfusion (0.3 μl/min). The ES cells docked within a microwell showed high cell viability (> 90%).

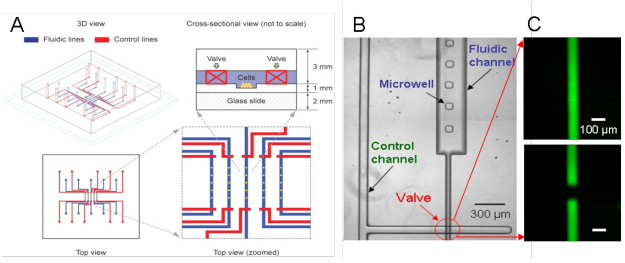

▲ Figure 1: A simple microfluidic screening device. (A) Schematic design of a microfluidic device. (B) Phase contrast image of a microfluidic screening device integrated with fluidic channel, control channel, and PEG hydrogel microwell (100×100 μm). (C) Actuation of on-chip valve. FITC-dextran images in a fluidic channel as valve is opened and closed.

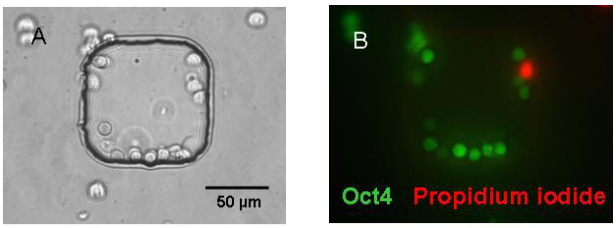

▲ Figure 2: Cell viability of mouse ES cells exposed to media for 2 hours in a microfluidic screening device. ES cells were expressed by Oct-4 (green) and dead cells (red) were indicated by propidium iodide.

Reference

[1] B.G. Chung, F. Lin, and N.L. Jeon, "A microfluidic multi-injector for gradient generation," *Lab on a Chip*, vol. 6, no. 6, pp. 764-768, June 2006.

Self-assembly of Cell-laden Microgels with Defined 3D Architectures on Micro-patterned Substrate

Y. Du, A. Khademhosseini
Sponsorship: NIH, CIMIT

Most living tissues are composed of repeating units on the scale of hundreds of microns; these units are ensembles of different cell types with well-defined three-dimensional (3D) microarchitectures and tissue-specific functional properties (i.e., islet, nephron, or sinusoid) [1]. To generate engineered tissues, the recreation of these repeating structural features is of great importance in enabling the resulting tissue function. Here, we tried to self-assemble cell-laden microscale hydrogel (microgel) units as 3D tissue constructs with defined architecture by using hydrophobic/hydrophilic interactions. By micro-contact printing [2], we patterned the glass slides with specific hydrophobic and hydrophilic regions [3]. We hypothesized that the hydrophilic microgels tend to stick to the hydrophilic patterns, while not on the hydrophobic patterns. Therefore, we could control the architecture of the microgel assembly by creating different hydrophilic patterns.

To achieve microcontact printing, we first created different SU 8 patterns on the silicon wafer based on the photomask by using standard photolithography. The SU 8 patterns were transferred to the PDMS mold, which was soaked with the hydrophobic ink. The ink was printed with specific patterns on the glass slide by microcontact printing. Afterwards, the slides were covered in DPBS (~600 μL of DPBS) containing microgels (approximately 1500 gel units each patterned slide). After a few minutes, the slides were tilted over, to allow the liquid to drain off the slide. Microgels remained on only the hydrophilic glass surfaces, as predicted. Below are images of microgel assembly on a 1600-um square pattern on the glass slide.

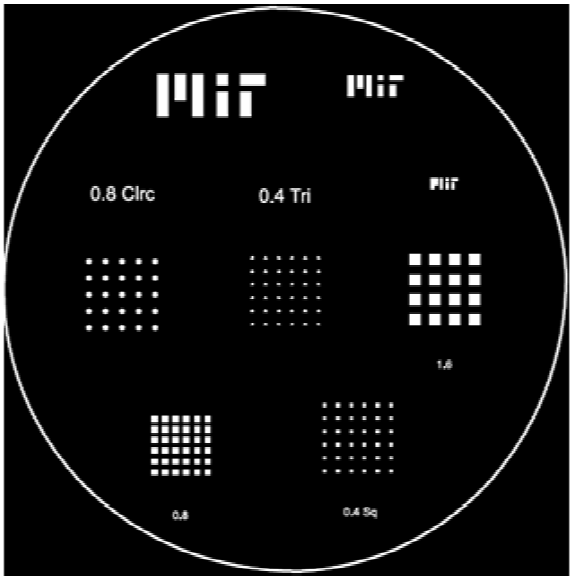

▲ Figure 1: Photomask containing various patterning designs.

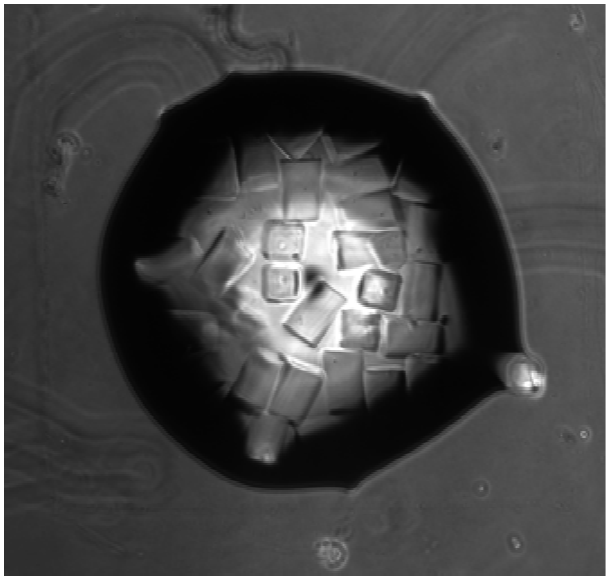

▲ Figure 2: Phase-contrast image of self-assembled microgel building blocks on a hydrophilic pattern.

References

[1] L. Costanzo, *Physiology (3rd edition)*. Philadelphia: Saunders, 2006.
[2] L. Lauer, C. Klein, and A. Offenhausser, "Spot compliant neuronal networks by structure optimized micro-contact printing," *Biomaterials*, vol. 22, pp. 1925-1932, July 2001.
[3] E. Kokkoli and C.F. Zukoski, "Interaction forces between hydrophobic and hydrophilic self-assembled monolayers," *Journal of Colloid Interface Science*, vol. 230, pp. 176-180, Oct. 2000.

High-throughput Study of Cell-ECM Interactions in 3D Environment Using Microwell Arrays

L. Kang, J. Shim, S. Lee, A. Khademhosseini

Sponsorship: NIH, CIMIT

The extracellular matrix (ECM) is critical in developing an integrated picture of the role of the microenvironment in the fate of many cells. A two-dimensional (2D) microarray method was reported for cell-ECM interaction study [1]. These 2D approaches can be complemented by three-dimensional (3D) approaches such as embedding cells within ECM gels [2]. However, 3D microarray methods are difficult to develop due to difficulties such as ECM array fabrication and nanolitre liquid handling. To overcome these difficulties, microwell array and robotic spotting may be useful.

In this study, we develop an approach using a microarrayer (Piezorray) and microwell arrays for cell-ECM interaction study with high throughput. The microwell array was fabricated with soft lithography (Figure 1). The diameter of a microwell was 400 μm with a pitch of 600 μm. In total, 2100 microwells were fabricated on a single slide with numbers and alphabets in between for identification (Figure 2A). As a proof-of-concept experiment, it was shown that dye solutions can be printed accurately into these microwells preloaded with collagen solution (Figure 2B). For future study, we will print the ECM component in a combinatorial manner into the microwell array preloaded with cells in prepolymer solutions. Then, the mixtures will be UV-crosslinked to immobilize the ECM mixture inside each isolated microwell for cell-ECM interaction study.

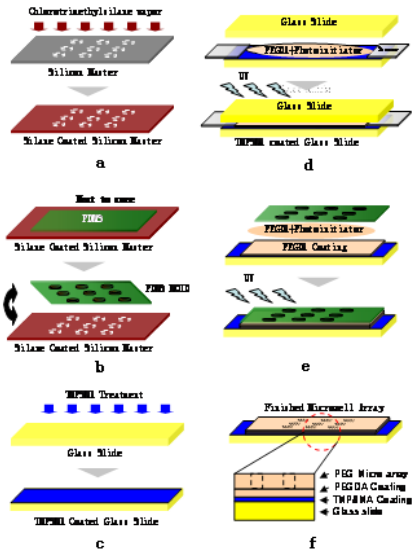

▲ Figure 1: The schematic representation of fabricating a microwell array containing 2100 microwells on a single glass slide.

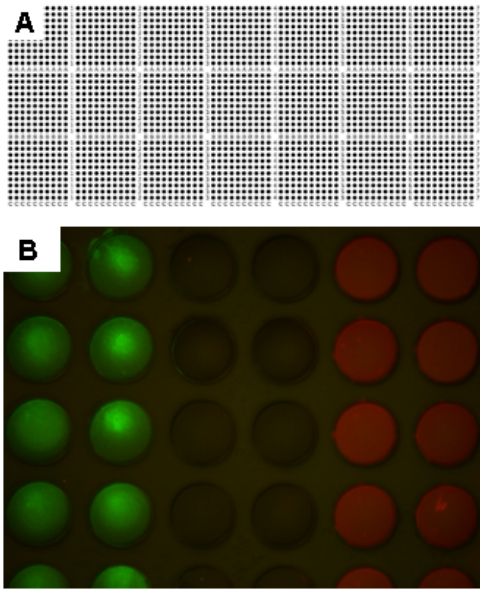

▲ Figure 2: A) The layout of the microwell array. B) FITC-BSA (green) and Rhodamine-dextran (red) dyes were printed into the microwells using a microarrayer (well diameter = 400μm).

References

[1] C.J. Flaim, S. Chien, and S.N. Bhatia, "An extracellular matrix microarray for probing cellular differentiation," *Nature Methods*, vol. 2, pp. 119–125, Jan. 2005.

[2] M.Y., Lee, R.A. Kumar, S.M. Sukumaran, M.G. Hogg, D.S. Clark, and J.S. Dordick, "Three-dimensional cellular microarray for high-throughput toxicology assays," *Proceedings of the National Academy of Sciences*, vol. 105, pp. 59-63, Jan. 2008.

Amplified Electrokinetic Response by Concentration Polarization near Nanofluidic Channel

S.J. Kim, J. Han

Sponsorship: NIH

Due to a strong electrokinetic response inside an ion-depletion region created by concentration polarization, the velocity of non-equilibrium electroosmotic flows (EOF) inside the ion-depletion zone can be 10 times faster than any equilibrium EOFs. [1, 2] Fast fluid vortices were generated at the anodic side of the nanochannel due to the non-equilibrium EOF. The vortex flow speed was estimated to be usually about 1000 μm/sec, which is about ~10X higher than that of primary EOF under the same electrical potential, and was proportional to the square of applied voltage, as shown in Figure 1(a). At the steady state, we can clearly observe the two counter-rotating vortices beside the nanochannel, as Figure 1(b) shows. In the dual-sided nanochannel device, since the ions were depleted through both walls, the four independent vortices were formed in the four divided regions, as shown in Figure 1(c). One can independently suppress the convective part of the phenomena by decreasing the microchannel thickness. As Figure 1(d) shows, the size of the vortex in the dotted circle was approximately 2μm, which corresponded to the depth of the microchannels. We also observed that, once the particles pass the depletion zone and entered the downstream low concentration zone, they travel 25 times faster than in the buffer zones, as Figure 2 shows. These results indicate that the concentration polarization (depletion) can be utilized to make efficient and novel electrokinetic pumps and fluid switching devices, at an efficiency that has never been demonstrated.

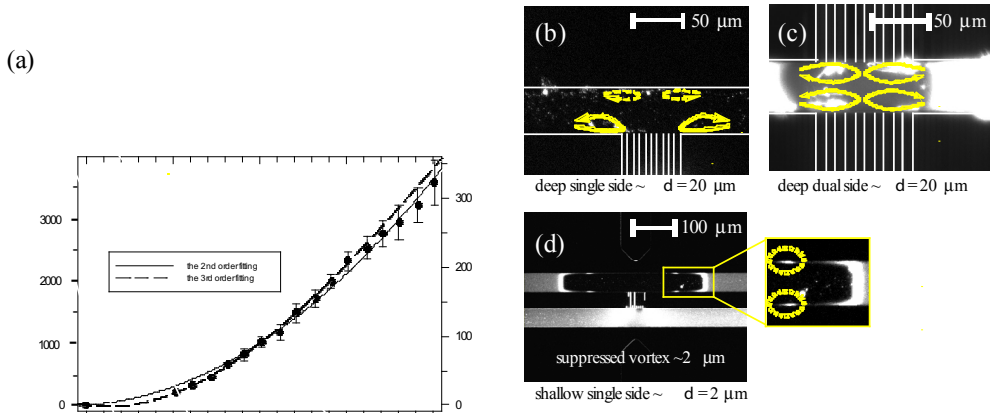

▲ Figure 1: (a) The translational and angular speed of the vortex as a function of applied voltage. The speed was 10 times or even higher than equilibrium EOFs. The data was fitted by the second order polynomial to reveal the proportionality to $|E|^2$. (b) A fast vortex at steady state in single-sided nanochannel device. (c) Four independent strong vortices in dual-sides nanochannel device. (d) Suppressed vortices in a shallow single-sided nanochannel device.

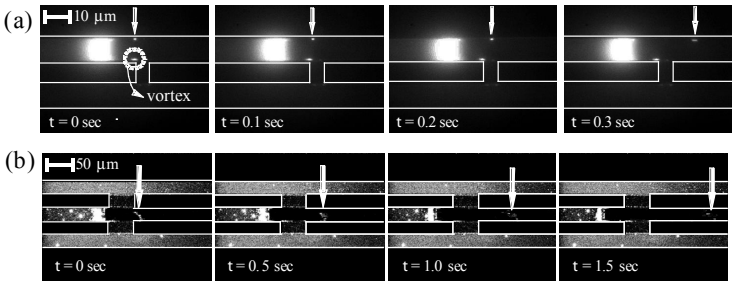

▲ Figure 2: The electrokinetic migration of charged particles in (a) single-sided and (b) dual-sided nanochannel devices. Estimated velocity of pointed particles was approximately (a) 140 μm/sec and (b) 500 μm/sec at E_T =5V/cm.

References

[1] S.J. Kim, Y.C. Wang, J.H. Lee, H. Jang, and J. Han, "Concentration polarization and nonlinear electrokinetic flow near a nanofluidic channel," *Physical Review Letters*, vol. 99, no. 4, pp. 044501:1-4, July 2007.

[2] A. Holtzel, and U. Tallarek, "Ionic conductance of nanopores in microscale analysis systems: Where microfluidics meets nanofluidics," *Journal of Separation Science*, vol. 30, no. 10, pp. 1398-1419, July 2007.

Micropipette Interfaces for Lab-on-a-Chip Systems

H. Lee, R.J. Ram, P. Boccazzi, A. Sinskey
Sponsorship: Lincoln Laboratory

We have developed a simple to use, pipette-compatible, integrated fluid injection port to interface closed microfluidic chambers for applications such as cell culture or microchamber PCR that are sensitive to external contamination. In contrast to open systems where fluid can be easily loaded into wells or flow-through microfluidic systems where interfacing involves bridging millimeter scale tubing with micrometer scale channels [1], filling closed chambers requires either first applying vacuum or venting the chamber. We have fabricated a pipette interface that automatically vents and seals upon insertion and removal of a pipette tip that can be directly integrated into fluidic devices.

The injection port is composed of a deformable elastomer nipple, compression housing, and flow and vent channels that interface with the fluid chamber. A schematic of the components is shown in Figure 1a and photographs are shown in Figures 1b through 1e. When the elastomer nipple (Figure 1c) is inserted in the compression housing (Figure 1d), the slit of the elastomer nipple is sealed closed, isolating the fluidic chamber from the external environment. Insertion of the pipette tip into the slit (Figure 1e) causes the nipple to deform, which opens the venting channel to the air while the pipette tip seals against the fluid flow channel. Actuation of the pipette plunger forces fluid into the chamber while air is vented around the pipette tip. Removing the tip reseals the port to prevent external contamination. The seal can withstand at least 15psi of backpressure.

The integrity of the injection port seal against bacterial contamination was tested using the device shown in Figure 2, which comprised eight closed chambers of 150µL in volume interfaced with an integrated injection port. By visual inspection and plating, the sealed ports prevented contamination while the negative controls were clearly contaminated.

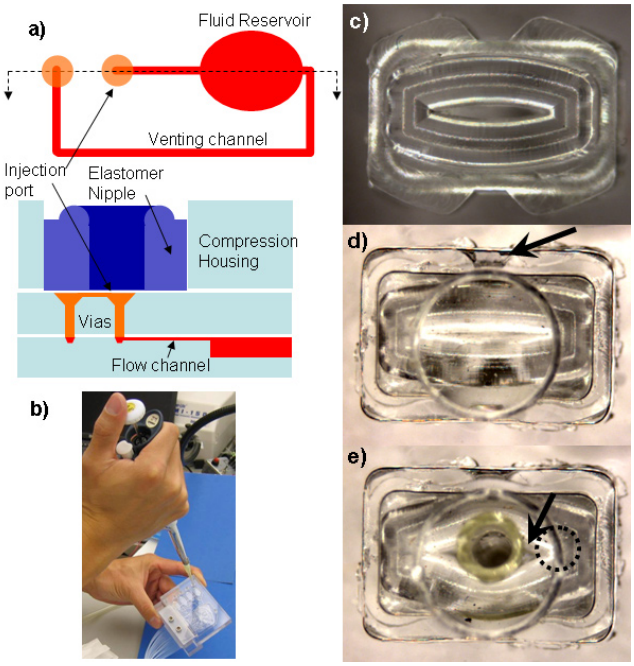

▲ Figure 1: a) Top and cross-section schematic representation of injection port. b) Photograph demonstrating fluid injection into a closed fluid reservoir using standard pipette. c) Elastomer nipple. d) Elastomer nipple inserted into compression housing. Arrow highlights open region to allow deformation upon pipette tip insertion. e) Port with 200uL pipette tip inserted. Arrow highlights opening in slit around the pipette where air is vented. Dotted circle outlines underlying vent port.

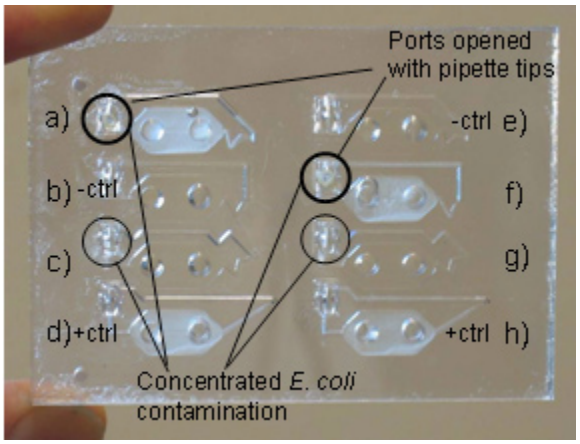

▲ Figure 2: Photograph of contamination test device. Eight 150-uL reservoirs are each interfaced with an integrated fluid injection port. A 70-um-thick PDMS membrane covers the reservoir to allow oxygenation. Reservoirs were prepared and then incubated for 24 hours at 37°C.

Reference

[1] C.K. Fredrickson and Z.H, Fan, "Macro-to-micro interfaces for microfluidic devices," *Lab on a Chip*, vol. 4, pp. 526-533, Apr. 2004.

Multiplexed Proteomic Sample Preconcentration Chip Using Surface-patterned Ion-selective Membrane

J.H. Lee, Y.-A. Song, J. Han

Sponsorship: NIH grants R01-EB005743 and P30-ES002109-28 (MIT CEHS)

We report a new method of fabricating a high-throughput protein preconcentrator in poly(dimethylsiloxane) (PDMS) microfluidic chip format. We print a submicron-thick ion-selective membrane on the glass substrate by using standard patterning techniques. By simply plasma-bonding a PDMS microfluidic device on top of the printed glass substrate, we can integrate the ion-selective membrane into the device and rapidly prototype a PDMS preconcentrator without complicated microfabrication and cumbersome integration processes. The PDMS preconcentrator showed a high preconcentration efficiency with a factor as high as ~10^4 in just 5 min., which was 12x higher than our previous PDMS preconcentrator fabricated by junction gap breakdown [1]. Moreover, we have demonstrated a fabrication of 10 single preconcentrators in an array format which increased the preconcentrated volume by 3 orders of magnitude compared to our previous result obtained with the silicon nanofluidic preconcentrator [2]. The ability to build a massively parallel array using this technique is significant in terms of the integration of our preconcentrator to an external sensing unit such as mass spectrometer. In addition to a shorter preconcentration time, the array can offer a sufficient amount of the concentrated sample volume to transfer it to an external sensing unit. Due to this capability, we expect a high potential of our PDMS preconcentrator chip as a signal enhancement tool for a mass spectrometer to detect low-abundance proteins and peptides. Furthermore, the PDMS microfluidic format of this device would allow the integration of preconcentrator into many different BioMEMS platforms, including cellular BioMEMS devices.

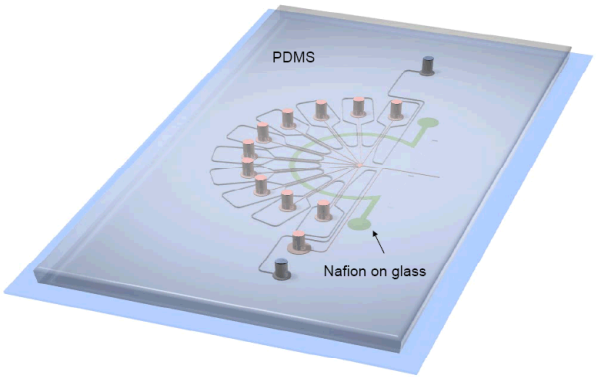

▲ Figure 1: Schematic of 10 array preconcentrators using integration of ion-selective membrane into PDMS preconcentrator by plasma bonding.

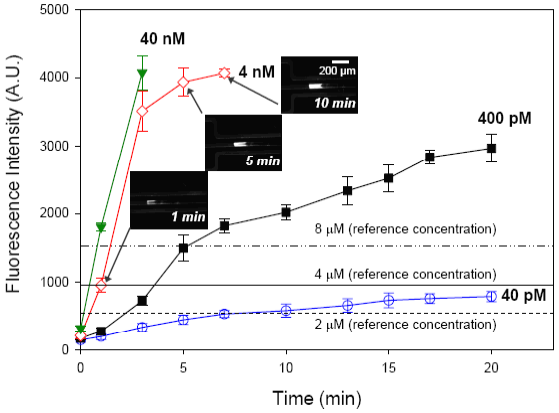

▲ Figure 2: Preconcentration of β-Phycoerythrin protein versus electrokinetic trapping time. This result shows that we can achieve a preconcentration factor of ~10^4 in 5 min. Fluorescence images of 4 nM protein shown next to the graph indicate an increase of the concentrated plug in size and concentration with trapping time.

References

[1] J.H. Lee, S. Chung, S.J. Kim, and J. Han, "Poly(dimethylsiloxane)-based protein preconcentration using a nanogap generated by junction gap breakdown," *Analytical Chemistry*, vol. 79, no. 17, pp. 6868-6873, Sept. 2007.

[2] Y.C. Wang, A.L. Stevens, and J. Han, "Million-fold preconcentration of proteins and peptides by nanofluidic filter," *Analytical Chemistry*, vol. 77, no. 14, pp. 4293-4299, July 2005.

Improving the Sensitivity and Binding Kinetics of Surface-based Immunoassays

V. Liu, Y.-C. Wang, J. Han
Sponsorship: NIH

Immunoassays are currently among the most widely used diagnostics tools in the healthcare industry. The usage of current immunoassays is limited by the availability of good antigen-antibody pairs, time-consuming incubation, and sensitivity limits. In particular, the sensitivity and binding kinetics are limited by the usually low concentration of molecules that we are trying to detect. One of the most common methods to overcome the limitations of sensitivity is by adding a post-binding amplification step, meaning that signals get enhanced after molecules are bound to capture antibodies. This method helps improve the sensitivity of the assay, but it fails to reduce the time required for the sensor to reach an equilibrium value because the low concentration of molecules still takes the same time to saturate the sensor. An alternative to post-binding amplification is pre-binding amplification. By increasing concentration of molecules of interest prior to their capture by antibodies, pre-binding amplification improves both the sensitivity of the sensor and kinetics of binding.

Our lab has developed and integrated a nanofluidics-based concentrator and has successfully integrated the device with an immunoassay [1]. The principle behind the concentrator, electrokinetic trapping, is a space-charge induced phenomenon that can be fine-tuned using external voltage controls. After application of appropriate voltages, a charge-depletion zone forms near the nanochannels and excludes all charged species. If the analyte-containing fluid is continuously moved into this zone, the analytes would accumulate and their concentration increase (Figure 1). The concentrator can be combined with an on-chip assay for improved assay sensitivity. In our lab, a 1,000-fold increase in sensitivity of assays has been demonstrated with fluorescent proteins in simple buffers (Figure 2). Currently, efforts are underway to adapt the system for use with non-natively fluorescent proteins in a more complex background such as serum. Development of a surface-coating method and a preconcentration scheme for non-natively fluorescent proteins is currently the main focus of this project.

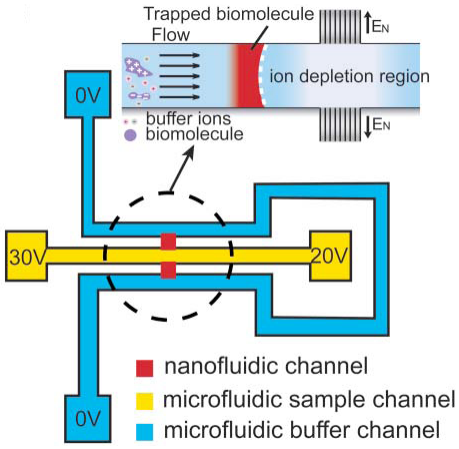

▲ Figure 1: A schematic diagram of the concentrator and operating principles.

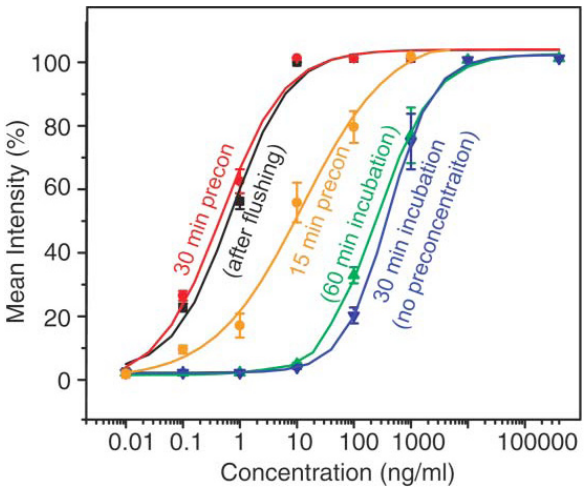

▲ Figure 2: Graph showing increase in sensitivity with pre-binding amplification.

Reference

[1] Y.-C. Wang and J. Han, "Pre-binding dynamic range and sensitivity enhancement for immuno-sensors using nanofluidic preconcentrator," *Lab on a Chip*, vol. 8, no. 3, pp. 392-394, Mar. 2008.

Mass-based Readout for Agglutination Assays

R. Chunara, M. Godin, S.M. Knudsen, S.R. Manalis
Sponsorship: ARO, NIH

Agglutination assays based on nanometer- and micrometer-sized particles were originally inspired by natural agglutination of cells [1] and provide a simple, rapid means for diagnostic testing. There are several commercial examples of agglutination assays used for clinical diagnostics applications. These assays are typically straightforward to administer and provide fast response times. Techniques for measuring agglutination include turbidity, dynamic light scattering, and UV – Vis spectroscopy. In some cases, particle-counting techniques such as flow cytometry and image analysis can improve sensitivity by quantifying small aggregates that are produced during the initial stages of aggregation, allowing a reduction of the required incubation times. Additionally, particle-counting enables gathering of more specific information about the agglutination distribution in a population, rather than reliance on the average agglutination information typically obtained by ensemble measurement techniques. Furthermore, microfluidic approaches for particle-counting can reduce the required sample volume from milliliters to microliters and enable integration with sample treatment steps.

We have developed a non-optical alternative for particle counting in which early-stage aggregation is quantified by measuring mass with the suspended microchannel resonator (SMR) [1]. In SMR detection, each aggregate is weighed in real-time by measuring transient changes in resonant frequency as it flows through the vibrating microchannel (Figure 1). Using a model system of streptavidin-functionalized microspheres and biotinylated antibody as the analyte, we obtain a dose-response curve showing particle agglutination over a concentration range of 630 pM to 630 nM (Figure 2). We show that the results are comparable to what has been previously achieved by image analysis and conventional flow cytometry.

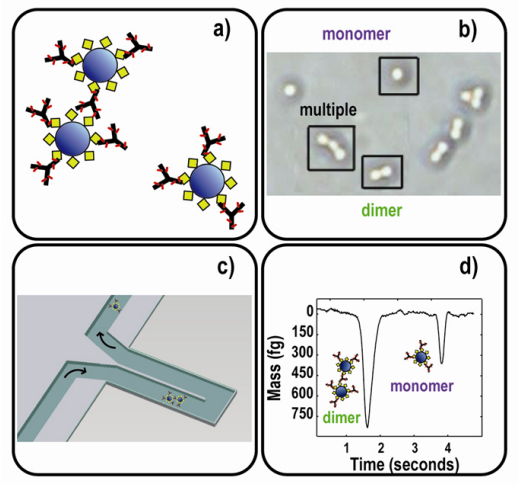

▲ Figure 1: a) Streptavidin (SA)-coated microspheres are incubated with the capture protein (SA is illustrated by diamonds). The analyte (biotinylated antibody) creates agglutination by binding to two different SA receptors located on separate microspheres. b) Optical micrograph of monomer, dimer, and multimer structures that are formed by agglutination of 0.97 μm SA microspheres with 0.63 nM of analyte. c) Schematic of the suspended microchannel resonator (SMR) for counting aggregates by weighing them one at a time. The resonance frequency of the SMR is sensitive to the presence of particles whose mass density differs from that of the solution in the microfluidic channel. d) The SMR is used to classify a monomer (right) and a dimer (left); it classifies anything larger as a multimer (not shown). The transient frequency shift from each structure is converted to a mass by using a calibration factor and accounting for the buffer density.

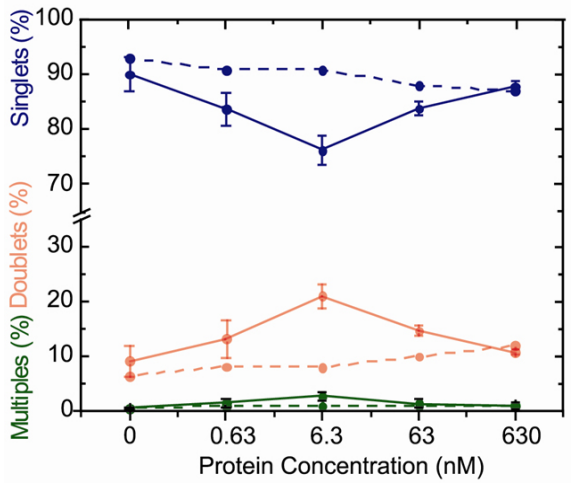

▲ Figure 2: Mass-based dose response curve obtained by weighing aggregates with the SMR. Each data point represents the mean obtained from three experiments, and at 0.63 nM, five experiments. The dependence of structure proportion is shown versus analyte concentration (biotinylated antibody in solid lines and pure antibody in dashed lines). Each data point represents the mean percentage of structures obtained from three separate experiments at each concentration. In each experiment approximately 2000 aggregates were weighed, and error bars represent the standard deviation from the mean.

Reference

[1] R. Chunara, M. Godin, S.M. Knudsen, and S.R. Manalis, "Mass-based readout for agglutination assays," *Applied Physics Letters*, vol. 91, no.19, pp. 193902:1-3, Nov. 2007.

Measuring the Mass, Density, and Size of Particles and Cells Using a Suspended Microchannel Resonator

M. Godin, A.K. Bryan, T. Burg, S.R. Manalis
Sponsorship: ARO

Nano- and micro-scale particles and colloidal solutions are central to numerous applications in industrial manufacturing, nanotechnology, and the life sciences. We demonstrate the measurement of mass, density, and size of cells and nanoparticles using suspended microchannel resonators (SMRs) [1]. The masses of individual particles are quantified as transient frequency shifts while the particles transit a microfluidic channel embedded in the resonating cantilever. Mass histograms resulting from these data reveal the distribution of a population of heterogenously sized particles. Particle density is inferred from measurements made in different carrier fluids, since the frequency shift for a particle is proportional to the mass difference relative to the displaced solution (Figure 1). We have characterized the density of polystyrene particles, Escherichia coli and human red blood cells with a resolution down to 10-4 g/cm3.

The SMR's particle measurement capabilities are a valuable complement to light scattering and other particle sizing methods currently used in numerous industrial and research applications. Of particular note is the SMR's ability to directly measure the mass/density of individual particles with high precision and accuracy. These capabilities provide a counterpoint to optical "ensemble" techniques such as laser diffraction, which are sensitive to the shape and optical properties of the target particles, and which for some samples are prone to artifacts and irreproducibility. In its current incarnation, the SMR excels for particles from ~ 50 nm to ~ 10 μm. Future improvements in mass resolution may allow measurement of particles down to the ~10-nm scale. The SMR's ability to measure particle density is unique among particle size analyzers and may be applied to applications such as the measurement of porosity and capacity of drug-loaded microspheres; the characterization of engineered porous silica used in coatings, slurries, and optoelectronics; and examination of the structure of submicron-sized particles.

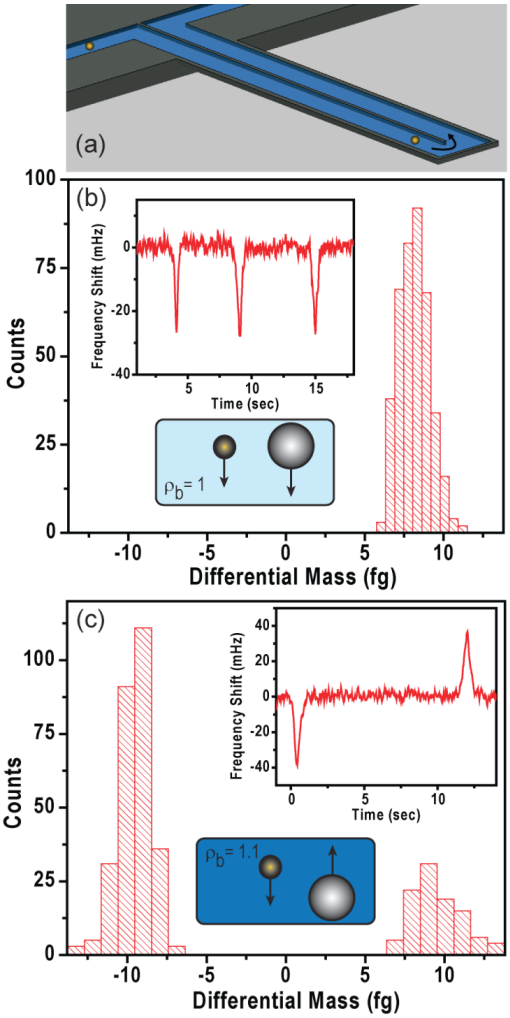

◀ Figure 1: (a) Particles flow through the suspended microfluidic channel contained within the resonating cantilever (the channel is completely enclosed within the beam). (b) A mixture of 99.5 nm gold and 708.6 nm polystyrene nanoparticles is measured in PBS. The differential mass of both particles is positive and the mass histograms overlap. The inset shows the time course of the frequency signal as particles flow through the device, but no peak can be assigned to either gold or polystyrene. The schematic indicates that both particles have a positive differential mass since their densities are larger than that of the surrounding fluid. (c) The differential mass of gold in a 44% glycerol/H2O solution remains positive, but it is negative for polystyrene, as immediately discerned from the time course data shown in the inset. The two histograms are now clearly distinct.

Reference

[1] M. Godin, A.K. Bryan, T. Burg, and S.R. Manalis, "Measuring the mass, density and size of particles and cells using a suspended microchannel resonator," *Applied Physics Letters*, vol. 91, no. 12, pp. 123121:1-3, Sept. 2007.

Making it Stick: Convection, Reaction and Diffusion in Surface-based Biosensors

T.M. Squires, R.J. Messinger, S.R. Manalis
Sponsorship: NIH

The past decade has seen researchers from a diverse range of disciplines develop and apply novel technologies for biomolecular detection, at times approaching hard limits imposed by physics and chemistry. In nearly all types of biomolecular sensors, the diffusive and convective transport of target molecules to the sensor can play as critical a role as the chemical reaction itself in governing binding kinetics and, ultimately, performance. This is particularly true as ever-smaller sensors are developed to interrogate ever-more-dilute solutions. Yet rarely does an analysis of the interplay between diffusion, convection and reaction motivate experimental design or data interpretation.

We have developed a physically intuitive and practical understanding of analyte transport for researchers who develop and employ biosensors based on surface capture [1]. Using a model sensor embedded within a microfluidic channel (Figure 1), we explore the qualitatively distinct behaviors that can result (Figure 2), develop rules of thumb to quickly determine how a given system will behave, and derive scaling relations that give order-of-magnitude estimates for fundamental quantities of interest, such as fluxes, collection rates, and equilibration times. We pay particular attention to collection limits for micro- and nano-sensors and highlight unexplained discrepancies between reported values and theoretical limits.

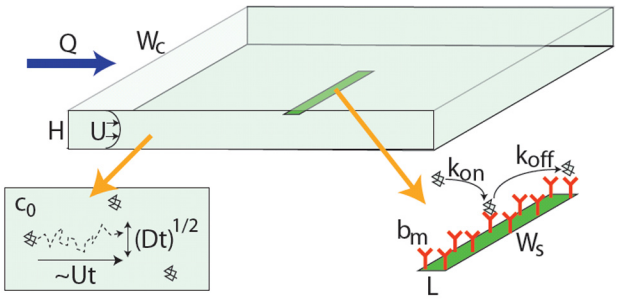

▲ Figure 1: Model system studied here. Solution with target concentration c_0 flows with rate Q ~ H Wc U through a channel of height H and width Wc over a sensor of length L and width Ws that is functionalized with bm receptors per unit area. The kinetic rate constants for the (first-order) binding reaction are k_{on} and k_{off}, and the diffusivity of the target molecules is D.

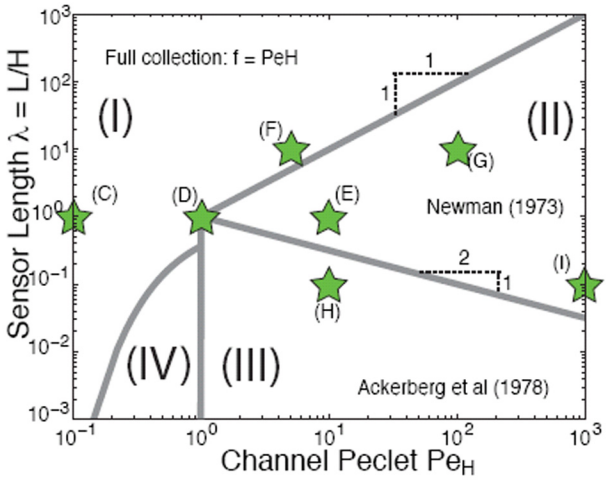

▲ Figure 2: "Phase diagram" for mass transport in our model sensing system. "Full collection" occurs at sufficiently low Pe_H, corresponding to region I. In region II, a depletion zone forms that is thin compared to both the sensor length L and the channel height H. In region III, the depletion zone is thinner than the channel, but thicker than the sensor. Region IV has not, to our knowledge, been studied thus far. The boundaries between these regions are described in Supplementary Notes of [1]. Stars correspond to concentration profiles (C)-(I) shown in Figure 3 of [1].

Reference

[1] T.M. Squires, R.J. Messinger, and S.R. Manalis, "Making it stick: convection, reaction and diffusion in surface-based biosensors," *Nature Biotechnology*, vol. 26, no. 4, pp. 417-426, Apr. 2008.

Iso-dielectric Separation of Cells and Particles

M.D. Vahey, J. Voldman

Sponsorship: NIH NIBIB, MIT Buschbaum Fund, Singapore-MIT Alliance, CSBi/Merck Graduate Fellowship

The electrical properties of cells and particles offer insight into their composition and structure as well as provide an intrinsic handle upon which separations can be based. Over the past several decades, dielectrophoresis (DEP) [1], electrorotation [2], and impedance spectroscopy [3] have been used to characterize the electrical properties of cells. Not surprisingly, these techniques – in particular, DEP - have also proven effective for cell sorting [1]. One significant barrier in developing effective electrical sorts of cells, however, is our relatively poor understanding of cells' electrical properties and how they vary under different environmental conditions. Better understanding of how phenotype and genotype manifest themselves through the electrical properties of a cell under different environmental conditions is crucial for developing new screens. Towards this end, we have created a separation method – iso-dielectric separation, or IDS – that separates continuous streams of cells and particles according to their intrinsic dielectric properties [4, 5].

Iso-dielectric separation uses dielectrophoresis (DEP) and a medium with spatially varying conductivity to sort cells according to their effective conductivity (Figure 1). It is similar to iso-electric focusing, except that it uses DEP instead of electrophoresis to concentrate cells and particles to the region in a conductivity gradient where their polarization charge vanishes [6]. The IDS leverages many of the advantages of microfluidics and equilibrium gradient separation methods to create a device that is continuous-flow, capable of parallel separations of multiple (>2) subpopulations from a heterogeneous background, and label-free. Additionally, because IDS offers analog separation of cells and particles according to their intrinsic properties, it can be also be used as a platform to characterize particles. We have demonstrated the separation and characterization of particles ranging from polystyrene beads, to the budding yeast Saccharomyces cerevisiae, to mouse pro B cells (Figure 2), representing three orders of magnitude in particle volume (~1-1000 μm^3) and conductivity (~0.001–1 S/m).

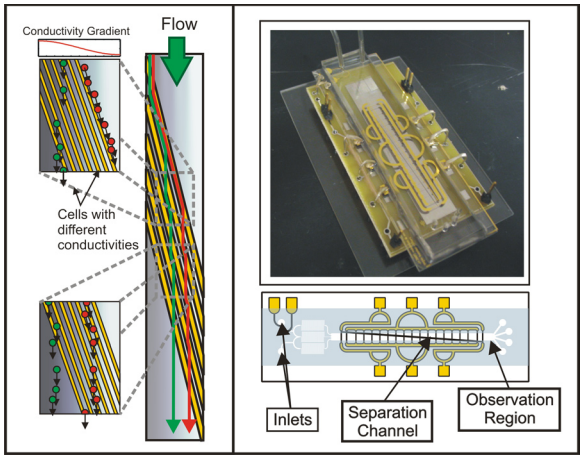

▲ Figure 1: (Left) Illustration of IDS, depicting cells with different electric properties following different trajectories in a conductivity gradient. (Top right) Photograph of an assembled device. (Bottom right) Schematic of the device highlighting its primary components.

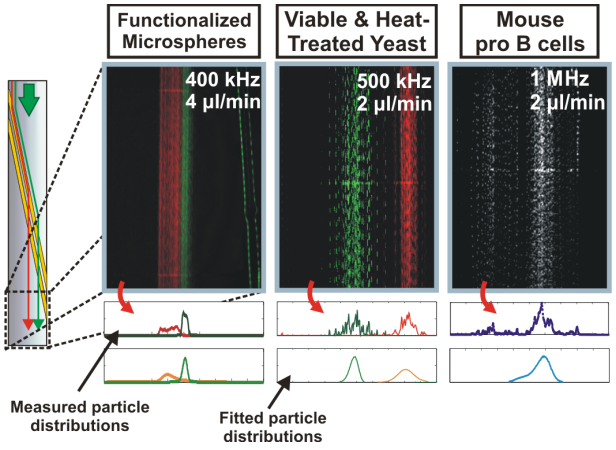

▲ Figure 2: Separation and characterization of cells and particles using IDS. By measuring the spatial distribution of cells as they exit the device under different conditions and fitting to these distributions, we are able to quantify physical and physiological properties.

References

[1] P.R.C. Gascoyne and J. Vykoukal, "Particle separation by dielectrophoresis," *Electrophoresis*, vol. 23, pp. 1973-1983, 2002.
[2] R. Holzel, "Electrorotation of single yeast cells at frequencies between 100 Hz and 1.6 GHz," *Biophysical Journal*, vol. 73, pp. 1103-1109, 1997.
[3] T. Sun, D. Holmes, S. Gawad, N.G. Green, and H. Morgan, "High speed multi-frequency impedance analysis of single particles in a microfluidic cytometer using maximum length sequences," *Lab on a Chip*, vol. 7, no. 8, pp. 1034-1040, Aug. 2007.
[4] M.D. Vahey and J. Voldman, "An equilibrium method for continuous-flow cell sorting using dielectrophoresis," *Analytical Chemistry*, doi: 10.1021/ac7020568.
[5] M.D. Vahey and J. Voldman, "Iso-dielectric separation: A new method for the continuous-flow screening of cells," *Micro Total Analysis Systems '06*, vol. 2, pp. 1058-1060, 2006.
[6] H.A. Pohl and J.S. Crane, "Dielectrophoresis of cells," *Biophysical Journal*, vol. 11, pp. 711-727, 1971.

Sub-cellular, Precision, On-chip Immobilization, Imaging, Manipulation, and Sorting of Small Animals

C.B. Rohde, F. Zeng, C.L. Gilleland, M.F. Yanik
Sponsorship: NIH, Merck/CSBi, NSF, NSERC

Today, pharmacological drug and genetic screens require use of in-vitro cell cultures due to the absence of high-throughput technologies for studying whole animals. However, isolated cells do not represent truly the physiology of live animals, and many multi-cellular processes cannot be screened using cell cultures alone. Although small-animal studies have significantly impacted cellular biology and continue to do so, the lack of techniques for rapid and high-throughput observation and manipulation of sub-cellular features in live animals has significantly limited the use of small-animal assays for drug/genetic discoveries. We have recently invented and developed the first technologies to conduct critical high-throughput drug/genetic studies on whole animals at cellular resolution at unprecedented speeds [1, 2]. These technologies can greatly accelerate drug discovery using small animals for target identification and validation as well as compound mode-of-action screens.

Using microfluidic large-scale-integration techniques, we enable sub-cellular precision high-throughput screening of *C. elegans*, a small semi-transparent nematode that is a powerful model organism for studying a wide variety of biological phenomena. We have created a whole-animal sorter (Figure 1a), which makes use of single and multiple suction channels and an additional control layer to isolate and immobilize a single animal from a group. A microfluidic valve is opened at the input, and the circulating animals enter the sorter. A single small suction channel held at a low pressure is used to capture a single worm, and the remaining animals are washed away. The single worm is then partially immobilized in a straight configuration using multiple aspiration channels on the opposite site of the sorter. The aspiration immobilizes animals only partially, and it is not sufficient to completely restrict their motion. In order to fully immobilize the animals, we create a seal around them that restricts their motion completely. This is done by using a flexible sealing membrane that separates a press-down channel from the flow channel underneath. The press-down channel can be rapidly pressurized to expand the thin membrane downwards. The membrane flexes on top of the captured animals, wrapping around them and forming a tight seal that completely constrains their motion in a linear orientation (Figure 1b). Although the animals are constrained by the PDMS membrane from the top and bottom, they still have access to liquid media via the multiple aspiration channels on the side. The stability of the immobilization is comparable to that achieved using anesthesia, which allows imaging using high-magnification optics (Figure 1c) as well as the use of advanced techniques including femtosecond microsurgery and multi-photon imaging, both of which we have demonstrated on-chip [2]. The ability to flow worms at a high density, combined with the high actuation speed of the valves, means that animals can be isolated and immobilized for analysis very quickly and sorted based on highly complex phenotypes.

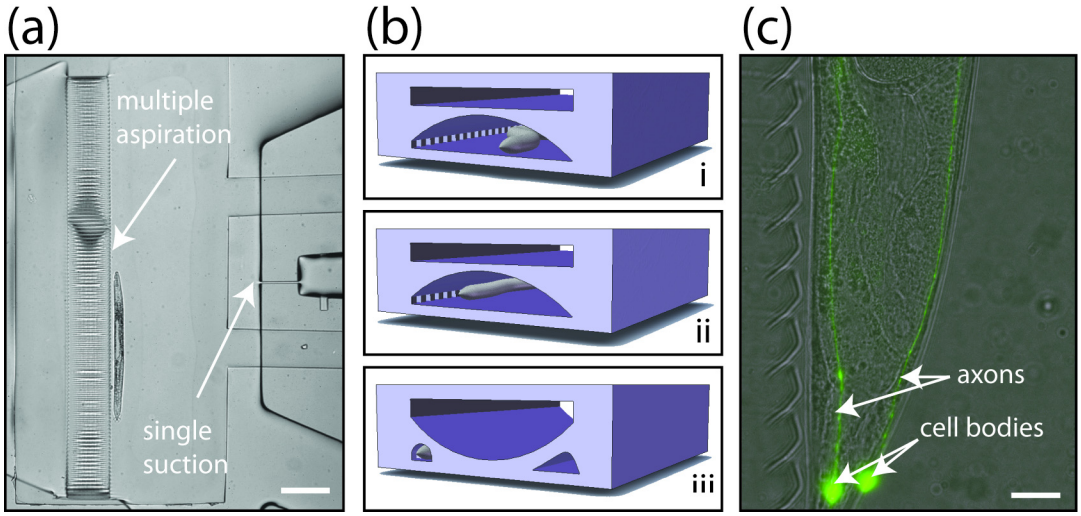

▲ Figure 1: Microfluidic immobilization of *C. elegans*. (a) Microfluidic worm sorter structure, illustration of single suction and multiple aspiration ports (scale bar 250 µm). (b) Illustration of the immobilization process. (c) Close-up of immobilized pmec-4::gfp animal, showing gfp-labeled fluorescent posterior lateral mechanosensory (PLM) neurons (scale bar 20 µm).

References

[1] C.B. Rohde, F. Zeng, R. Gonzalez-Rubio, M. Angel, and M.F. Yanik, "Microfluidic system for on-chip high-throughput whole-animal sorting and screening at sub-cellular resolution," *Proc. of the National Academy of Sciences*, vol. 104, no. 35, pp. 13891-13895, Aug. 2007.

[2] F. Zeng, C.B. Rohde, and M.F. Yanik, "Sub-cellular precision on-chip small-animal immobilization, multi-photon imaging and femtosecond laser manipulation," *Lab on a Chip*, 2008, DOI: 10.1039/b804808h.

High-throughput pI-based Fractionation of Biological Samples in Microfluidic Chip for Mass Spectrometry

Y.-A. Song, J. Han

Sponsorship: NSF (CTS-0347348), IMC-KIST, CSBi/Merck Postdoctoral Fellowship

We have developed a microfluidic chip for pI (isoelectric point)-based fractionation of peptides and proteins as a sample preparation step for mass spectrometry (MS). The sorting chip with its multiple outlets allows continuous-flow binary sorting of the proteomic samples into positively and negatively charged molecules without using any carrier ampholytes (Figure 1a). When coupled with pH titration, two fractionation steps enable us to isolate molecules within a predetermined pI range from proteomic sample mixtures [1]. The pI information of the isolated molecules that is not provided by the standard ion-exchange chromatography can lead to a substantial reduction of peptide sequencing time in shotgun proteomics [2].

The electrical junction inside the sorting chip was created simply by patterning multiple submicron-thin hydrophobic layers on glass substrate prior to plasma bonding with the PDMS chip (Figure 1b). To demonstrate the sorting capability, we used three pI markers, 10.3, 8.7 and 6.6, in 20mM phosphate buffer solution with pH 8.4. As Figure 1c) shows, three bands were clearly visible in presence of an electric field of 200 V/cm. We could also separate two different proteins, GFP and R-Phycoerythrin, differing by only 0.5 pI units, into two streams (Figure 1d). In addition, we demonstrated the high-throughput capability of the device by processing raw samples at 1 µL/min, which is sufficient for downstream, standard biomolecule assays such as MS.

We validated the two-step sorting result of a peptide mixture, pI 9.7, pI 7.2 and pI 5.1, into three different fractions with the MALDI-MS. As Figure 2 shows, pI 7.2 (falling between pI 6-8) could be isolated from the mixture. The test of the device with more complex samples such as human serum will ultimately demonstrate its potential in sample preparation for mass spectrometry. Its successful development will have a significant impact on MS-based bioanalysis.

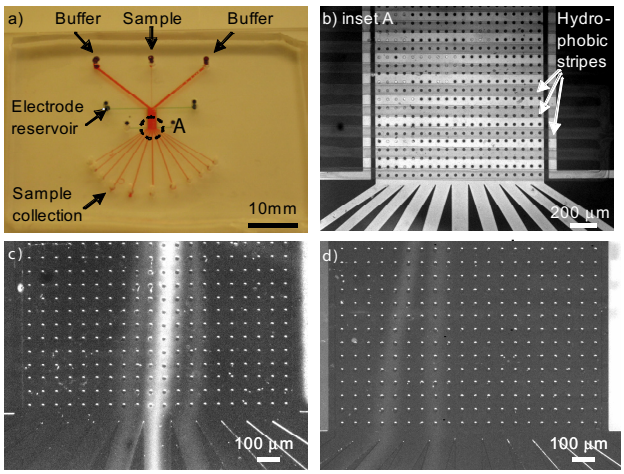

▲ Figure 1: a) The pI-based sorting chip in PDMS with multiple outlets for collection of fractionated sample. b) Multiple hydrophobic layers patterned on glass substrate create electrical junctions. c) Separation of three pI markers (pI 10.3, 8.7 and 6.6) at pH 8.4, 1 µL/min sample flow rate, 4 µL/min sheath flow rate, applied field strength of 200 V/cm at 500 µA. d) Continuous-flow separation of GFP and R-phycoerythrin at pH 6.0, 200 V/cm and 0.5 µL/min.

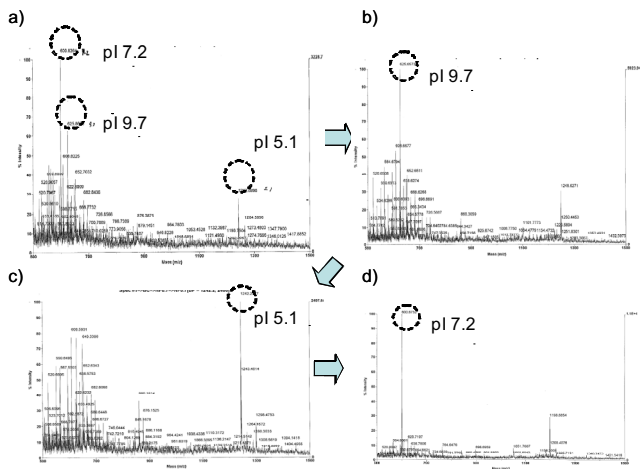

▲ Figure 2: The MALDI-MS result for the two-step sorting of three peptides (pI 9.7, 7.2 and 5.1). a) Original mixture with 100nM concentration for each peptide. b) In the first sorting step at pH 8.0, the positively charged peptide, pI 9.7, was removed from the mixture. c) In the second sorting step at lower pH value, pH 6.0, negatively charged pI 5.1 was removed from the mixture. d) The remaining pI 7.2, which falls between pI 6-8, was collected out of the peptide mixture.

References

[1] Y.-A. Song, C. Celio, and J. Han, " Continuous-flow pi-based sorting of proteins and peptides for isolation of basic pI range molecules," in *Proc. Eleventh MicroTAS 2007 Symposium*, Paris, France, Oct. 2007, pp. 811-813.

[2] M. Washburn, D. Wolters, and J.R.Yates III, "Large-scale analysis of the yeast proteome by multidimensional protein identification technology," *Nature Biotechnology*, vol. 19, pp. 242-247, Mar. 2001.

Microfabricated Devices for Sorting Cells Using Complex Phenotypes

S. Desai, J. Kovac, B. Taff, J. Voldman

Sponsorship: NIH, Department of Defense Graduate Research Fellowship, Singapore-MIT Alliance

This research involves the development of sorting cytometer architectures for genetic screening of complex phenotypes in biological cells. Our approaches combine the ability to observe and isolate individual mutant cells within surveyed populations. In this work we merge the benefits of microscopy and flow-assisted cell sorting (FACS) to offer unique capabilities in a single platform. Biologists will leverage this flexibility to isolate cells based upon imaged dynamic or intracellular responses

Our most recent electrical approach to image-based sorting [1] combines microfabricated weir structures and their efficient single-cell capture mechanics with negative dielectrophoretic (n-DEP) actuation (Figure 1). In these designs, we "pin" individual cells in designated on-chip locations using "capture cups" formed from a photopatterned silicone polymer [2]. Negative DEP forces then operate as a switch to unload targeted subgroups of the weirs and prevent site-specific loading altogether in arrayed weir grouping. This functionality enables the placement of multiple cell types in organized single-cell patterns on a common substrate, permitting new screening and response assays for cell-cell signaling dynamics. With this platform, manipulations prove feasible in standard cell-culture media, thus avoiding cell health concerns associated with comparative p-DEP approaches.

We have also continued developing our optical approach to image-based cell sorting. In this approach, cells are captured in a 10,000-site silicone microwell array. Following imaging, we use an infrared laser to levitate and thus sort cells out of microwells. Over the past year we have demonstrated the ability to purify cell populations up to >150× as well as sort cells based upon a localization-based phenotype [3].

Additionally, we are investigating the effects of DEP manipulation on cell physiology using a microfabricated, high-content screening (HCS) platform that applies electrical stimuli to cells and monitors the resulting subcellular molecular responses via automated fluorescence microscopy. The platform consists of a chip with individually addressable arrayed electrodes and peripheral support electronics (Figure 2). We seed cells onto the chip and then expose them to a variety of electrical stresses. By monitoring the response of the cells via a fluorescent reporter cell line, we can assess how cells respond to the electric fields.

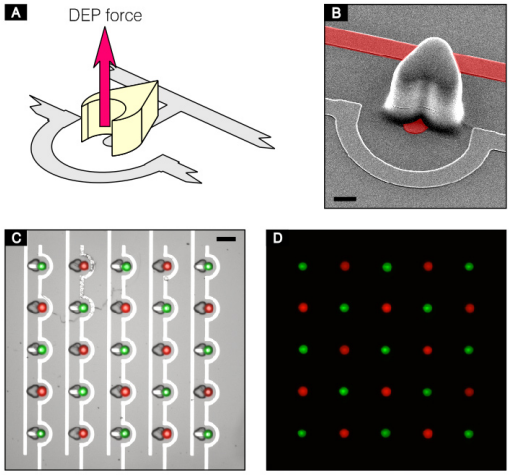

▲ Figure 1: A combined n-DEP/weir cell-sorting platform.(A) Schematic showing cell "capture cups" (yellow) aligned to underlying electrodes (gray). Cells flow into the "cups" via fluid flow and n-DEP forces enable unloading. (B) An SEM of (A) - scale bar = 10 µm. (C) Dual-color bead patterning as enabled by this new achitecture: merged bright field (BF) and fluorescence signals, scale bar = 50 µm. (D) Highlighted version of image (C) showing fluorescence alone.

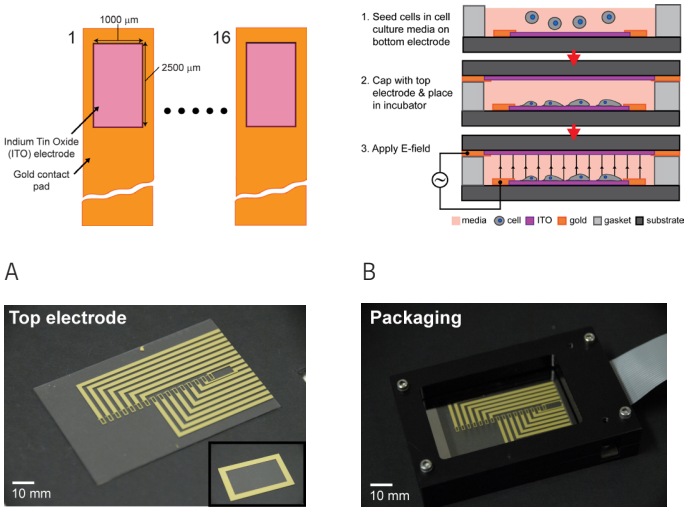

▲ Figure 2: HCS platform. (A) Top-down schematic of 16 individually addressable transparent indium-tin oxide (ITO) electrodes. (B) Seeding of cells on electrodes and running the screening assay. (C) Images of bottom electrode (left panel) and top electrode chips (inset). Image of packaged device (right panel), showing bottom electrode chip visible through transparent top electrode.

References

[1] B.M. Taff, S.P. Desai, and J. Voldman, "Dielectrophoretically switchable microfluidic weir structures for exclusion-based single-cell manipulation," in *Proc. of Eleventh International Conference on Miniaturized Systems for Chemistry and Life Sciences*, Paris, France, Oct. 2007, pp. 8-10.

[2] S.P. Desai, B.M. Taff, and J. Voldman, "A photopatternable silicone for biological applications," *Langmuir*, vol. 24, no. 2, pp. 575-581, Jan. 2008.

[3] J.R. Kovac and J. Voldman, "Intuitive, image-based cell sorting using optofluidic cell sorting," *Analytical Chemistry*, vol. 79, no. 24, pp. 9321-9330, Nov. 2007.

Inkjet Stimulation of Neurons

L. Theogarajan, M.A. Baldo

Electrical excitation is the standard method for stimulating neural tissue [1]. Although widely used, it is not the most efficient method. We have been investigating the use of potassium ions as a method of stimulating neural tissue. The use of ionic stimulation allows for a more biocompatible and low-power method of stimulation. Initial in-vitro experiments on rabbit retina show that a modest increase (~10mM) of extracellular potassium ion concentration elicits neural responses.

Our initial experiments were performed by pressure ejection of KCl using a multi-barrel glass pipette and performed on the epi-retinal side of the retina [2], as in Figure 1. However, the final envisioned device will be situated in the sub-retinal space. Furthermore, a different in-vitro experimental platform needs to be designed to overcome the limitations of the existing setup. Furthermore, a device that allows for ejection of very small volumes (pL compared to nl) and also allows for accurate estimation of volumes ejected would greatly enhance the development of a prosthetic device using this concept. An additional advantage of ionic stimulation over electrical stimulation, as an investigation tool for neuroscience, is that ionic stimulation does not induce a stimulus artifact that allows for simultaneous recording from multiple neurons.

Thus, it would be advantageous to build an ionic stimulation platform that has the capability of array stimulation. Inkjet printing technology naturally lends itself to this endeavor and is the platform of choice for our device. Figure 2 illustrates the scheme . However, our initial experiments using thermal inkjet technology met with failure for reasons including inkjet head construction and chamber size. Simple experiments performed using a piezoelectric inkjet head showed more promise and we are currently building a custom in-vitro stimulation platform using a piezoelectric inkjet head controlled by custom electronics and using a software platform based on LabView.

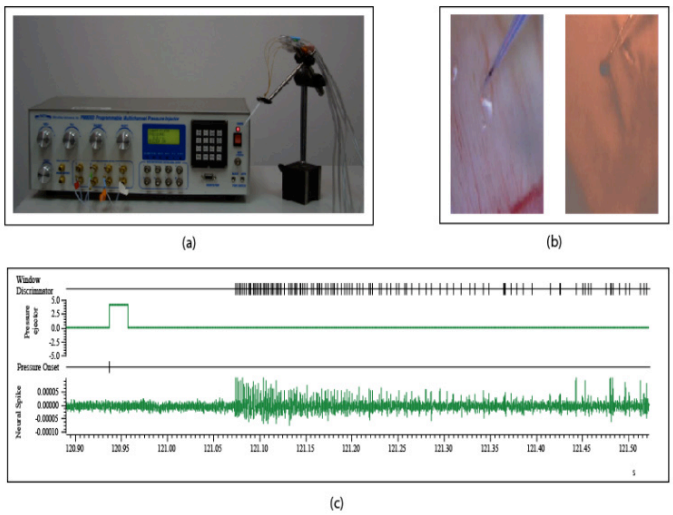

▲ Figure 1: a) Experimental setup used for the K+ stimulation. b) Snapshots of the pipette positioned over the retina; the figure with a red shading is the pipette under red light illumination and shows the KCl solution being ejected with the dark stain caused by the Azure B dye used for visualization. The red light was used to prevent the retina from responding to the ambient light since it is known that rabbit retinae do not respond to red light. c) Typical response to K+ stimulation. Shown is the response to concentration of 30mM KCl. The square pulse is the onset of the ejection.

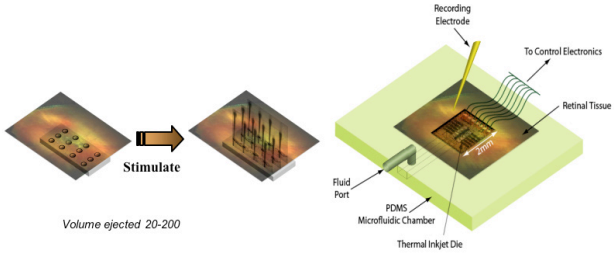

▲ Figure 2: Inkjet stimulation platform for accurate determination of ejected volumes and multi-point stimulation. (See text for more details.)

References

[1] L. Theogarajan et al., "Minimally invasive retinal prosthesis," ISSCC Digest of Technical Papers, 2006, pp. 99-102.

[2] L. Theogarajan, R. Jensen and J.F. Rizzo, "Stimulation of rabbit retinal ganglion cells by altering K+ ion gradients: Dose-response curve," *Investigative Ophthalmology & Visual Science*, vol. 45, sup. 2, pp. U401-U401, Apr. 2004.

Flexible Multi-site Electrodes for Moth Flight Control

W.M. Tsang, A.I. Akinwande, J. Voldman
Sponsorship: DARPA

Significant interest exists in creating insect-based Micro-Air-Vehicles (MAVs) that would combine advantageous features of insects—small size, relatively large payload capacity, navigation ability—with the benefits of MEMS and electronics—sensing, actuation and information processing. In this work, we have developed a flexible electrode array that provides multi-site stimulation in the moth's abdominal nerve cord. These flexible multi-site electrodes (FMEs) are implanted into moth (Manduca Sexta) pupae and directly interface with the central nervous system (CNS) of the moths for flight control.

The FMEs are composed of two layers of polyimide with gold sandwiched in between and have 4 – 8 stimulation sites (Figure 1). The FMEs have a split-ring design that allows the FME to encircle the nerve cord, and the electrodes on the FME are on flexible tabs that protrude into the split ring and can bend back to make good contact with the nerve cord. The split-ring and tab design makes the FME adaptable to a wide range of nerve cord diameters, maintaining good contact as animals undergo metamorphosis and the nerve cord diameter increases.

These FMEs were inserted into pupae as early as 7 days before the adult moth emerges and could stimulate pupae and adult moths. In pupae, we observed abdominal flexion using square wave pulses of ≥4 volts at various pairs of the stimulation sites, and similar behavior was observed in tethered adult moths. The electrode implantations and stimulation experiments were performed by our collaborators at the University of Arizona and University of Washington, respectively. Finally, in loosely tethered flight, we have used this abdominal ruddering to cause the normally hovering moth to change its abdominal angle, leading to a change in flight direction (Figure 2). This demonstrates our ability to create MEMS-based electrodes that can be implanted in pupae, directly interface with the CNS, and enable control of insect flight.

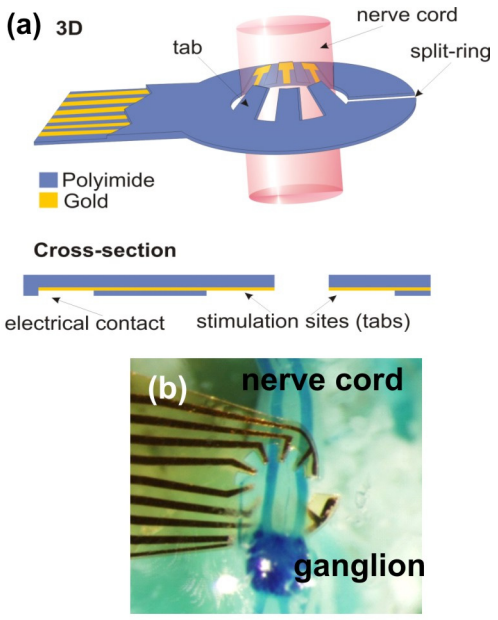

▲ Figure 1: (a) Schematic and (b) photograph show the electrode inserted in the CNS of a pupa.

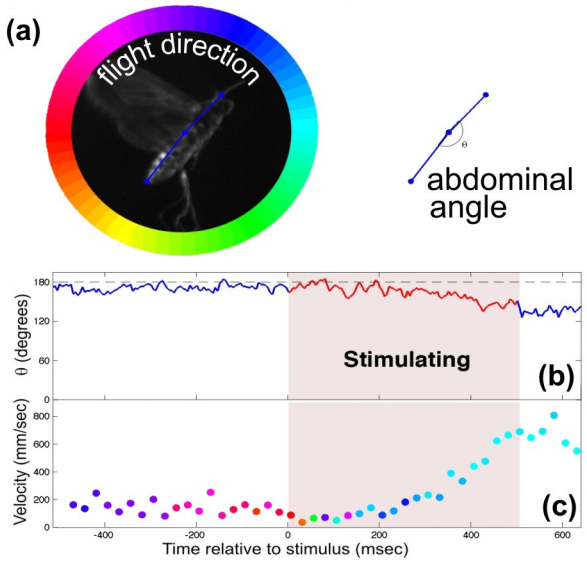

▲ Figure 2: Flight control of a loosely tethered adult moth: (a) Definitions of flight direction (colored circle) and abdominal angle (θ) of the moth; (b) Variation of the abdominal angle and (c) The magnitude and direction of the moth's velocity (the colors indicate the direction) with stimulation. Upon stimulation of the insect, the velocity increases and the flight direction of the moth changes from up-and-to-the-left to directly right, and both coincide with a change in angle caused by the flexion of the abdomen.

Protein Separation by Free-flow Isoelectric Focusing

J. Wen, J. Albrecht, E. W. Wilker, M.B. Yaffe, K.F. Jensen

Sponsorship: Department of Chemical Engineering, Center for Cancer Research, Department of Biology

Disposable, inexpensive microfluidic devices have the potential to become a robust new tool for proteomic research involving difficult proteins and protein complexes. In this work, a preparative scale free-flow IEF isoelectric focusing (FF-IEF) device was designed, investigated, and optimized. Prior work on micro FF-IEF has described devices with volumes in the range of 1-2 μL [1] and a flow rate of sub-microliters per minute. A larger FF-IEF device was developed to address the needs of molecular biologists working with samples of milligrams in mass and milliliters in volume. Earlier work [1] with IEF simulations has confirmed the advantages of using non-rectilinear channel geometries. Here we present a triangular-shaped preparative IEF device fabricated by soft lithography in PDMS and having 24 outlets. The triangular design facilitates the development of the pH gradient with a corresponding increase in separation efficiency and decrease in focusing time.

The unique design of a triangular separation channel required the electric fields across the central channel to be optimized. After the shaping of the PDMS prior to the device binding, a functionalized polyacrylamide gel region at the bottom of the device was selectively controlled to adjust the ratio of the applied potential across the separation channel (Figure 1). At the device depth of 160 mm, the electric fields of as high as over 300 V/cm could be achieved. To further investigate the separation of the protein complex mixture on the microdevice, whole cell lysate of U20S was applied and separated under denaturing conditions. To validate the performance of the free-flow IEF separation, selective fractions representing the acidic, neutral, or basic region were run on a traditional 2D gel. As Figure 2 shows, effective isolation of acidic (blue), neutral (green), and basic (orange) proteins from the whole cell lysate was achieved. High-molecular-weight proteins were retained by FF-IEF (shown in the blue box), but they are mostly missing from the 2D gel separation.

Thus using the IEF device is an advantage for biologists interested in high-molecular-weight proteins, which presently are difficult to isolate with conventional IEF-strip 2D gel techniques. The devices can process complex biological samples and fractionate whole cell lysate at rates between 10-30 uL/min while providing greater separation of traditionally difficult proteins. These findings show the promise of inexpensive, disposable microfluidic FF-IEF devices in proteomics research.

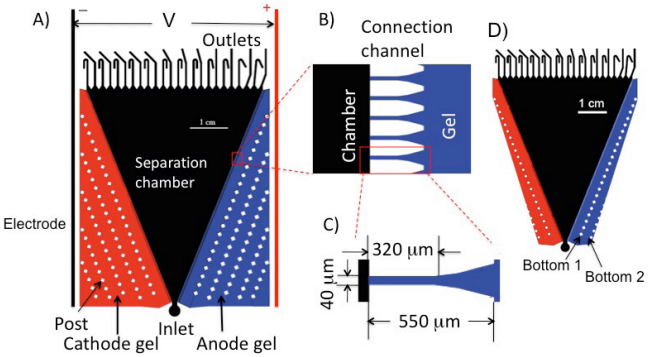

▲ Figure 1: A) Mask design of free-flow IEF device. The device was 5 cm by 7.5 cm with the center triangle separation chamber of 4 cm in width and 5.2 cm in height. Functionalized pH gradient cathode (pK=9.3) and anode (pK=3.6) polyacrylamide gels were polymerized into the gel regions, which were connected to the separation chamber. B) Detail of channel array. C) Channel dimensions: 0.32 by 0.04 mm. D) The regions of functionalized gels can be adjusted for individual devices.

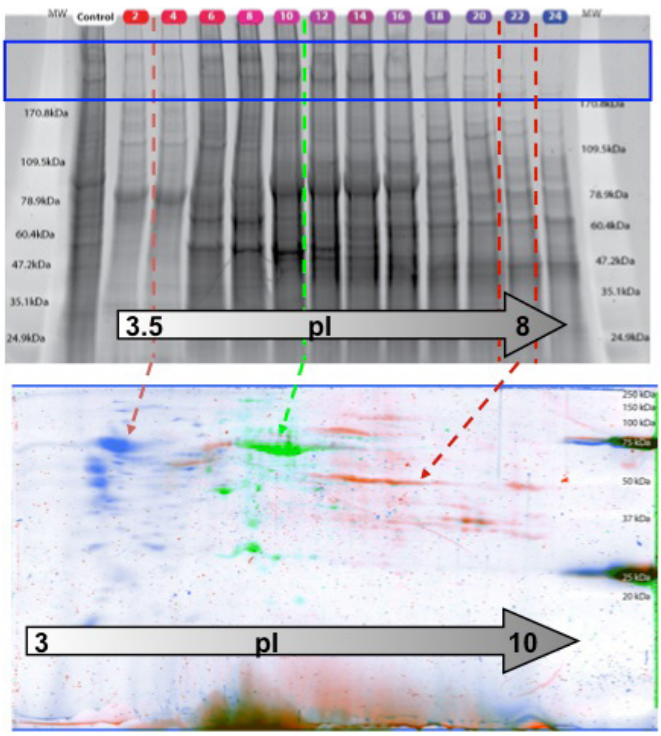

▲ Figure 2: Focusing of U20S cell lysate with FF-IEF followed by 2-D electrophoresis. Acidic, neutral, and basic fractions of 3, 11, and 21+23 were further run on a conventional 2D gel to show the effectiveness of the FF-IEF separation.

Reference

[1] J.W. Albrecht, J. El-Ali, and K.F. Jensen. "Cascaded free-flow isoelectric focusing for improved focusing speed and resolution," *Analytical Chemistry*, vol. 79, no. 24, pp. 9364-9371, 2007.

Multiplexed Comet Assay for DNA Damage and Repair

D.K. Wood, D.M. Weingeist, J.T. Mutamba, B.P. Engelward, S.N. Bhatia

Sponsorship: Biological Response Indicators of Environmental Stress (U01), National Institute of Environmental Health Sciences

The use of DNA damage as a biomarker with predictive value for cancer and other diseases requires the development of a robust assay that enables routine assessment of DNA damage levels in human samples. Many applications, such as toxicity testing and epidemiological studies, require an assay that is capable of testing many conditions or many samples in parallel. To this end, we are developing a high-throughput version of the comet assay, a well-known assay for DNA damage. The basic principle of the assay is that undamaged DNA is supercoiled and highly compact, whereas damaged DNA is composed of relaxed loops and fragments and is more mobile when electrophoresed in an agarose gel. Our assay offers many distinct advantages over other DNA damage assays, including a high level of sensitivity and the ability to detect multiple damage types. The assay can also be implemented as a measure of DNA repair kinetics. Despite the assay's apparent benefits, it has been underutilized because of poor reproducibility, both from laboratory to laboratory and from user to user, and the time- and labor-intensive process of performing the assay. The major goal of this project is to overcome this assay's limitations, such as its low throughput and poor reproducibility, to create a multiplexed assay for DNA damage and repair. The goal is a new tool that will be useful in a broad range of clinical, epidemiological, and experimental settings.

Cell micropatterning enables spatial encoding of assay conditions, and it vastly improves spatial utilization of chips over the case with randomly placed cells. Both of these features are critical to a truly multiplexed assay platform. We have implemented single-cell micropatterning using microwells[1-2] fabricated directly into agarose gel (Figure 1). A negative relief mold of the microwells is fabricated using photolithography of SU-8 on a silicon substrate. Molten agarose is applied to the mold and allowed to solidify, resulting in an agarose gel with patterned microwells. A cell suspension with $1-2\times10^6$ cells/ml is applied to the gel, and cells are allowed to settle into the wells by gravity. Afterwards excess cells are rinsed, leaving only cells contained in the microwells. Finally, another agarose layer is applied to encapsulate the cells and to contain the DNA during the comet assay. Examples of microarrayed comets appear in Figure 2. The size of the well is a tunable parameter, which allows us to control the number of cells trapped in a single well. Additionally, this method places the cells in the same focal plane, which facilitates automated imaging, and it gives control over the cell microenvironment. We are currently developing a method for applying multiple chemical damaging agents to a single comet chip. With 100% filling efficiency, 200-μm cell spacing requires only 4 mm² for 100 cells/condition, which would allow 200 conditions on a single comet chip (20×50 mm² imaged area). Combining a platform for applying multiple conditions with the existing comet chip would provide the first truly multiplexed assay for DNA damage.

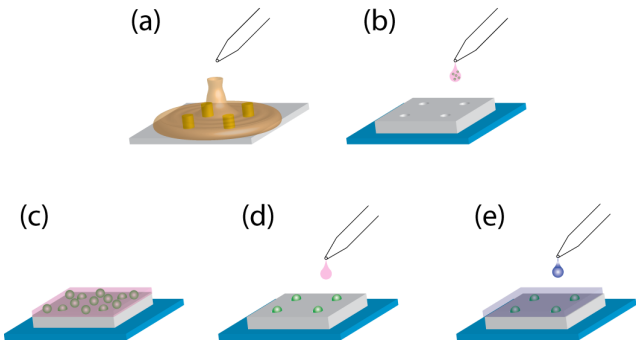

▲ Figure 1: (a) Single cell micropatterning using agarose microwells. Molten agarose is allowed to solidify on a master of silicon with SU-8 posts. (b) Single cell suspension is applied to agarose microwells. (c) Cells are allowed to settle into wells. (d Excess cells are washed away. (e) The microwells are capped with an agarose capping layer.

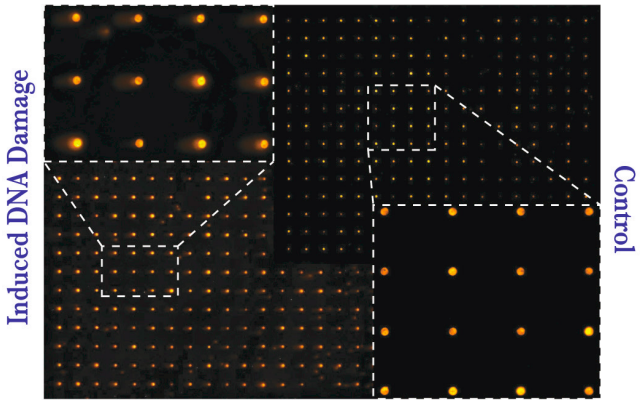

▲ Figure 2: Arrayed comets created using cell micropatterning method. Dose response is shown for TK6 lymphoblastoid cells treated with 1X DPBS (control) and 98 μM H_2O_2. Cells are arrayed with a 200-μm pitch, which was empirically determined to allow sufficient space for the comet tail. This demonstrates our ability to spatially encode DNA damage using micropatterning.

References

[1] J.R. Rettig and A. Folch, "Large-scale single cell trapping and imaging using microwell arrays," *Analytical Chemistry*, vol. 77, no. 17, pp. 5628-5634, Sept. 2005.

[2] A. Rosenthal, A. MacDonald, and J. Voldman, "Cell patterning chip for control of the stem cell microenvironment," *Biomaterials*, vol. 28, no. 21, pp. 3208-3216, July 2007.

Microfluidic Devices for Studying Early Response of Cytokine Signaling

L.L Ye, K.F. Jensen

This study presents the design, fabrication, and characterization of a microfluidic device (as shown in Figure 1) integrated with cell culture, cell stimulation, and protein analysis as a single device towards efficient and productive cell-based assay development. In particular, it demonstrates the feasibility of culturing human cancer cells in microliter-volume reactors in batch and fed-batch operations, stimulating the cell under well-controlled and reproducible conditions at early stages, and detecting the protein signals with an immunocytochemical (In-Cell Western) assay.

These microfluidic devices take advantage of microfabrication techniques to create an environment suitable for cell culture, biomechanical and biochemical stimulation of cells, and protein detection and analysis. The microfluidic approach greatly reduces the amounts of samples and reagents necessary for these procedures and the required process time compared with their macroscopic counterparts. Moreover, the technique integrates unit operations, such as cell culture, stimulation, and protein analysis, in a single microchip.

The microfluidic technique presented in this study correlates the space in the microchannels with the biological process time (cell stimulation time). Thus, a single experiment in one microfluidic device is capable of generating a multiple experimental complete temporal cell response curve, which otherwise would have required multiple experiments and manual assays by standard microwells and pipetting techniques. The developed method also provides high time-resolution and reproducible data for studies of cell signaling events, especially at early stages. These cell signaling events are difficult to investigate by conventional techniques.

This study reports the development not only of a cell population analysis method, but also of a single-cell detection and analysis technique to explore cell-to-cell variations. In this study, a new microscope stage holder was designed and machined, and an auto cell counting algorithm was developed for single-cell analysis. This single-cell method provided data on cell-to-cell variations and showed that the average cell signaling profiles were consistent with those by population-based analysis. The integration of single-cell imaging and microfluidic-enabled measurements shows promise as a technique for exploring cell signaling with single-cell resolution.

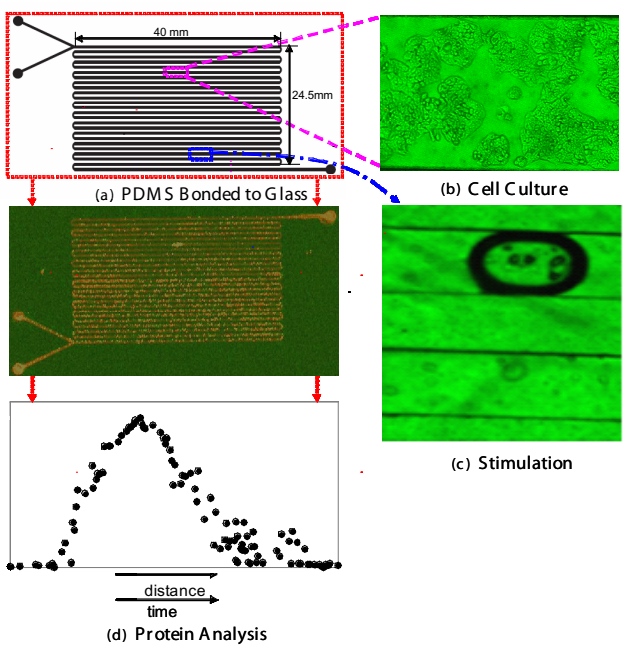

▲ Figure 1: Schematic of the microfluidic system

Micromechanical Actuators for Insect Flight Mechanics

H. Zhou, M.A. Schmidt (in collaboration with T.L. Daniel, University of Washington)
Sponsorship: DARPA

This project aims to develop MEMS actuators to aid in the study of insect flight mechanics. Specifically, we are developing actuators that can stimulate the antennae of the crepuscular hawk moth *Manduca Sexta*. The possible mechanosensory function of antennae as airflow sensors has been suggested [1], and recent discoveries of our collaborators reveal that mechanosensory input from the antennae of flying moths serves a similar role to that of the hind wings of two-winged insects, detecting Coriolis forces and thereby mediating flight stability during maneuvers [2]. Early evidence suggests that mechanical stimulus of the antennae may enable flight control. In addition, the crepuscular hawk moth *Manduca Sexta* has a wide wingspan (~110 mm) and is capable of carrying at least one quarter of its own weight. Thus, studying the flight of *Manduca Sexta* by attachment of microsystems seems plausible. The goal of our project is to design and fabricate micromechanical actuators, which will be mounted onto the moth antennae. Our collaborators will study the flight control mechanism by mechanical stimulation.

Our first step was to fabricate "dummy" silicon rings for our biologist collaborators for implant experimentation. Due to the nature of the moth antennae, ring-beam-ring construction was designed and fabricated, like a "shackle," to meet the mounting requirements [3]. Our current work focuses on integrating actuators onto the mounting kit. A piezoelectric-bender and piezoelectric-stack are considered the actuator (Figure 1). Live testing is also done while the moth is resting or flipping its wings (Figure 2). The moth apparently responds to the mechanical stimulus under both circumstances by swinging its wings and abdomen. Future work will refine the actuator design and quantitatively analyze the moth's reaction to the mechanical stimulation, which might lead to successful flight control of the moth.

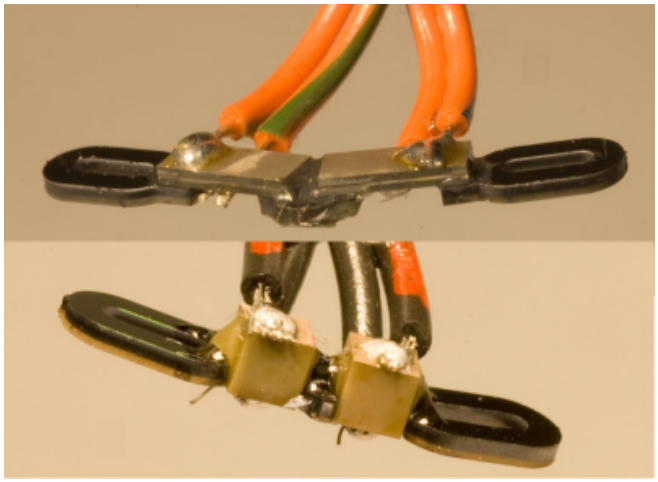

▲ Figure 1: Mounting kits made of silicon bases and piezoelectric benders (top) and piezoelectric stacks (bottom).

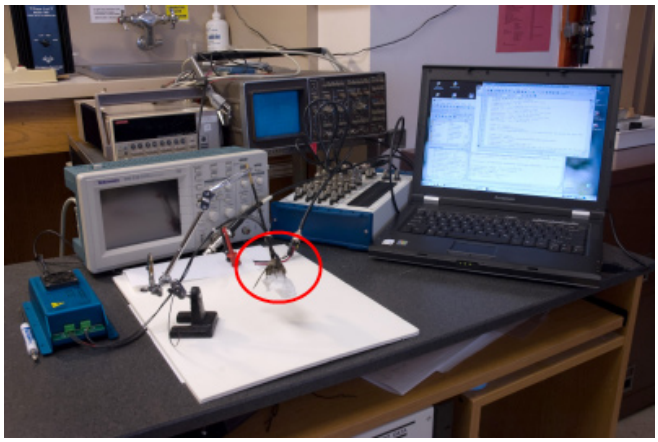

▲ Figure 2: Experimental setup for live testing (the moth is highlighted by a red circle, wearing the piezoelectric-stack "shackle").

References

[1] M. Gewecke, "Antennae: Another wind-sensitive receptor in locusts," *Nature*, vol. 225, no. 5239, pp. 1263-1264, Mar. 1970.
[2] S.P. Sane, A. Dieudonné, M.A. Willis, and T.L. Daniel, "Antennal mechanosensors mediate flight control in moths," *Science*, vol. 315, pp. 863-866, Feb. 2007.
[3] H. Zhou and M.A. Schmidt, "Micromechanical actuators for insect flight mechanics," Massachusetts Institute of Technology, Cambridge, MA, MTL Annual Research Report, 2007.

Biomimetically Inspired MEMS Pressure Sensor Assays for Passive Underwater Navigation

V.I. Fernandez, S.M. Hou, F.S. Hover, J.H. Lang, M.S. Triantafyllou
Sponsorship: NOAA: MIT Sea Grant College Program

A novel sensing technology for unmanned undersea vehicles (UUVs) is under development. The project is inspired by the lateral line sensory organ in fish, which enables some species to form three-dimensional maps of their surroundings [1, 2]. The canal subsystem of the organ can be described as an array of pressure sensors [3]. Interpreting the spatial pressure gradients allows fish to perform a variety of actions, from tracking prey [4] to recognizing nearby objects [2]. It also aids schooling [5]. Similarly, by measuring pressure variations on a vehicle surface, an engineered dense pressure sensor array allows the identification and location of obstacles for navigation (Figure 1). We are demonstrating proof-of-concept by fabricating such MEMS pressure sensors by using KOH etching techniques on SOI wafers to construct strain-gauge diaphragms.

The system consists of arrays of hundreds of pressure sensors spaced about 2 mm apart on etched silicon and Pyrex wafers. The sensors are arranged over a surface in various configurations (Figure 2). The target pressure resolution for a sensor is 1 Pa, which corresponds to the noiseless disturbance created by the presence of a 0.1-m-radius cylinder in a flow of 0.5 m/s at a distance of 1.5 m. A key feature of a sensor is the flexible diaphragm, which is a thin (20 μm) layer of silicon attached at the edges to a silicon cavity. The strain on the diaphragm due to pressure differences across the diaphragm is measured. At this stage, the individual MEMS pressure sensors are being constructed and tested.

In parallel to the construction of a sensor array, techniques are being developed to interpret the signals from a dense pressure array by detecting and characterizing wake structures such as vortices and building a library of pressure distributions corresponding to basic flow obstructions. In order to develop these algorithms, experiments are being performed on coarse arrays of commercial pressure sensors.

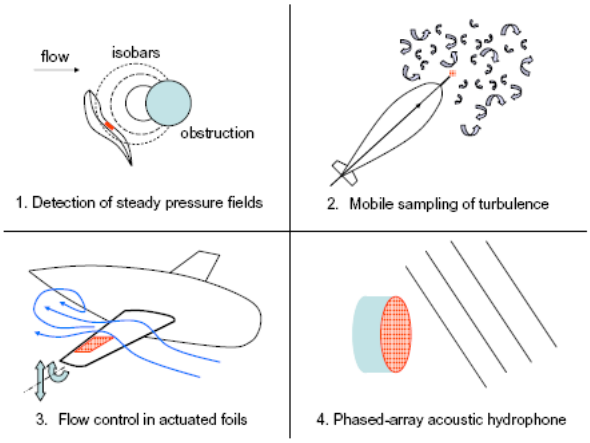

▲ Figure 1: Pressure-sensor array applications.

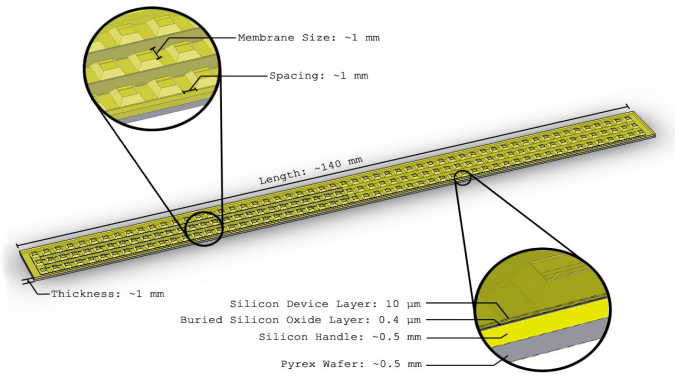

▲ Figure 2: Diagram of pressure-sensor array with basic structure depicted.

References

[1] J.C. Montgomery, S. Coombs, and C.F. Baker, "The mechanosensory lateral line system of the hypogean form of *Astyanax fasciatus*," *Environmental Biology of Fishes*, vol. 62, pp. 87-96, 2001.

[2] C. von Campenhausen, I. Riess, and R. Weissert, "Detection of stationary objects by the blind cave fish *Anoptichthys jordani* (Characidae)," *Journal of Computational Physiology A*, vol. 143, pp. 369-374, 1981.

[3] S. Coombs, "Smart skins: Information processing by lateral line flow sensors," *Autonomous Robots*, vol. 11, pp. 255-261, 2001.

[4] K. Pohlmann, J. Atema, and T. Breithaupt, "The importance of the lateral line in nocturnal predation of piscivorous catfish," *Journal of Experimental Biology*, vol. 207, pp. 2971-2978, 2004.

[5] T.J. Pitcher, B.L. Partridge, and C. S. Wardle, "A blind fish can school," *Science*, vol. 194, pp. 963-965, 1976.

Piezoelectric Micro-power-generator: MEMS Energy-arvesting Device for Self-powered Wireless Monitoring Systems

A. Hajati, S.-G. Kim

Sponsorship: NSF, Korean Institute of Machinery and Material

A novel thin-film lead zirconate titanate $Pb(Zr,Ti)O_3$ (PZT) MEMS energy-harvesting device is designed and developed for powering autonomous wireless sensors. It is designed to harvest energy from parasitic vibrational energy sources and convert it to electrical energy via the piezoelectric effect [1-4]. The new pie-shaped design always generates positive tension on the PZT layer and then positive charge output throughout vibration cycles. It produces mono-polarity output charge without using any additional bridge rectifier circuitry, which will be a huge cost saving for commercial production of scaled-up products. Contrary to the high-Q cantilever designs, the new design has a low-Q, doubly anchored beam design, which provides a wide bandwidth of operational frequency. This will enable more robust power generation even if the frequency spectrum of the source vibration varies unexpectedly. Furthermore, the beam shape is optimized to achieve uniform strain throughout the PZT layer [5].

In this new design, the whole thickness of the silicon wafer is used as the proof mass to increase the power of the generator. The fabrication includes CVD of 10-micron-thick oxide, followed by spin-coating, patterning, wet-etching, and annealing a thin ZrO2 layer as the diffusion barrier layer, followed by three layers of PZT. The top interdigitated electrodes are patterned by the lift-off method out of gold. A long BOE etching through the oxide followed by a DRIE of silicon from the wafer's back finalizes the device structure and releases the beams and proof mass (Figure 1). The SEM images of the released multi-beam cantilever beam design with a common heavy proof mass (an improved version of type-I PMPG) and a pie-shaped device with a center proof mass (type-II device) are imaged using scanning electron microscope (SEM) as shown in Figure 2.

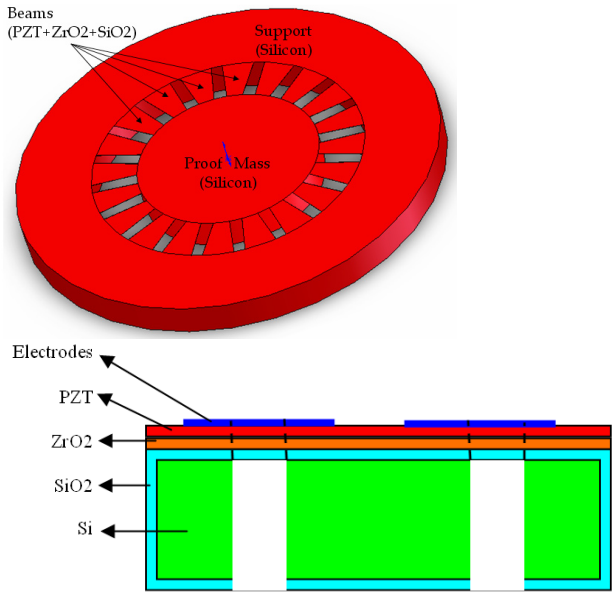

▲ Figure 1: The structure of the pie-shaped PMPG.

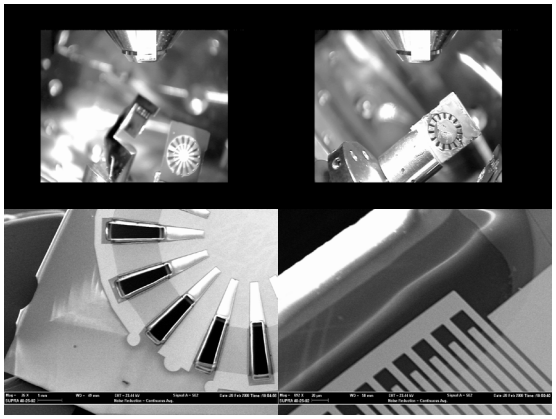

▲ Figure 2: SEM pictures of the released PMPG.

References

[1] Y.B. Jeon, R. Sood, J.H. Jeong, and S.-G. Kim, "MEMS power generator with transverse mode thin film PZT," *Sensors and Actuators A: Physical*, vol. 122, no. 1, pp. 16-22, July 2005.

[2] W.J. Choi, Y. Xia, J.A. Brewer, and S.-G. Kim, "Energy harvesting MEMS device based on thin-film piezoelectric cantilevers," in *Proc. of INSS05*, San Diego, CA, June 27-28, 2005.

[3] R. Xia, C. Farm, W. Choi, and S.-G. Kim, "Self-powered wireless sensor system using MEMS piezoelectric micro power generator," *Proc. IEEE Sensors 2006*, Daegu, Korea, 2006.

[4] W.J. Choi, Y. Jeon, J.-H. Jeong, R. Sood and S.-G. Kim, "Energy harvesting MEMS devices based on thin film piezoelectric cantilevers," *Journal of Electroceramics*, vol. 17, nos. 2-4, p. 543, 2006.

[5] A. Hajati and S.-G. Kim, "Rectifierless piezoelectric micro power generator," *SPIE Smart Structures and Materials & Nondestructive Evaluation and Health Monitoring 2008*, San Diego, CA, 2008

MEMS Vibration Harvesting for Wireless Sensors

W.S. Kim, M. Kim, M.Hoegen, F. Fachin, S.-H. Kim, A. Mracek, B.L. Wardle (in collaboration with S.-G. Kim)
Sponsorship: AFOSR, NSF Fellowship, Samsung Fellowship

The recent development of "low-power" (10's-100's of μW) sensing and data transmission devices, as well as protocols with which to connect them efficiently into large, dispersed networks of individual wireless nodes, has created a need for a new kind of power source. Embeddable, non-life-limiting power sources are being developed to harvest ambient environmental energy available as mechanical vibrations, fluid motion, radiation, or temperature gradients [1]. While potential applications range from building climate control to homeland security, the application pursued most recently has been that of aircraft structural health monitoring (SHM).

This SHM application and the power levels required favor the piezoelectric harvesting of ambient vibration energy, compared to other transduction principles. Current work focuses on harvesting this energy with MEMS resonant structures of various geometries. Coupled electromechanical models for uniform beam and plate structures have been developed to predict the electrical and mechanical performance obtainable from ambient vibration sources. The optimized models have been validated by comparison to prior published results [2] and verified by comparison to tests on a macro-scale device [3]. A non-optimized, uni-morph beam prototype (Figure 1) has been designed and modeled [4-5]. Dual optimal frequencies with equal peak power and unequal voltages and currents are characteristic of the response of such coupled devices when operated at optimal load resistances (Figure 2). Design tools to allow device optimization for any given vibration environment have been developed for both geometries. Future work will focus on fabrication and testing of optimized uni-morph and proof-of-concept bimorph prototype beams. This work will include system integration and development, including modeling the power electronics.

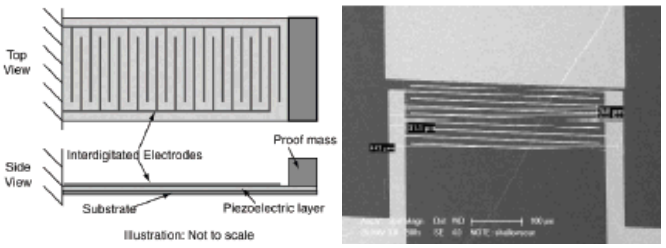

▲ Figure 1: Illustration of uni-morph energy-harvester configuration (left) and SEM of a prototype device.

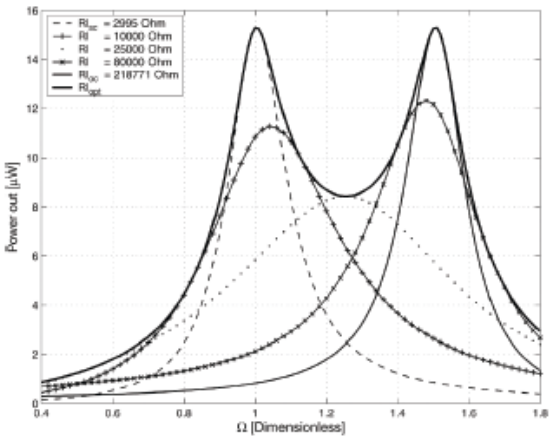

▲ Figure 2: Power vs. normalized frequency with varying electrical load resistance [4].

References

[1] S. Roundy, P.K. Wright, and J.M. Rabaey, *Energy Scavenging for Wireless Sensor Networks with Special Focus on Vibrations*, Norwell, MA: Kluwer Academic Publishers, 2004.

[2] H.A. Sodano, G. Park, and D.J. Inman, "Estimation of electric charge output for piezoelectric energy harvesting," *Strain*, vol. 40, no. 2, pp. 49-58, May 2004.

[3] N.E. duToit and B.L. Wardle, "Experimental verification of models for microfabricated piezoelectric vibration energy harvesters," *AIAA Journal*, vol.45, no.5, pp.1126-1137, May 2007.

[4] N.E. duToit, B.L. Wardle, and S.-G. Kim, "Design considerations for MEMS-Scale piezoelectric mechanical vibration energy harvesters," *Integrated Ferroelectrics*, vol. 71, pp. 121-160, 2005.

[5] N.E. duToit and B.L. Wardle, "Performance of microfabricated piezoelectric vibration energy-harvesters," *Integrated Ferroelectrics*, vol. 83, pp.13-23, 2007.

A Muscle-inspired Cellular Piezo Actuator

H.J. Lee, H. Lee, S.-G. Kim

Sponsorship: Korea Institute of Metallurgy and Manufacturing

A muscle-inspired linear actuator that combines many piezoelectric micro-actuator "cells" into a single functional collection is designed and fabricated via a folding assembly technique. A triplet of individually contractive MEMS actuator cells is designed and fabricated in series and three triplets are assembled by folding them out-of-plane around gold ribbon hinges. A triplet demonstrates peak unblocked displacement of 15.24μm, which is about 30 times amplification of the PZT strain at 10V stimulus. The loaded displacement measurements predict the 9.21μN blocking forces for the single triplet. Since the motion of the end effecter is linear and in plane, the device is arrayable in series. The use of flexible gold ribbon hinges and the folding method out-of-plane allows assembly of strings of actuators around the hinges [1].

The final goal of this study is to array these actuators massively in series and in parallel to make a linear actuator like an artificial muscle bundle. An improved folding assembly method such as a stacking assembly will be used to assemble hundreds of discrete piezoelectric MEMS actuators. This muscle-like actuator can be attached directly to the skeletal structure without tendon wires and additional transmission mechanisms, simplifying micro-robot systems.

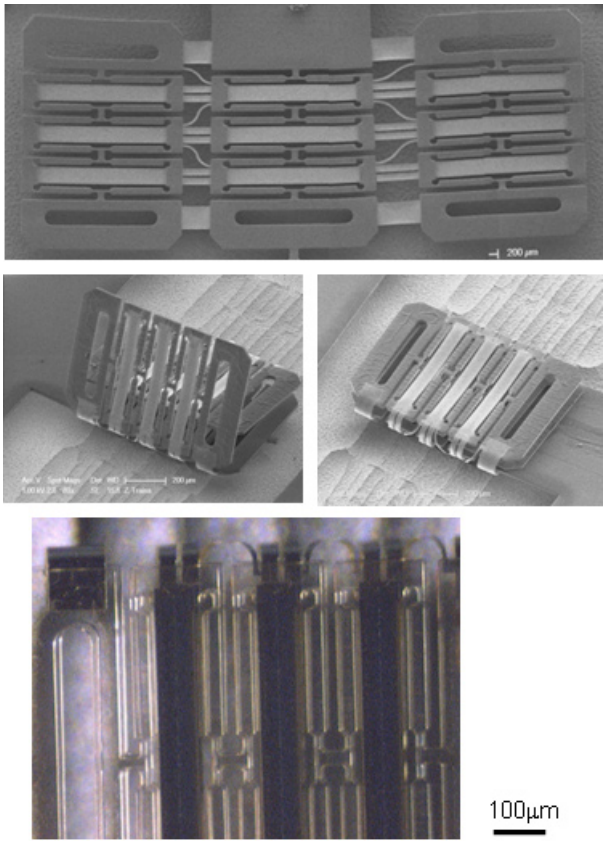

▲ Figure 1: Three unfolded triplet actuators (top), folding process (middle), and folded triplet actuators (bottom).

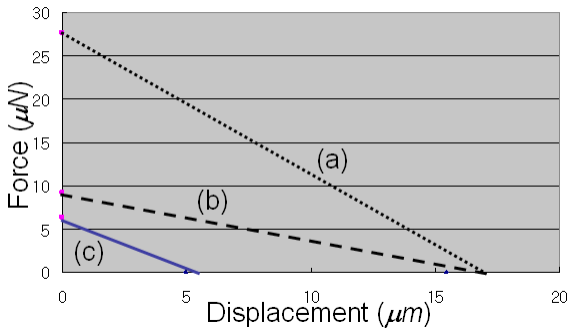

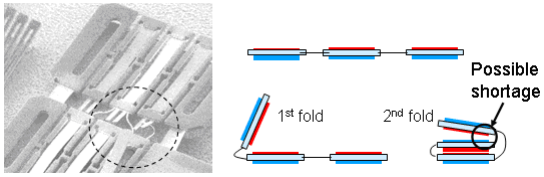

▲ Figure 2: Actuator performance curves of single triplet actuator (b), calculated (a) and measured (c) folded three triplet actuators (up), and possible defects (disconnection or shortage) causing low performance of actuator (below).

Reference

[1] S.-G. Kim, Z. Traina and H.W. Lee, "Folding assembly of microactuators," *Annals of the Journal of Manufacturing System*, 2008, to be published.

A System for Measuring Micro-scale Contact Resistance

M. Read, A. Weber, R. Martens, A.H. Slocum, J.H. Lang
Sponsorship: NSF

Designing devices utilizing micro-scale electrical contacts requires a precise knowledge of the relationship between contact force and contact resistance [1]. This relationship must be obtained experimentally because traditional contact theory does not always hold at the micro-scale, particularly at very low contact forces [2]. Additionally, this relationship has been shown to change with repeated cycling. The changes in this relationship are linked to physical changes of the contacts [3]. A system has been developed that measures the relationship between contact force and contact resistance for flat-on-flat micro-scale electrical contacts and also permits the contacts to be observed intermittently during testing [4]. This system is composed of two separate coupons, each containing a metal trace of the contact material and three KOH-etched pits. The coupons are assembled by placing stainless steel ball bearings into the KOH-etched pits of the bottom coupon and then placing the pits of the top coupon over the balls. An integrated flexure on the top coupon allows the metal traces to be brought into and out of contact, as shown in Figure 1. This kinematic coupling configuration allows the coupons to be assembled and reassembled with a repeatability on the order of a few microns [5]. During testing the metal traces are brought into contact while a load cell measures force and an integrated Kelvin structure measures contact resistance, as Figure 2 shows. This type of measurement has previously been used to measure the contact resistance of carbon nanotubes [6]. The contact surfaces are then separated and observed with an SEM. The cycle of repeated measurements and observation of the contact surface can be used to quantify the relationship between contact resistance and contact force and describe how this relationship and the physical attributes of the contact surface change with cycling.

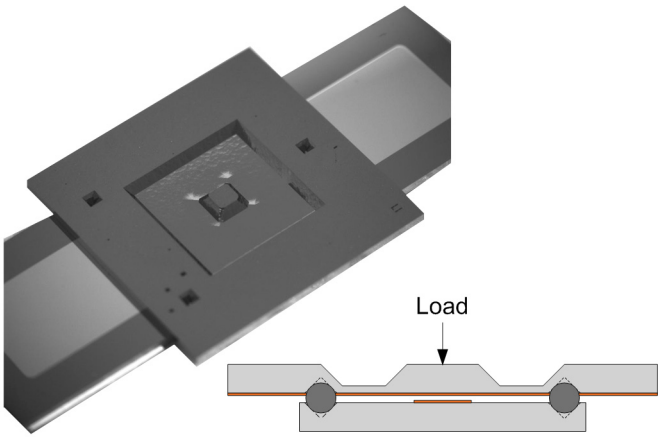

▲ Figure 1: An image of the completed device along with a schematic that shows how the metal traces are brought into and out of contact with each other when a load or displacement is applied to the integrated flexure within the top coupon.

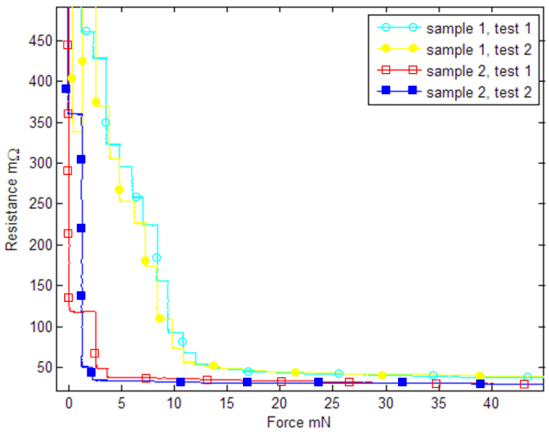

▲ Figure 2: The measurement of contact resistance versus contact force for two different devices with each test repeated twice. The contact material for both devices was 7000 Å of evaporated Au with a contact area of 4 mm^2. The differences between devices were attributed to contaminants found on device 1.

References

[1] A.C. Weber, J.H. Land, and A.H. Slocum, "The {111} Si etched planar electrical contacts for power MEMS-relays," in *Proc. 53rd IEEE Holm Conference on Electrical Contacts*, Pittsburg, PA, Sept. 2007, pp. 156-159.

[2] R.S. Timsit, "Electrical conduction through small contact spots," *IEEE Transactions on Components and Packaging Technologies*, vol. 26, no. 4, pp. 727–734, Dec. 2006.

[3] D. Hyman and M. Mehregany, "Contact physics of gold microcontacts for MEMS switches," *IEEE Transactions on Components and Packaging Technologies*, vol. 22, no. 3, pp. 357-364, Sept. 1999.

[4] M.B. Read, A.C. Weber, R. Martens, O. Yaglioglu, J.H. Lang, and A.H. Slocum "A highly repeatable MEMS based electrical contact test system," in *Proc. 10th EUSPEN International Conference*, Zürich, Switzerland, May 2008.

[5] M.B. Read, A.C. Weber, R. Martens, O. Yaglioglu, J.H. Lang, and A.H. Slocum, "A two-coupon system for the repeatable measurement of flat on flat microscale contact resistance," presented at *Proc. 24th International Conference on Electrical Contacts*, Saint Malo, France, June 2008.

[6] O. Yaglioglu, A.J. Hart, R. Martens, and A.H. Slocum, "Method of characterizing electrical contact properties of carbon nanotube coated surfaces," *Review of Scientific Instruments*, vol. 77, pp. 095105:1-3, Sept. 2006.

A MEMS-Relay for Make-Break Power-Switching Applications

A.C. Weber, J.H. Lang, A.H. Slocum

Sponsorship: NSF

We present a horizontal-displacement, electrostatically-actuated, MEMS relay for make-break power switching applications. The relay features {111}-plane silicon-etched electrical contacts. Experimental relays exhibit a minimum total on-state contact resistance of 130 mΩ, a response time of 750 µs, a theoretical electrical isolation in excess of 1 kV (tested to 450 V with available equipment), and a current-carrying capacity of 800 mA. The MEMS relay has been hot-switched in excess of 10^5 cycles without signs of performance degradation [1].

The relay, shown in Figure 1, is composed of four double-parallelogram flexures (1) that serve as bearings, eight pairs of engaging and disengaging electrostatic "zipper" actuators (2), one moving {111} contact (3), and a pair of static {111} contacts (4a, 4b). The {111}-plane contacts [2] offer several advantages over traditional MEMS-relay metal contacts: they provide large travel, on the order of 70 µm, which exceeds the 30 µm required to withstand contact erosion and the 10 µm required to prevent arcing while operating in air at atmospheric pressure; the oblique contact geometry introduces contact wipe, which is known to enhance the contact reliability; and the contact geometry allows for an enhanced metallization process that provides low on-state contact resistance. The relay is etched in (100) Si through a combination of KOH etching and DRIE using nested masks. After evaporation of a gold seed-layer on the contacts using a shadow mask, the silicon is bonded to a glass substrate. Next, the contacts are plated with a 10-µm-thick copper and a 2-µm-thick palladium-cobalt film. The device is released by dicing and packaged in a pin grid array for testing.

During testing, voltages and currents were continuously monitored as the relay cycled, and the instantaneous total contact resistance was computed, as shown in Figure 2. The load current and voltage were increased until the relay showed any signs of temporary contact-sticking during any actuation cycle throughout the test. The maximum hot-switched current achieved without any signs of contact sticking was 800 mA with a resistive load and 350 mA with a 1 mH inductive load. While operating at or below these currents, the MEMS relay was hot-switched in excess of 10^5 cycles without signs of performance degradation. While the device operated at higher currents than the threshold, the sticking phenomenon was found to occur sporadically and to be reversible. Once stuck, the contacts recovered after the relay was cycled with the load disconnected.

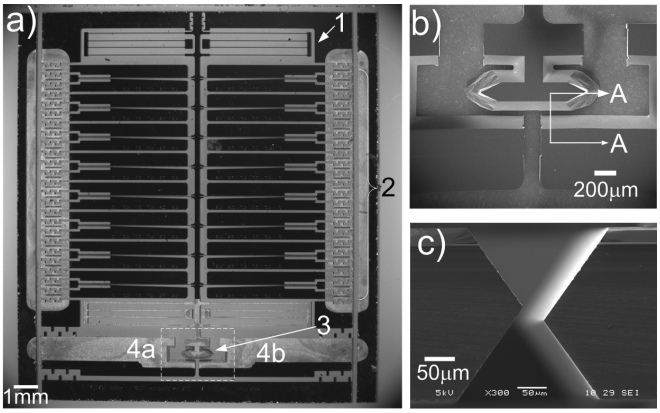

▲ Figure 1: Fabricated relay. (a) Die top view. (b) Contact detail, prior to metal deposition. (c) Contact cross-section A-A, as shown in Figure 1b, without the metal film.

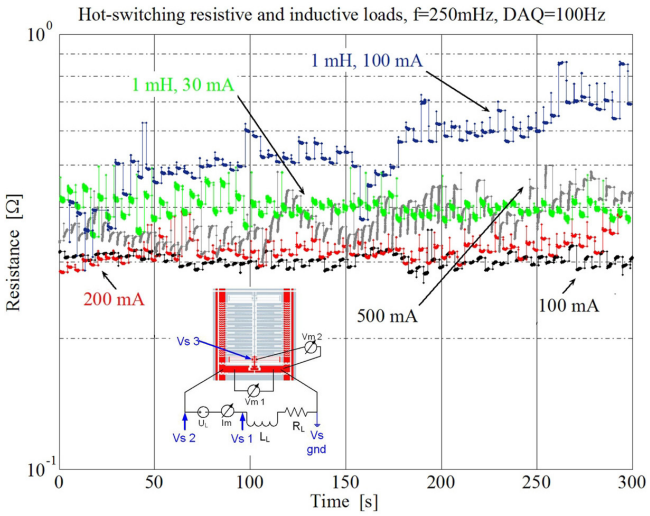

▲ Figure 2: Continuous sampling of total contact resistance during hot-switching. Inset: Experimental setup.

References

[1] A.C. Weber, J.H. Lang, and A.H. Slocum, "A MEMS-relay for Make-Break Power Switching Applications," to be presented at the *Solid State Sensor and Actuator Workshop*, Hilton Head, SC, June, 2008.

[2] A.C. Weber, J.H. Lang, and A.H. Slocum, "{111} Si Etched Planar Electrical Contacts for Power MEMS Relays," in *Proc. 53rd IEEE Holm Conference on Electrical Contacts*, Pittsburgh, PA, 2007, pp. 156-159.

Fabrication and Testing of a Fully-Integrated Multiwatt TurboGenerator

B.C. Yen, M. Allen, F.F. Ehrich, A.H. Epstein, F. Herrault, K.J. Hillman, L.C. Ho, S. Jacobson, J.H. Lang, H. Li, Z.S. Spakovszky, C.J. Teo, D. Veazie

Sponsorship: US Army Research Laboratory Collaborative Technology Alliance

There is a need for compact, high-performance power sources that can outperform the energy density of modern batteries for use in portable electronics, autonomous sensors, robotics, and other applications. The current research aims to produce a fully-integrated, synchronous permanent magnet microturbogenerator capable of generating 10 W DC output power using compressed air as its energy source. Past conference abstracts by Yen, et al. [1, 2] focused on the theoretical design as well as core fabrication procedures and techniques. Presently, all the silicon die fabrication is complete, and the magnetic components are being integrated onto the die in preparation for power generation testing.

While the magnetic integration is in progress, efforts are underway to separately test and qualify the gas-lubricated bearings that will support the magnetic rotor to very high speeds. To make the tests relevant, they are conducted on silicon dies similar to the final generator dies, with the only differences being the lack of surface windings and a laminated magnetic stator. Figure 1 shows a bearing rig die enclosed in an acrylic package, as well as the metal tubulations and o-rings used to bring nitrogen into the die.

Three sets of bearing rig tests are currently planned. A light rotor made purely of silicon and shown in Figure 2 will be used to assess the nominal imbalance, defined as the distance between the geometric and mass center of the rotor, introduced by the fabrication process. This rotor has approximately half the mass of the magnetic rotor, so a solder-filled rotor twice as heavy will be tested next to determine whether the bearings perform well with a massive rotor. After these two sets of experiments are complete, the magnetic rotor, which has permanent magnets and a soft magnetic back iron embedded in it, will be characterized. Because the silicon die can be easily opened along its eutectic interface [2], it is anticipated that the magnetic rotor can be removed from the die after testing and reused for the generator die.

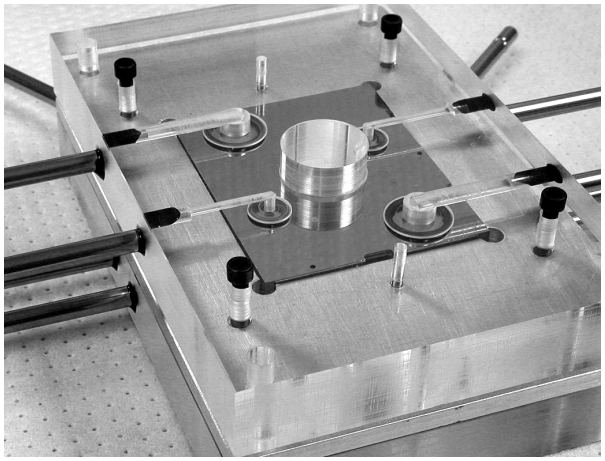

▲ Figure 1: A fully bonded heavy bearing rig silicon die enclosed in an acrylic package ready for testing. Nitrogen required for pressurizing the gas bearings and accelerating the rotor is fed in through an array of metal tubulations attached to the package using epoxy.

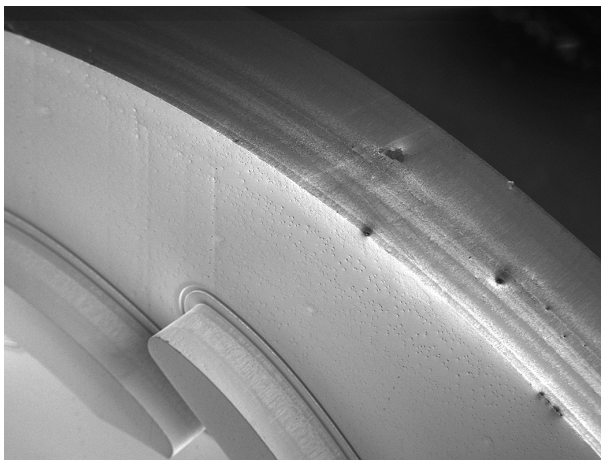

▲ Figure 2: Close-up SEM photo showing the journal bearing etch around the silicon rotor. A few recessed craters are visible, but the 900-µm sidewall is otherwise straight as expected. The rotor blades, created using a halo etch, are visible on the rotor surface.

References

[1] B.C. Yen, M. Allen, F.F. Ehrich, A.H. Epstein, F. Herrault, K.J. Hillman, L.C. Ho, S. Jacobson, J.H. Lang, H. Li, Z.S. Spakovszky, C.J. Teo, and D. Veazie, "An integrated multiwatt permanent magnet turbine generator," in *Proc. MTL Annual Research Conference,* January 2006.

[2] B.C. Yen, *et al.*, "Fabrication of a fully-integrated multiwatt µturbogenerator," in *Proc. MTL Annual Research Conference*, January 2007.

MEMS Micro-vacuum Pump for Portable Gas Analyzers

V. Sharma, M.A. Schmidt
Sponsorship: DARPA

There are many advantages to miniaturizing systems for chemical and biological analysis. Recent interest in this area has led to the creation of several research programs, including a Micro Gas Analyzer (MGA) project at MIT. The goal of this project is to develop an inexpensive, portable, real-time, and low-power approach for detecting chemical and biological agents. Elements entering the MGA are first ionized, then filtered by a quadrupole array, and sensed using an electrometer. A key component enabling the entire process is a MEMS vacuum pump, responsible for routing the gas through the MGA and increasing the mean free path of the ionized particles so that they can be accurately detected.

A great deal of research has been done over the past 30 years in the area of micro pumping devices [1, 2]. We are currently developing a displacement micro-vacuum pump that uses a piezoelectrically driven pumping chamber and a pair of piezoelectrically driven active-valves; the design is conceptually similar to the MEMS pump reported by Li et al. [3]. We have constructed an accurate compressible mass flow model for the air flow [4] as well as a nonlinear plate deformation model for the stresses experienced by the pump parts [5]. Using these models, we have defined a process flow and fabricated five generations of the MEMS vacuum pump over the past years and are currently working on improving the overall design.

Figure 1 shows a schematic of the pump. For ease in testing we have initially fabricated only layers 1-3 and have constructed a testing platform which, under full computer control, drives the pistons and monitors the mass flows and pressures at the ports of the device. The lessons learned from the first four generations of the pump have led to numerous improvements. Every step from the modeling, to the etching and bonding, to the testing has been modified and improved along the way. The most recent fifth generation pump test data appears in Figure 2. Figure 2a shows the measurements of the vacuum being generated in an external volume (5.6cm^3) by the micropump operating at 2Hz. The pump was able to reduce the external volume pressure by 163 Torr. Figure 2b shows the micropump-generated flow rate as a function of pumping frequency (driven in a 6-stage cycle by a controlling microprocessor to move the gas from the input to the output). The performance of this pump compares very well with that of other similar scaled micropumps in the literature. Next, we plan to fabricate and test an improved overall design and develop a final set of models to fabricate any future micropumps to the desired specifications.

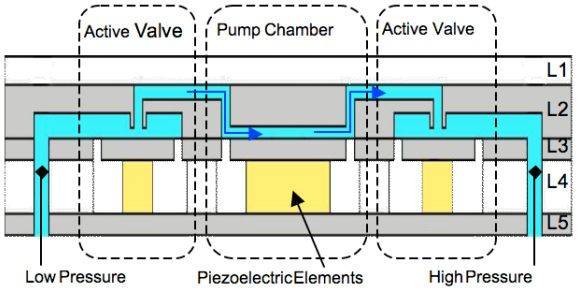

▲ Figure 1: The MEMS vacuum pump schematic. Layers 1 and 4 are glass, layers 2 and 5 forming the chambers, channels, and support are silicon, and layer 3 forming the pistons and tethers is SOI silicon

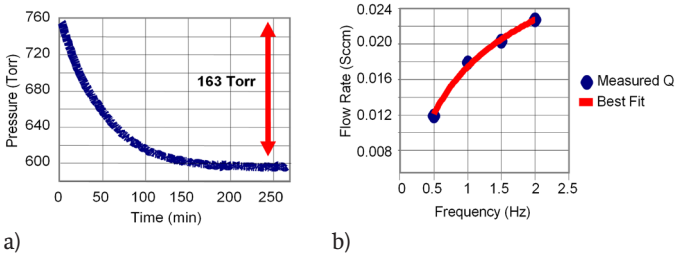

▲ Figure 2: a) The vacuum generation performance of the micropump. b) The pump-generated flow rate as a function of the pumping frequency.

References

[1] D.J. Laser and J.G. Santiago, "A review of micropumps," *Journal of Micromechanics and Microengineering*, vol. 14, no. 6, pp. 35-64, 2004.

[2] P. Woias, "Micropumps--past, progress and future prospects," *Sensors and Actuators B: Chemical*, vol. 105, no. 1, pp. 28-38, 2005.

[3] H.Q. Li, D.C. Roberts, J.L. Steyn, K.T. Turner, J.A. Carretero, O. Yaglioglu, Y.-H. Su, L. Saggere, N.W. Hagood, S.M. Spearing, M.A. Schmidt, R. Mlcak, and K. Breuer, "A high-frequency, high flow rate, piezoelectrically driven MEMS micro-pump," *IEEE Solid State Sensors and Actuators Workshop*, Hilton Head SC, June 2000.

[4] A.K. Henning, "Improved gas flow model for micro-valves," *Proceedings of Transducers 2003*, Boston, MA, pp. 1550-1553, June 2003.

[5] D.C. Roberts, O. Yaglioglu, J.Carretero, Y.-H Su, L. Saggere, and N.W. Hagood, "Modeling, design, and simulation of a piezoelectrically driven microvalve for high pressure, high frequency applications," in *Proc. SPIE–The International Society for Optical Engineering, Smart Structures and Materials 2001–Smart Structures and Integrated Systems*, Newport Beach, CA, Mar. 2001, pp. 366-380.

Batch-fabricated Linear Quadrupole Mass Filters

K. Cheung, L.F. Velasquez-Garcia, A.I. Akinwande
Sponsorship: DARPA

In recent years, there has been a desire to scale down linear quadrupoles. The key advantages of this miniaturization are the portability it enables and the reduction of pump power needed due to the relaxation on operational pressure. Attempts at making microelectromechanical systems-based linear quadrupoles met with varying degrees of success [1-3]. Producing these devices involved some combination of precision machining or microfabrication and downstream assembly. For miniature quadrupole mass filters to be mass-produced cheaply and efficiently, manual assembly should be removed from the process.

A purely microfabricated quadrupole mass filter consisting of a planar design and a rectangular electrode geometry has been made. Rectangular rods were utilized since they are most amenably shaped for planar microfabrication. This deviation from the conventional round rod geometry required optimization and analysis. After we minimized unwanted effects through various simulations, we proposed a design (Figure 1), conceived a process flow, and fabricated the Micro-Square Electrode Quadrupole Mass Filter (MuSE-QMF) (Figure 2). The process requires the bonding of five silicon wafers and the use of deep reactive ion etching to pattern the features. It is a relatively simple process, furthering the case for mass-production of these devices.

This non-conventional design will introduce non-linear resonances that manifest as peak splitting in the mass spectrum. Reported work involving linear quadrupoles operated in the second stability region shows improved peak shape without these splits [3]. It is believed that operating this device in the second stability region will provide a means to overcome the nonlinear resonances introduced by the square electrode geometry. Successful implementation of this device will lead into arrayed configurations for parallel analysis and aligned quadrupoles operated in tandem for enhanced resolution.

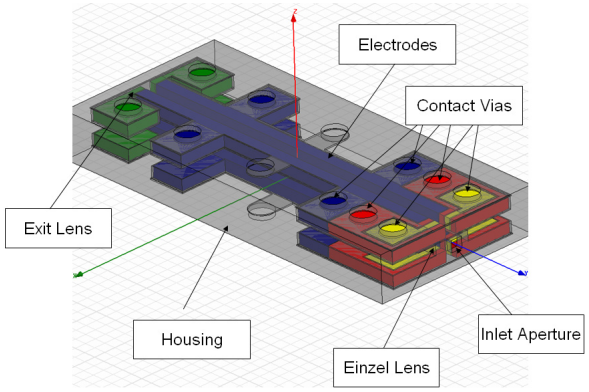

▲ Figure 1: Schematic of proposed device.

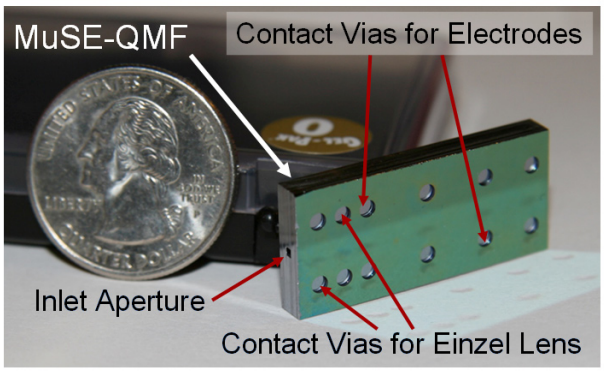

▲ Figure 2: Fabricated device.

References

[1] M. Gear, R.R.A. Syms, S. Wright, and A.S. Holmes, "Monolithic MEMS quadrupole mass spectrometers by deep silicon etching," *Journal of Microelectromechanical Systems*, vol. 14, no. 5, pp. 1156-1166, Oct. 2005.

[2] J.J Tunstall, S. Taylor, R.R.A. Syms, T. Tate, and M.M. Ahmad, "Silicon micromachined mass filter for a low-power, low-cost quadrupole mass spectrometer," in *Proc. IEEE Eleventh Annual International Workshop on Micro Electro Mechanical Systems*, Heidelberg, Germany 1998, pp. 438-442.

[3] L.F. Velazquez-Garcia, K. Cheung, and A.I. Akinwande, "An application of 3D MEMS packaging: Out-of-plane quadrupole mass filters," *Journal of Microelectromechanical Systems*, submitted for publication.

MEMS Ejector Pumps Driven by MEMS Steam Generators

F. Eid, L.F. Velasquez-Garcia, C. Livermore
Sponsorship: DARPA, MDA, AFRL

Vacuum pumping of gases at the MEMS scale is an ongoing challenge; MEMS pumps typically have pressures far above and pumping rates far below those of their macroscale counterparts. To meet this challenge, we are creating high-mass-flow-rate MEMS steam-ejector pumps that are driven by MEMS-based steam generators. Ejector pumps scale favorably to the MEMS scale because the entrainment of the flow to be pumped by the driving fluid takes place over a much shorter distance in a narrow, millimeter-scale channel than in a wide macroscale channel [1]. However, delivering driving fluid from a compact source remains a significant challenge. Our solution to this challenge is MEMS steam generators that decompose hydrogen peroxide with a liquid catalyst in order to produce the ejectors' driving fluid. The creation of MEMS steam generators enables the creation of systems of high-performance MEMS pumps.

One important objective of this work is the design, fabrication, and demonstration of the MEMS steam generator to drive the pumps. The generator decomposes hydrogen peroxide using a homogeneous (liquid) catalyst to produce steam, which is then accelerated through a nozzle to the high velocities required for effective pumping. Hydrogen peroxide is selected for its availability and environmental friendliness. The use of a liquid catalyst eliminates common problems of catalyst poisoning and aging, and the system is sized and designed to minimize thermal losses and enable complete decomposition of the peroxide.

Our work to date has primarily focused on the design and modeling of the steam generator and its interface with the pumps. Conceptually, the MEMS steam generator consists of a microscale mixer, a reactor, and a converging-diverging nozzle to accelerate the exiting flow, as shown in Figure 1. One or more steam generators would be coupled to a MEMS ejector as shown in Figure 2. Liquid H_2O_2 is mixed with the catalyst in the generator's "engulfment" mixer [2] and then injected into the reactor, where the peroxide decomposes into steam and oxygen gas. The mixing timescale is much less than the reaction timescale, so that the reaction and vaporization take place in uniformly-mixed fluid inside the reaction chamber. The gaseous products are then accelerated to supersonic velocities through the converging-diverging nozzle. Models predict adequate thermal management and high performance for the generator-driven MEMS pumping system. The research now focuses on the realization and experimental demonstration of the MEMS steam generator to drive the MEMS pumping system.

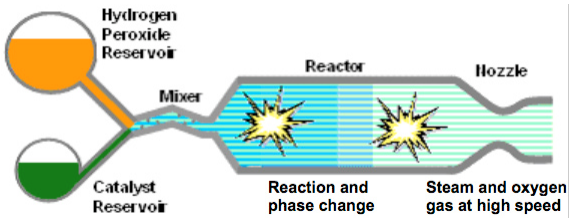

▲ Figure 1: Schematic diagram of a hydrogen peroxide-based MEMS steam generator, showing the mixer, reactor, and nozzle

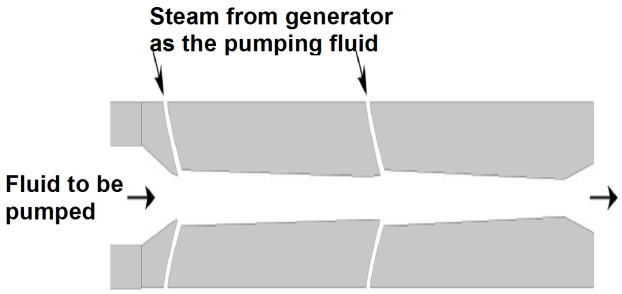

▲ Figure 2: Integration of MEMS steam generators with an ejector unit

References

[1] B.A. Wilhite, C. Livermore, Y. Gong, A.H. Epstein, and K.F. Jensen, "Design of a MEMS-based microchemical oxygen-iodine laser (mCOIL) system," *IEEE Journal of Quantum Electronics*, vol. 40, pp. 1041-1055, Aug. 2004.

[2] N. Kockmann and P. Woias, "Flow regimes and mass transfer characteristics in static micromixers," *Proc. of SPIE*, vol. 4982, pp. 319, 2003.

Micro-Reaction Technology for Energy Conversion

B. Blackwell, K. Deshpande, J. Keybl, C. Marton, M.A. Schmidt, K.F.Jensen

The development of portable-power systems remains an important goal, with applications ranging from the automobile industry to the portable electronics industry. The focus of this work is to develop microreaction technology that converts fuels – such as light hydrocarbons and their alcohols-- to hydrogen for use in solid oxide fuel cells or directly into electricity. Developing high-efficiency devices requires addressing difficulties in high temperature operation: specifically, thermal management, material integration, and improved packaging techniques. In addition, recent work has included efforts to harness energy rejected to the environment as heat.

The microreactor designed for combustion has been improved, resulting in longer residence times within the reactor. This longer residence time ensures full combustion of propane fuel over a platinum catalyst. The channels within the reactor are etched using wet potassium hydroxide, which is the most economical etch technique available. The reactor remains suspended via thin-walled glass tubes, reducing conductive heat losses and allowing the reactor to operate at high temperatures. The tubes are brazed to the microreactor using a thermally-matched glass braze technique that was developed in-house. The coupling of two reactors has allowed for combustion to occur in one and ammonia cracking in the other, resulting in autothermal hydrogen generation.

A combined reforming/separation device has been developed and demonstrated. Specifically, the hydrogen generation unit combines a 200-nm-thick palladium-silver film with a methanol reforming catalyst, e.g., LaNiCoO3. The catalytic combustion unit employs a platinum catalyst. Both units are formed in a silicon wafer by bulk silicon micromachining techniques. The energy generated in the combustion unit is efficiently transferred to the hydrogen production unit in the thermal conduction of silicon support. With a modified brazing technique, the reactor is thermally insulated from its environment. The system has been demonstrated to purify hydrogen at elevated pressures (up to 2 atm). Joint combustion/purification of the system has also been demonstrated, in which combustion and reforming occur simultaneously with the purification of the resulting hydrogen.

Recent work has also included efforts to harness waste heat in the form of electrical energy. Thermophotovolatics (TPV) cells are being integrated to harness radiation energy. Work is also ongoing to integrate thermoelectric (TE) devices to harness waste heat through intimate contact of the TE device with the microreactor.

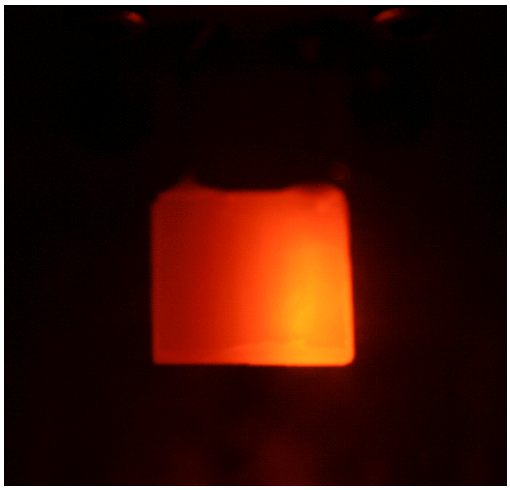

▲ Figure 1: Autothermal, steady-state combustion of 9.5-sccm butane over 2.5 mg of 1wt% Pt on Al_2O_3. The temperature of the hotspot was 830°C.

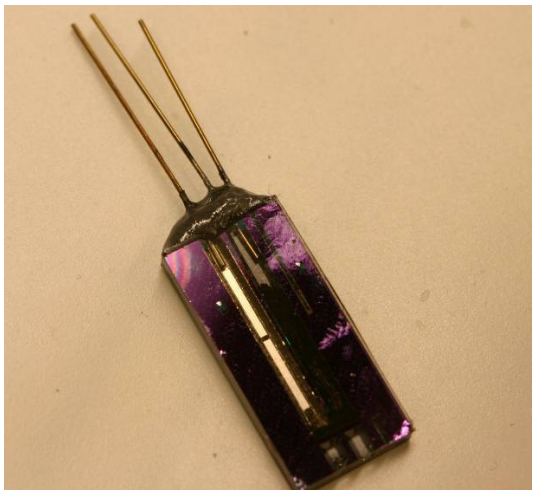

▲ Figure 2: Combined reforming/separation device. The three fluidic connections are for reactant gases, combusted gases, and purified hydrogen.

Microfabricated Thin-film Electrolytes and Electrodes for Solid Oxide Fuel-cell Electrodes

S.J. Litzelman, W.C. Jung, K. Sahner, H.L. Tuller
Sponsorship: National Science Foundation, DMR-0243993

Micro-solid oxide fuel cells (SOFCs) are currently under intense investigation for portable power applications, such as notebook computers and mobile phones [1, 2]. While thin-film nanostructured solid electrolytes result in lower cell losses due to ohmic resistance, grain boundaries may serve as fast diffusion pathways for cations, resulting in poorer long-term stability. The effects of grain boundary chemistry and interdiffusion on ionic transport have yet to be systematically investigated.

To explore the relationship between performance and stability, CeO_2 thin films were grown by pulsed laser deposition (PLD), as shown in a transmission electron micrograph (TEM) in Figure 1 [3]. Thin diffusion sources of NiO and Gd_2O_3 were deposited, and samples were annealed in the temperature range of 700-800 °C to in-diffuse the Ni cations heterogeneously along the grain boundaries. Confirmation of diffusion along the grain boundaries was achieved via time-of-flight secondary ion mass spectrometry (ToF-SIMS). After modification, the diffusion source was removed by a wet etching process, and Pt microelectrodes were prepared via a photolithographic lift-off process. The electrical conductivity was measured by impedance spectroscopy and two-point DC techniques, and it decreased 10x following grain boundary in-diffusion. These results are being modeled by examination of changes in charge-carrier profiles induced by the in-diffusion in the space charge region adjacent to the boundary.

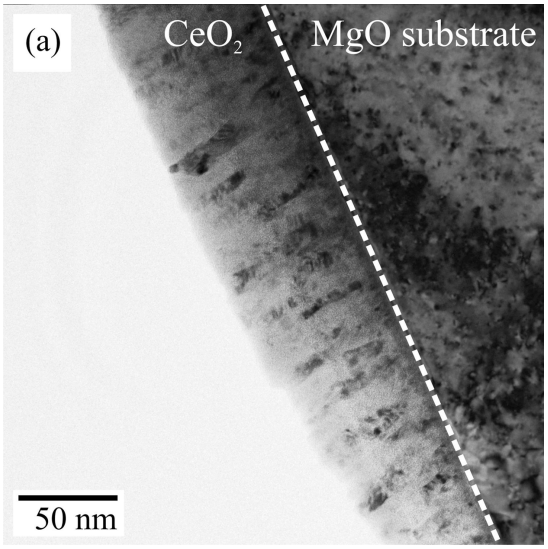

▲ Figure 1: Cross-sectional TEM image of CeO_2, showing parallel columnar grain boundaries and grain sizes of approximately 25-40 nm.

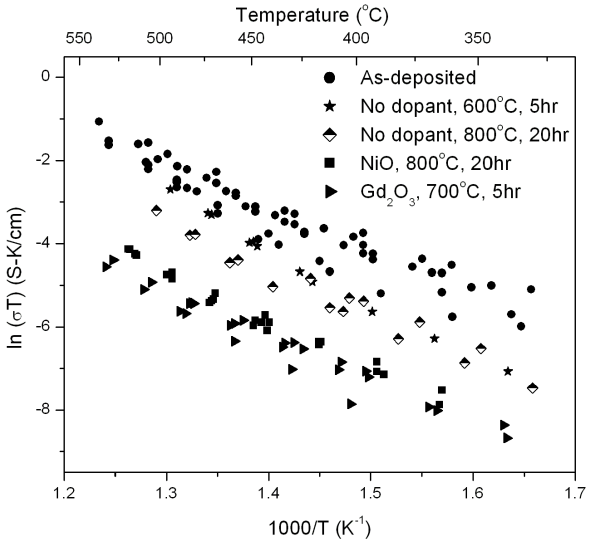

▲ Figure 2: Electrical conductivity of as-deposited and modified CeO_2, which decreases upon in-diffusion but without any clear change in the thermal activation energy.

References

[1] C.D. Baertsch, K.F. Jensen, J.L. Hertz, H.L. Tuller, S.T. Vengallatore, S.M. Spearing, and M.A. Schmidt, "Fabrication and structural characterization of self-supporting electrolyte membranes for a micro solid-oxide fuel cell," *Journal of Materials Research*, vol. 19, no. 9, pp. 2604-2615, Sept. 2004.

[2] D. Nikbin, "Micro SOFCs: Why small is beautiful," *The Fuel Cell Review*, vol. 3, no. 2, pp. 21-24, Apr. 2006.

[3] S.J. Litzelman, R.A. De Souza, B. Butz, H.L. Tuller, M. Martin, and D. Gerthsen, "Heterogeneously doped nanocrystalline ceria films by grain boundary diffusion: Impact on transport properties," *Journal of Electroceramics*, DOI: 10.1007/s10832-008-9445-y, 2008.

Chemical Synthesis with Online Optimization in Microreactor Systems

J.P. McMullen, N. Zaborenko, H.R. Sahoo, K.F. Jensen
Sponsorship: MIT Microreactor Consortium

Microreactors are powerful instruments for scanning and optimizing chemical reactions due to their enhanced heat and mass transfer, reduced reaction volume, and the ability to run several experiments in parallel. Applying fabrication principles that have been developed for integrated circuits, such as lithography, deep reactive ion etching (DRIE), oxidation, anodic bonding, and electron beam metal deposition, microreactors can be designed to accommodate a comprehensive set of chemistries. In addition to the study of chemical reactions under these enhanced conditions, such as high temperature and high pressure, use of other process components such as mixers, heat exchangers, and phase separators can be incorporated on a chip to provide a multifunctional microreactor (Figure 1). Previous work in our group has focused on exploiting these benefits in order to determine optimal reaction conditions (e.g., temperature, pH, etc.) quickly, as well as to accurately evaluate the reaction kinetics for chemical syntheses related to pharmaceutical and fine chemistry sectors.[1, 2]

Microreactors can also be integrated with physical sensors to provide online measurement of process variables. Pressure sensors can be used to determine liquid flow rates, and temperature sensors are readily integrated by using thin film resistors or by incorporating a thin thermocouple. The progress of the chemical reaction can be monitored on-chip through UV/Vis, infrared, or Raman spectroscopy. Incorporating these measurements with traditional feedback control and optimization algorithms enables the optimization procedure to be completely automated. Such an 'intelligent' microreactor system was applied experimentally for a multi-step reaction, the oxidation of benzyl alcohol by chromium trioxide to benzaldehyde with further oxidation to benzoic acid, to determine the conditions that maximize the yield of the intermediate, benzaldehyde. In a multi-parameter (e.g., reaction temperature and reagent flow rates) optimization approach, the system performed approximately 30 experiments in a completely automated fashion to determine the optimal yield of 82 – 84% (Figure 2).

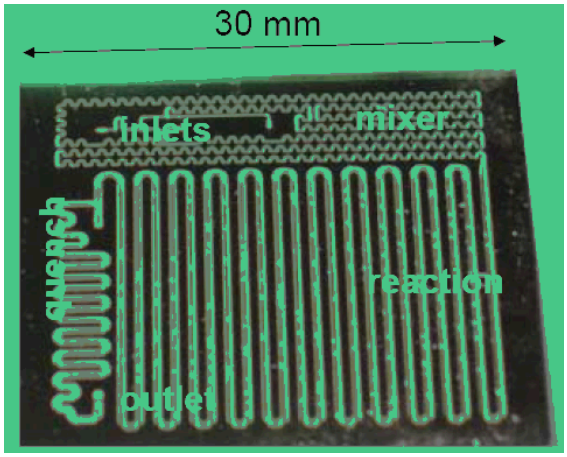

▲ Figure 1: Microreactor is integrated with mixer and quench zone for accurate optimization and kinetic studies. Mixing channels are 200 x 400 µm and reaction channels are 400 x 400 µm in cross section.

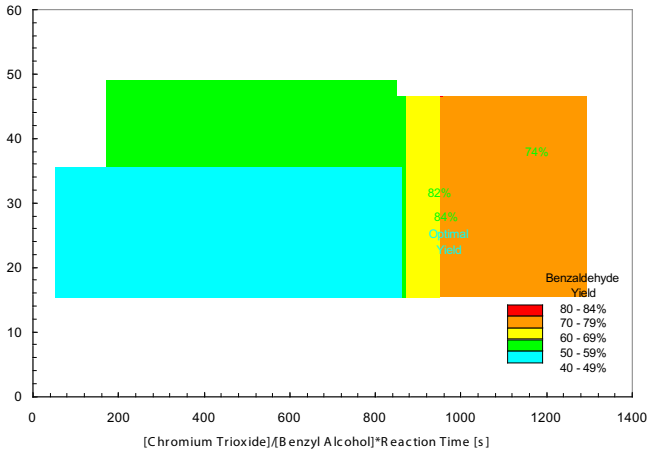

▲ Figure 2: Benzaldehyde yield for experimental conditions automatically performed by multiple parameter optimization platform. Contours of benzaldehyde yield are shown for different reaction temperatures and for a lumped variable defined by the product of the ratio of the initial concentrations of chromium trioxide to benzyl alcohol and reaction time for 2-D representation of data collected over a 4-parameter (4D) optimization.

References

[1] E.R Murphy, J.R. Martinelli, N. Zaborenko, S.L. Buchwald, and K.F. Jensen, "Accelerating reactions with microreactors at elevated temperatures and pressures: Profiling aminocarbonylation reaction," *Angewandte Chemie, International Edition*, vol. 46, pp. 1734-1737, 2006 .

[2] D.M. Ratner, E.R. Murphy, M. Jhunjhunwala, D.A. Snyder, K.F. Jensen, and P.H. Seeberger, "Microreactor-based reaction optimization in organic chemistry – Glycosylation as a challenge," *Chemical Communications*, vol. 5, no. 5, pp. 578-580, 2005.

Novel Synthesis of Polymeric Nanoparticles for Drug Delivery Applications Using Microfluidic Rapid Mixing

P. Valencia, F. Gu, P. Basto, L. Zhang, C. Cannizzaro, R.S. Langer, O. Farokhzad, R. Karnik
Sponsorship: National Cancer Institute

The development of smart targeted nanoparticles (NPs) that can deliver drugs at a sustained rate directly to specific cells may provide better efficacy and lower toxicity for treating many diseases. For these applications, control of the NP properties such as size and polydispersity is of utmost importance for the particles' end therapeutic effects. Here we report the use of rapid microfluidic mixing using hydrodynamic flow focusing to control self-assembly of polymeric NPs. Self-assembly occurs through nanoprecipitation, a process that involves dilution of a block copolymer from a solvent to an anti-solvent resulting in the precipitation of NPs [1]. We demonstrated that through the rapid mixing of precursors with anti-solvent (i.e., water), the particle size could be tuned and more homogeneous NPs could be synthesized. This work is the first implementation of nanoprecipitation on a microfluidic platform.

The PDMS microfluidic devices were used to synthesize PLGA-PEG NPs by mixing PLGA7400-PEG3500 in acetonitrile (50 mg/ml) with water (anti-solvent). Hydrodynamic focusing was achieved by controlling flow rates with syringe pumps. Figure 1 shows the polymer stream being focused by two water streams as well as a TEM image of the resulting NPs. Figure 2 shows the change in PLGA-PEG particle size as mixing time is varied. Mixing time (~ 1-10 ms) can be tuned by changing the flow ratio of the solvent to anti-solvent. These results agree with the idea that self-assembly of block copolymers into NPs by nanoprecipitation yields smaller particles as mixing time is decreased [2].

This work demonstrates that microfluidic synthesis of polymeric nanoparticles with rapid mixing allows for tuning of NP size and distribution through control of flow rates. These results lay the foundations of a microfluidic platform for controlled synthesis of NPs that may result in improved performance in drug delivery applications.

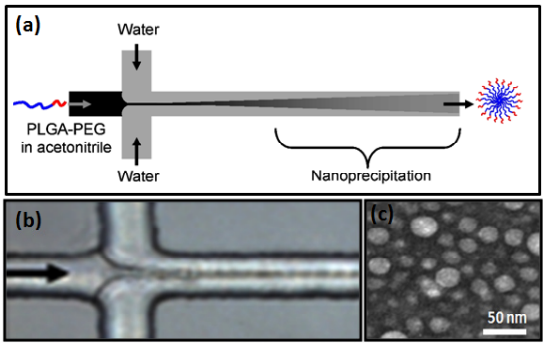

▲ Figure 1: (a) Schematic of synthesis of nanoparticles by nanoprecipitation using hydrodynamic flow focusing. (b) Micrograph of the 20x60-μm device in operation. Flow rates of the polymer and water streams are 2 μl/min and 20 μl/min (total), respectively. (c) A TEM image of nanoparticles synthesized

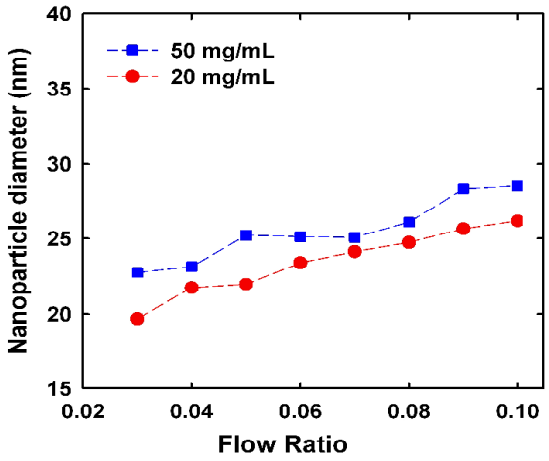

▲ Figure 2. Effect of flow ratio on nanoparticle size. Increasing the polymer stream flow rate and keeping the water stream flow rate constant (20 μl/min) results in larger nanoparticles. Mixing time increases as the polymer stream flow rate increases.

References

[1] J. Cheng, B.A. Teply, I. Sherifi, J. Sung, G. Luther, F. Gu, E. Levy-Nissenbaum, A.F. Radovic-Moreno, R. Langer, and O.C. Farokhazad, "Formulation of functionalized PLGA-PEG nanoparticles for in vivo targeted drug delivery," *Biomaterials*, vol. 28, pp. 869-873, Oct. 2006.

[2] B.K. Johnson and R.K. Prud'homme, "Mechanism for rapid self-assembly of block copolymer nanoparticles," *Physical Review Letters*, vol. 91, no. 11, pp. 118302: 1-4, Sept. 2003.

Design, Fabrication, and Testing of Multilayered, Microfabricated Solid Oxide Fuel Cells (SOFCs)

N. Yamamoto, D. Quinn, P. Capozzoli, N. Wicks, B.L. Wardle, S.M. Spearing (in coll. with B.A. Wilhite, J. Hertz, J. Cui, K.F. Jensen, H.L. Tuller, M.A. Schmidt)

Sponsorship: ARO

Microfabricated solid oxide fuel cells were investigated for portable power applications requiring high energy densities [1]. The thickness of the electrolyte, the travel length of oxygen ions, was reduced down to ~150nm. The tri-layers (yttria-stabilized zirconia (YSZ) as an electrolyte and platinum-YSZ cermet as cathode/anode) were sputter-deposited on a silicon wafer, and then they were released as square plates by KOH-etching the silicon through patterned silicon nitride masks on the back side. High intrinsic and extrinsic (thermal) stresses due to fabrication and operation (25-600°C) [2], respectively, require careful thermomechanically stable design of μSOFCs.

First, material properties of the ultra-thin YSZ were characterized experimentally and found to be significantly different than those of bulk YSZ [3]. Second, based on the obtained properties, maximum stresses in the plates at 625°C were analyzed using non-linear von Karman plate theory [4]. The stresses showed three regions with sidelength variation: un-buckled regime, buckled regime with high stresses, and post-buckling regime with lower stresses (see Figure 1). The μSOFCs were fabricated in the post-buckling regimes with ~80-~180-μm sidelength and total ~450-nm thickness. With the plates buckled as shown in Figure 2, the μSOFCs produced power output of 0.008mW/cm, lower than the expected power from their electrochemical test. Given the high-performance predicted for the underlying nano-structured ultra-thin electrolyte, anode, and cathode layers, additional studies are needed to improve specimens and test setup and to assess μSOFCs' long-term operational stability.

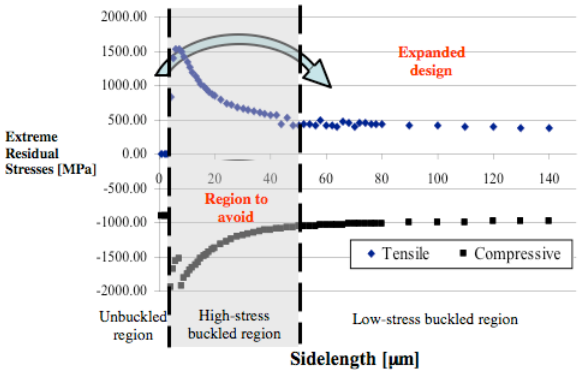

▲ Figure 1: Maximum stress evolution with sidelength of YSZ square membranes with ~450nm thickness cycled to 600°C.

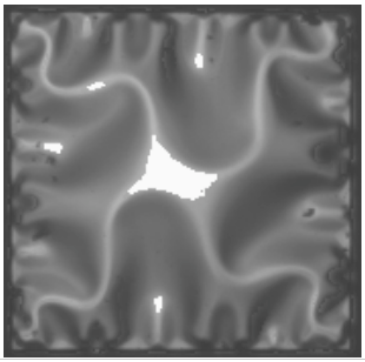

▲ Figure 2: Top-view of highly buckled, but unfailed, square membrane.

References

[1] C.D. Baertsch, et al., "Fabrication and structural characterization of self-supporting electrolyte membranes for a μSOFC," *Journal of Materials Research*, vol. 19, pp. 2604-2615, 2004.

[2] D.J. Quinn, M.S. Spearing, and B.L. Wardle, "Residual stress and microstructural evolution in thin film materials for a micro solid oxide fuel cell (SOFC)," *Materials Research Society Meeting*, Boston, MA, Nov. 2004.

[3] N. Yamamoto, "Thermomechanical properties and performance of microfabricated solid oxide fuel cell (μSOFC) structures," Masters' thesis, Massachusetts Institute of Technology, Cambridge, MA, 2006.

[4] N. Yamamoto, N. Wicks, and B.L. Wardle, "Twice-buckled cermet composite laminate under equibiaxial compression," in *Proc. 48th AIAA/ASME/ASCE/AHS/ASC Structures, Structural Dynamics, and Materials Conference*, Honolulu, HI, Apr. 2007.

Microscale Singlet Oxygen Generator for MEMS-based COIL Lasers

T. Hill, L.F. Velásquez-García, A.H. Epstein, K.F. Jensen, C. Livermore
Sponsorship: DARPA, MDA, AFRL

Conventional chemical oxygen iodine lasers (COIL) offer several important advantages for materials processing, including short wavelength (1.3 μm) and high power. However, COIL lasers typically employ large hardware and use reactants relatively inefficiently. This project is creating an alternative approach called microCOIL. In microCOIL, most conventional components are replaced by a set of silicon MEMS devices that offer smaller hardware and improved performance. A complete microCOIL system includes microchemical reactors, microscale supersonic nozzles, and micropumps. System models incorporating all of these elements predict significant performance advantages in the microCOIL approach [1].

Initial work is focused on the design, microfabrication, and demonstration of a chip-scale singlet oxygen generator (SOG), a microchemical reactor that generates singlet delta oxygen gas to power the laser. Given the extensive experience with micro-chemical reactors over the last decade [2], it is not surprising that a microSOG would offer a significant performance gain over large-scale systems. The gain stems from basic physical scaling; surface-to-volume ratio increases as the size scale is reduced, which enables improved mixing and heat transfer. The SOG chip being demonstrated in this project employs an array of microstructured packed-bed reaction channels interspersed with microscale cooling channels for efficient heat removal [3]. To date the device has produced oxygen concentrations of 10^{17} cm^{-3}, yields approaching 80%, and molar flowrates in excess of $600x10^{-4}$ moles/L/sec [4]. The yield and molar flowrates indicate a significant improvement over the macroscale SOG designs.

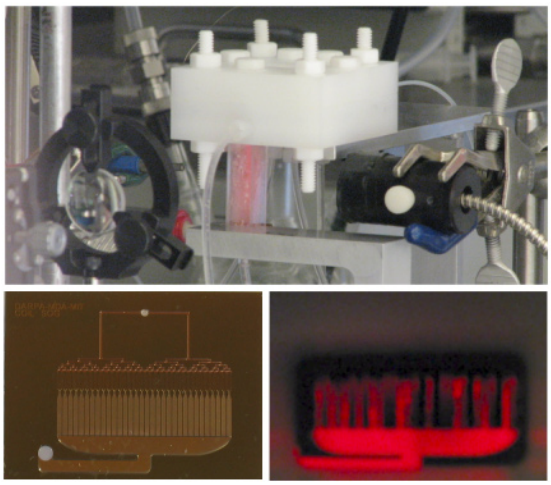

▲ Figure 1: A) View of chip surface showing glow resulting from singlet-oxygen production. B) View of packaging and optics surrounding microSOG. C) Photograph of microSOG.

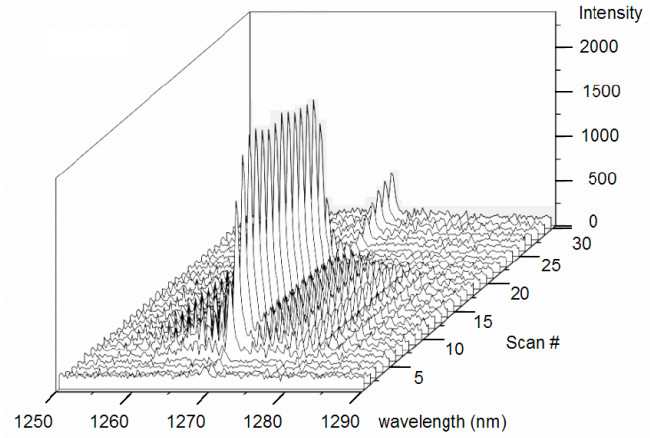

▲ Figure 2: The IR spectra measured at the μSOG gas outlet versus time. The peak at 1268 nm indicates the spontaneous decay of singlet oxygen into its triplet state.

References

[1] B.A. Wilhite, C. Livermore, Y. Gong, A.H. Epstein, and K.F. Jensen, "Design of a MEMS-based microchemical oxygen-iodine laser (mCOIL) system," *IEEE Journal of Quantum Electronics*, vol. 40, pp. 1041-1055, Aug. 2004.

[2] M.W. Losey, M.A. Schmidt, and K.F. Jensen, "Microfabricated multiphase packed-bed reactors: Characterization of mass transfer and reactions," *Ind. Eng. Chem. Res.*, vol. 40, pp. 2555-2562, June 2001.

[3] L.F. Velásquez-García, T.F. Hill, B.A. Wilhite, K.F. Jensen, A.H. Epstein, and C. Livermore, "A MEMS singlet oxygen generator – Part I: Device fabrication and proof of concept demonstration," submitted to *IEEE Journal of Microelectromechanical Systems*, 2007.

[4] T.F. Hill, L.F. Velásquez-García, B.A. Wilhite, W.T. Rawlins, S. Lee, S.J. Davis, K.F. Jensen, A.H. Epstein, and C. Livermore, "A MEMS singlet oxygen generator- Part II: Experimental exploration of the performance space," submitted to *IEEE Journal of Microelectromechanical Systems*, 2007.

Templated Assembly by Selective Removal

G. Agarwal, F. Eid, C. Livermore

Sponsorship: NSF Career Award, Pappalardo Graduate Fellowship

Templated assembly by selective removal (TASR) is an effective technique for site-selective multi-component assembly at the nano- and micro-scales. In this project, the TASR approach has been created, demonstrated and quantitatively modeled; work to expand the technology and exhibit practical applications is now underway. The TASR approach offers great promise for assembling arbitrary (not necessarily periodic) systems of multiple different types of nanoscale components, such as electronics and biological or chemical sensing devices. It also offers a path to a new kind of shape- and size-selective chromatography.

TASR employs a combination of chemistry, surface topography and controllable ultrasonically-induced fluid forces to assemble diverse sets of objects selectively from fluid into designated sites on a 2D surface [1]. Figure 1 shows a schematic layout of the process set-up. The components and the substrate, after undergoing chemical surface modification by a coating of an adhesion promoter, are placed in a fluid environment for the assembly process and megahertz frequency ultrasound is applied to the fluidic bath. Competition between the chemical adhesive effects and fluidic removal forces takes place in which adhesive forces emerge as stronger for components in a well-matched site. The selectivity is based on the degree to which the component to be assembled matches the shape and dimensions of the surface topography at that location. Figure 2 is an optical micrograph showing the successful assembly of 600 nm and 2 mm diameter silica microspheres using TASR. Experiments are now being conducted to extend the technique to a variety of different materials such as biological cells, polymers and nanorods which vary markedly not only in their physical configuration and properties but also in their chemical interaction with the substrate onto which they are to be assembled.

Thus, TASR can be used as a low-cost nanofabrication method with the ability to create complex, arbitrary patterns. We are also investigating the extension of TASR to a shape- and size-sensitive separation mechanism enabling the fabrication of a filtering device with chromatography applications. Present work focuses on the extension of TASR to smaller size scales, a diverse set of component shapes and materials, and improved template fabrication techniques with the goal of demonstrating numerous practical applications enabled by this approach.

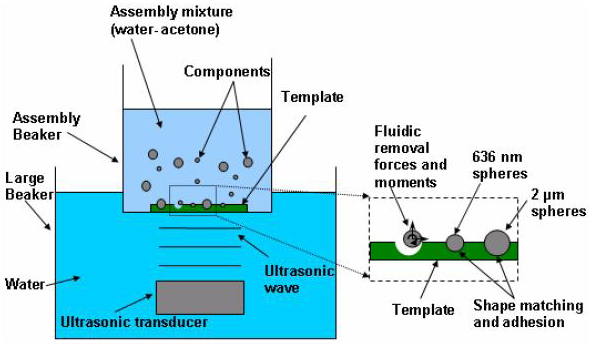

▲ Figure 1: Concept schematic of Templated Assembly by Selective Removal (TASR).

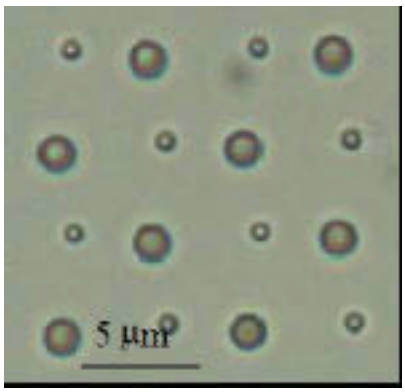

▲ Figure 2: Silicon microspheres self assembled on a templated silicon-silicon dioxide substrate.

References

[1] S. Jung and C. Livermore, "Achieving selective assembly with template topography and ultrasonically induced fluid forces," *Nanoletters*, vol. 5, no. 11, pp. 2188-2194, Nov. 2005.

Transplanting Assembly of Individual Carbon Nanotubes to MEMS Devices

S. Kim, H.W. Lee, S.-G. Kim

Sponsorship: Intelligent Microsystems Center

The biggest challenge in integrating nanostructures to MEMS is how to handle and assemble individual nanostructures. We demonstrate a novel assembly method for fabricating CNT-tipped atomic force microscopy (AFM) probes at a high rate and controllable quality via integrating the CNT into MEMS. Its key idea is to grow individual CNTs on a separate substrate and to transplant a well-grown CNT to the target location on a MEMS cantilever (Figure 1). This assembly concept transforms the scale of CNT assembly from nano-scale to micro-scale, which enables even manual assemble of individual CNTs in a deterministic way.

An array of CNTs is grown from the nickel (Ni) nano-dots defined on Si substrates using electron-beam lithography followed by metal deposition and lift-off processes. Each CNT is embedded into a MEMS scale polymer block that serves as a CNT carrier. A double polymeric layer encapsulation process with SU8 (top) and PMGI (bottom) enables an easy release from the substrate and a deterministic length control of the CNT tip. Manual assembly of a polymer block to the end of a tipless AFM cantilever forms a CNT-tipped AFM probe. No laborious weeding, trimming, or welding process was required, and the transplanting assembly technique enables reliable assembly of CNT tips on various AFM cantilevers. The exposed CNT tip normal to the sample surface is 1.5 μm long, which corresponds to the thickness of the bottom layer (Figure 2, top).

The scanning results over a grating with 3-μm pitch and 100-nm-deep vertical trenches shows that our CNT-tipped AFM probe scans the vertical trenches close to their vertical walls. The scanning on a biological sample (filament actins) demonstrates the potential of a CNT-tipped AFM probe for use with soft biological samples (Figure 2, bottom). This technology makes readily feasible massive parallel assembly, which will be pursued in the future.

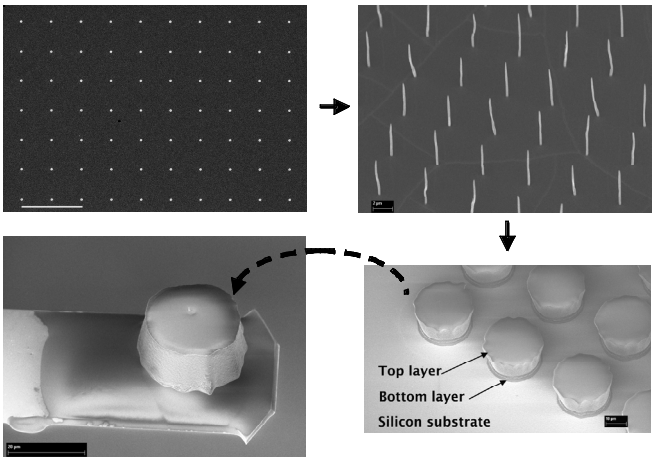

▲ Figure 1: Transplanting assembly procedure in fabricating CNT-tipped AFM probes. A single CNT strand is grown and transplanted at the end of an AFM cantilever in a deterministic and repeatable manner.

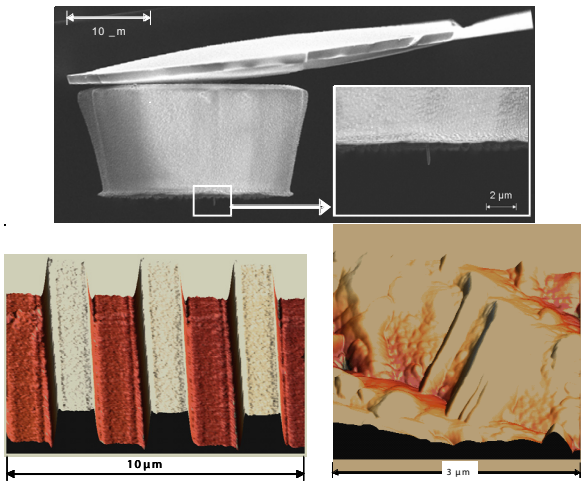

▲ Figure 2: An AFM probe with a single CNT tip normal to the sample surface (top). An AFM scanning result on a standard grid with 3-μm pitch and 100-nm-deep trenches (bottom left) and on filament actins (bottom right).

Reference

[1] T. El-Aguizy, J.H. Jeong, Y.B. Jeon, W.Z. Li, Z.F. Ren, and S.-G. Kim, "Transplanting carbon nanotubes," *Applied Physics Letters*, vol. 85, no. 25, pp. 5995-5597, Dec. 2004.

Surface Micromachining via Digital Patterning

E.W. Lam, J. Chen, V. Leblanc, V. Bulović, M.A. Schmidt
Sponsorship: DARPA, Hewlett-Packard

Conventional microelectromechanical systems (MEMS) fabrication relies heavily on the semiconductor manufacturing paradigm. While this model is well-suited for planar devices such as integrated circuits, it is drastically limited in the design and fabrication of three-dimensional devices such as MEMS. From a commercial viewpoint, this paradigm also poorly fits MEMS because the lower market demand makes it harder to offset the high production costs. Ridding MEMS fabrication of its reliance on such techniques may introduce several advantages, namely a wider base of substrate materials as well as decreased manufacturing costs.

Our project investigates severing MEMS fabrication from the traditional paradigm via digital patterning technologies. We have previously shown how MEMS can be used for the direct patterning of small molecular organics [1]. Using similar concepts, we have shown that surface micromachining can also be achieved.

In 2007-2008, we identified a viable material set for our surface micromachining process' sacrificial and structural layers: poly-methylmethacrylate (PMMA) and silver nanoparticles. To account for surface non-uniformity of the deposited PMMA, we employed solvent vapors to effectively lower the polymer's glass transition temperature and cause reflow at room temperatures [2]. To limit surface wetting and increase material loading of the silver nanoparticles, we deposited a PMMA reservoir to contain the silver nanoparticle solution (Figure 1). Free-standing cantilevers were fabricated (Figure 2), confirming that these techniques can be used for a surface micromachining process.

The next stage will be to fabricate additional MEMS structures and test the silver nanoparticle's mechanical properties. These properties will be used to design and fabricate a demonstration system based on our surface micromachining process. Subsequent stages will consist of creating a library of digital fabrication processes so that entire MEMS devices can be fabricated without the use of semiconductor manufacturing techniques.

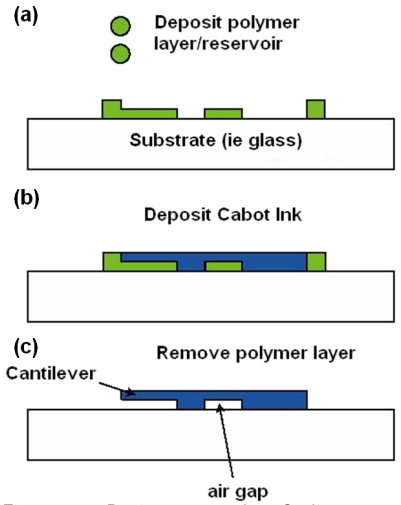

▲ Figure 1: Basic approach of direct surface micromachining. (a) PMMA layer (green) is deposited. (b) Metal silver ink (blue) is deposited and sintered. (c) PMMA is removed to release structure.

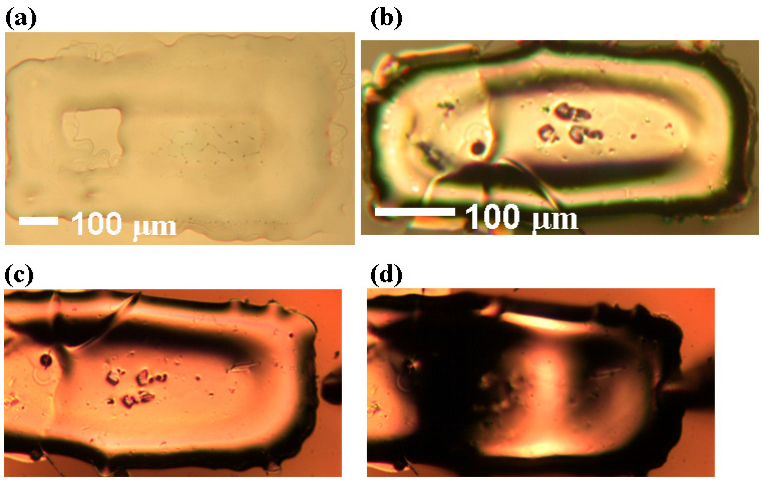

▲ Figure 2: Proof-of-concept displaying the feasibility of using the process for surface micromachining. (a-c) Pictures corresponding to the cartoons in Figure 1 which outline the fabrication process. (d) Cantilever being mechanically deflected by a probe, showing that the cantilever is free-standing.

References

[1] J. Chen, V. Leblanc, S.-H. Kang, M.A. Baldo, P.J. Benning, V. Bulović, and M.A. Schmidt, "Direct patterning of organics and metals using a micromachined printhead," in *Proc. MRS Spring 2005*, San Francisco, CA, Mar./Apr. 2005, pp. H1.8:1-7

[2] J. Feng, M. Winnik, R.R. Shivers, and B. Clubb, "Polymer blend latex films: morphology and transparency," *Macromolecules*, vol. 28, no. 23, pp. 7671-7682, Nov. 1995.

Vertical Growth of Individual CNTs/CNFs as Building Blocks for Functional Nano-devices

H.W. Lee, S. Kim, M. DeVolder, S.-G. Kim
Sponsorship: Intelligent Microsystems Center

We grow the vertically aligned single-strand CNT/CNF with the plasma-enhanced chemical vapor deposition (PECVD) machine we developed [1]. We found that ammonia (NH_3) gas etching is one of the key process parameters in growing vertically aligned CNTs/CNFs. The NH_3 gas etches Ni catalyst layers to form nanoscale islands while the NH_3 plasma etches deposited amorphous carbon.

A 30-nm-thick Ni layer is deposited on top of a 25-nm-thick titanium layer where CNT/CNF forest can grow vertically. For individual CNT/CNF growth at deterministic locations, 100~200-nm-sized nano dots were made by the E-beam lithography process (Raith, SEBL). The individual CNT/CNF growth requires shorter NH_3 etching time than is needed for a large-area forest growth. We obtained a well-grown array of vertically aligned individual CNTs/CNFs with 5~10 μm in length (Figure 1). High-resolution transmission electron microscopy (HRTEM) images show fishbone structures with multiple layers parallel to the etched surface of a Ni dot and the spacing between the layers is measured as 0.34 nm, which confirms that they are stacked graphene layers (Figure 2).

In this research, we obtained vertically aligned individual CNTs/CNFs on predefined location. We found that NH3 time in gas state is one of important parameters which affect in growing CNTs by PECVD. These individual CNTs/CNFs will be excellent candidates as building blocks for functional nano-devices such as an AFM tip, photovoltaic cell, super capacitor, and so on.

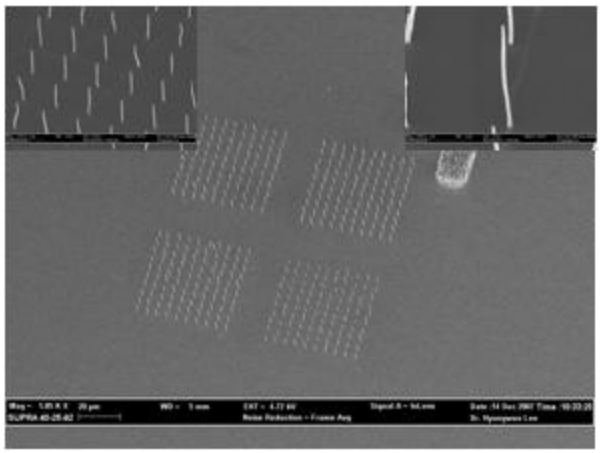

▲ Figure 1: Arrays of vertically aligned 5~10μm-long CNTs/CNFs grown from arrays of the Ni nano dots. The 5-μm spacing between the dots was predefined by electron beam lithography, and Ni dots were formed through heating to 580°C followed by introducing NH_3 gas for 5~10 minutes.

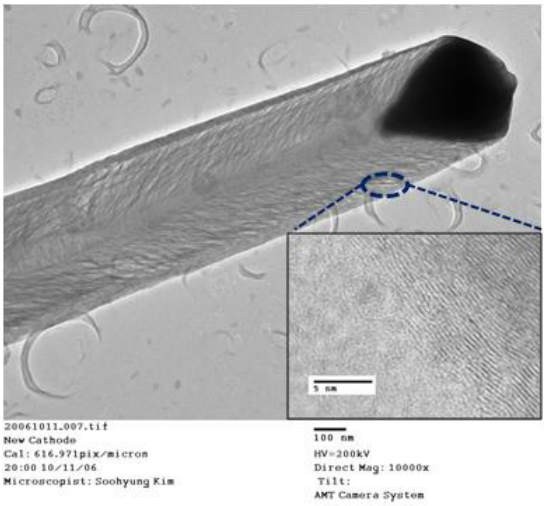

▲ Figure 2: An HRTEM image shows the internal fishbone structures with multiple graphene layers parallel to the outer surface. The spacing between the layers is 0.34 nm, as shown in the inset figure.

Reference

[1] C. Mueller-Falcke, S.D. Gouda, S. Kim, and S.-G. Kim, "A nanoscanning platform for bio-engineering: In-plane probe for switchable stiffness," *Nanotechnology*, vol. 17, pp. S69-S76, Jan. 2006.

High-pressure, High-temperature, Continuous Micro-flow Synthesis of Narrow Size-distribution Quantum Dots

S. Marre, J.Park, M.G. Bawendi, K.F. Jensen
Sponsorship: ISN, NSF

We have developed a high-pressure, high-temperature continuous-flow Silicon-Pyrex microreactor for the synthesis of CdSe quantum dots (QDs). The microreactor consists of a 400-µm-wide and 250-µm-deep channel with a 0.1- m-long mixing zone maintained at room temperature and a 1-m-long reaction zone heated up to 350°C. The two zones are separated by a thermally isolating halo etch that allowed for a temperature gradient of over 250°C. High-pressure modular compression fluidic connections are realized by compressing the microreactor between two stainless steel parts using silicone O-rings. In this configuration, the set-up allows reaching high pressure (up to 15 MPa) and temperature (up to 350 °C in the heated section). The entire set-up (Figure 1) is first pressurized from the inlet to the outlet using a pressurized nitrogen gas cylinder. Thereafter, the nitrogen valve is closed and the two precursor solutions are delivered independently using a high pressure syringe pump, insuring good control of the flow rate. Applying pressure allows the use of more conventional solvents like hexane, instead of high-boiling-point solvents (squalane) used previously [1]. One can even reach the low-viscosity supercritical fluid phase of hexane (T_c = 234.7 °C and p_c = 3.03 MPa, 20 < η < 70 µPa.s). In contrast to viscous single-phase flow reactors, the supercritical fluid flow approach enables narrow distribution of residence time, factors which have strong influence on the ultimate QD size distribution, as well as higher nucleation rates. Cadmium and selenium precursor solutions are delivered separately in the cooled mixing region and are thereafter allowed to react in the heated region. The use of supercritical hexane has a strong effect on the size distribution of the QDs and consequently the Full Width at Half Maximum (FWHM) of the emission peak (Figure 2). The size distribution for QDs synthesized in hexane, 4 - 5% (FWHM: 25 - 26 nm), is much smaller than for those synthesized in liquid squalane, 9 - 11% (FWHM: 45 - 49 nm).

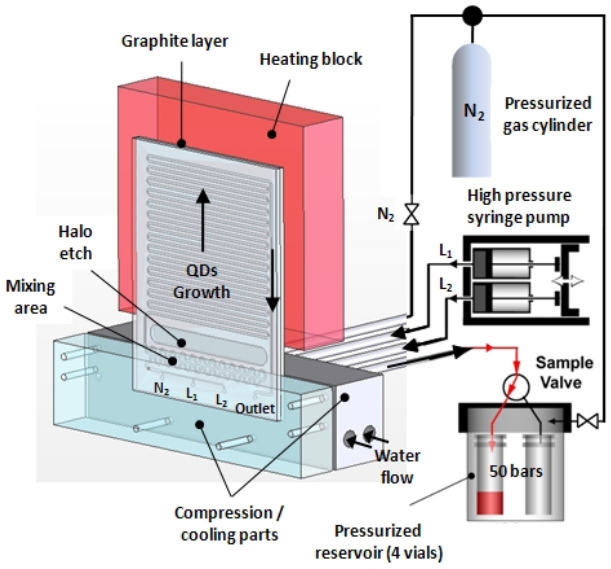

▲ Figure 1: Experimental set-up including a high pressure high temperature microreactor (Silicon – Pyrex), a compression-cooling aluminum part, a high-pressure syringe pump (Harvard Apparatus model: PHD 2000), 5-way high-pressure valve and a highpressure reservoir containing 4 vials.

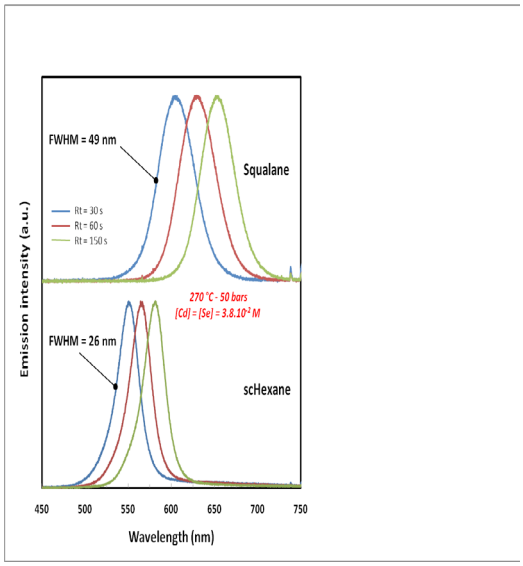

▲ Figure 2: The PL spectra at different residence times (Rt) obtained for CdSe QDs synthesized in Squalane and Hexane at 270 °C, 50 bars with [Cd] = [Se] = 3.8.10^{-2}M.

References

[1] B.K.H. Yen, A. Günther, M.A. Schmidt, K.F. Jensen, and M.G. Bawendi, "A microfabricated gas-liquid flow reactor for high-temperature synthesis: The case of CdSe quantums dots," *Angewandte Chemie, International Edition*, vol. 44, no. 34, pp. 5447-5451, Aug. 2005.

[2] B.K.H Yen, N.E. Stott, K.F. Jensen and M.G. Bawendi, "A continuous-flow microcapillary reactor for the preparation of a size series of CdSe nanocrystals," *Advanced Materials*, vol. 15, pp. 1858-1861, 2003.

[3] S. Marre, J. Park, J. Rempel, J. Guan, M.G. Bawendi, and K.F. Jensen, "Supercritical continuous-microflow synthesis of narrow size distribution quantum dots," *Advanced Materials*, to be published.

Modeling of Pattern Dependencies in Hot Embossing Processes

H. Taylor, D.S. Boning

Sponsorship: Singapore-MIT Alliance

The embossing of thermoplastic polymeric layers has proved to be both a lithographic technique with exceptional lateral resolution and a promising approach to high-volume microfabrication. Understanding of the mechanics of hot embossing is well developed thanks to experimentation and meticulous finite-element modeling [1], but it is not practicable to extend such approaches to the feature-rich embossed patterns of real devices. What is needed is a computationally efficient simulation technique that can predict the fidelity of an embossed topography, given an arbitrary stamp layout and a chosen embossing temperature, pressure, and loading duration. Previous attempts to develop efficient embossing simulators have modeled the polymer as a Newtonian fluid [2], an assumption that neglects the elasto-plastic and rubbery behavior that is present between the glass-transition and melting temperatures of popular embossing materials such as polymethylmethacrylate (PMMA).

We present a highly computationally efficient way of simulating the deformation of a polymeric layer when embossed with an arbitrarily patterned stamp [3]. Our approach takes a discretized stamp design and iteratively finds the distribution of stamp–polymer contact pressure that is consistent with the stamp's remaining rigid while the polymer deforms. We model the polymer in its rubbery regime as a perfectly elastic layer with a temperature-sensitive Young's modulus; we find the overall embossed topography by convolving the pressure distribution with the response of the polymeric surface to unit pressure applied in one cell of the discretized region. This topography is assumed to be "frozen" in place by cooling before unloading. The simulation is implemented in Matlab and the convolution uses Fast Fourier Transforms so that we can complete simulations containing ~10^6 elements within a few minutes using a standard desktop computer. We can additionally represent plastic flow of the polymer during embossing by scaling the point-load-response function and performing a time-stepped simulation.

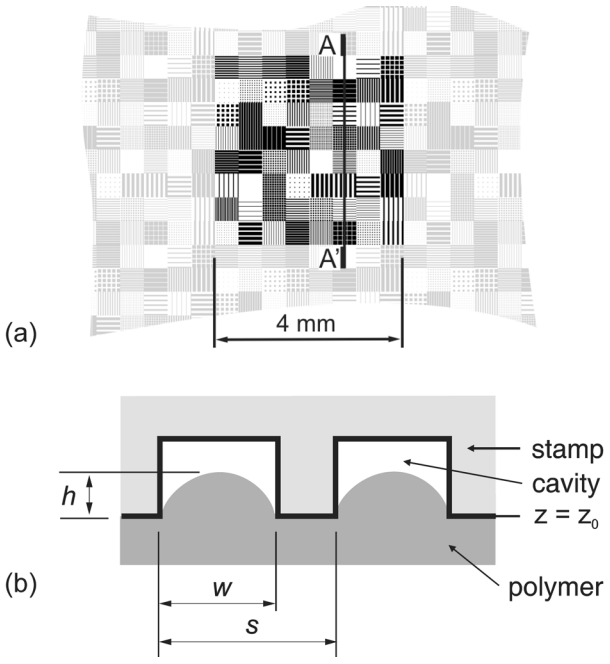

▲ Figure 1: (a) Embossing test pattern. Shaded features correspond to recesses in the silicon stamp. (b) Nomenclature of embossed features.

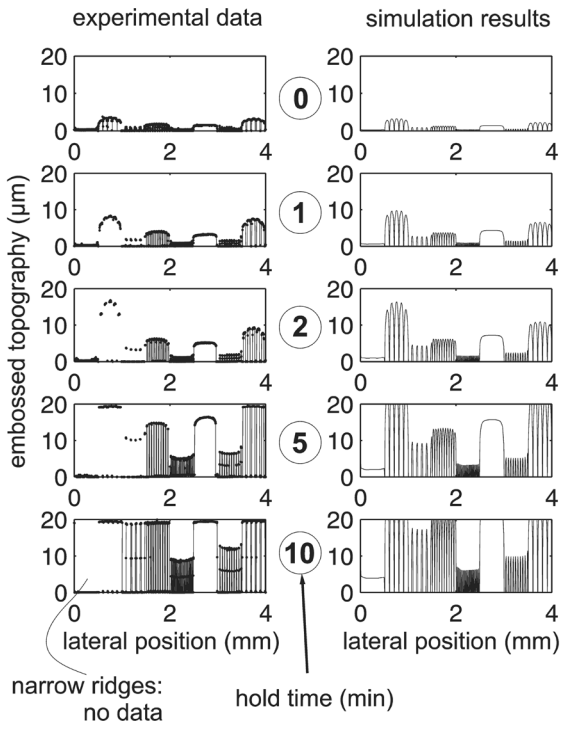

▲ Figure 2: Experimental and simulated topographies for the section A–A' shown in Figure 1a, after zero to ten minutes' loading duration at 110 °C and 8 MPa. Embossed material: PMMA.

References

[1] H.-C. Scheer, N. Bogdanski, M. Wissen, T. Konishi, and Y. Hirai, "Polymer time constants during low temperature nanoimprint lithography," *Journal of Vacuum Science and Technology B: Microelectronics and Nanometer Structures*, vol. 23, pp. 2963–2966, 2005.

[2] V. Sirotkin, A. Svintsov, H. Schift, and S. Zaitsev, "Coarse-grain method for modeling of stamp and substrate deformation in nanoimprint," *Microelectronic Engineering*, vol. 84, pp. 868–871, 2007.

[3] H. Taylor, D. Boning, B. Chen, and C. Iliescu, "Computationally efficient modeling of pattern dependencies in the micro-embossing of thermoplastic polymers," *Microelectronic Engineering*, DOI:10.1016/j.mee.2008.01.015, 2008.

Inexpensive Metrology Approaches for Process Variation in Polymeric MEMS

H. Taylor, Z. Xu, D.S. Boning
Sponsorship: Singapore-MIT Alliance

Polymeric materials, often inexpensive, tough and transparent, are attractive for manufacturing micro- and nano-fluidic devices. Here we describe three projects to develop tools for monitoring polymeric microstructure production. The first uses diffraction to identify dimensional defects in embossed thermoplastic components. A collimated laser beam is shone through a component whose microembossed structure includes a specially designed holographic test pattern that spatially modulates the phase of the transmitted light (Figure 1). A far-field diffraction pattern is formed, yielding information about the embossed topography without requiring precise alignment of, or contact with, the manufactured part [1].

The second project uses moiré interference to study distortions of hot-embossed polymeric substrates. The only apparatus required is a desktop image scanner and a precisely printed reference grid. The reference grid and a substrate embossed with a grid of the same target pitch are placed on the scanner and rotated by hand until moiré fringes are seen. At least two scans are made, each with a different relative reference–part rotation. These rotations are extracted from the images and, together with the moiré fringes' orientations and spacings, reveal the part's distortions.

Thirdly, we are designing a way of testing the toughness of bonds between polymeric layers. The UV/ozone- and plasma-activated bonding of polymeric layers is appealing because, unlike with thermal fusion bonding, microstructures at the interface remain intact [2]. However, the lack of a simple bond test method has impeded the development of these processes. Our approach is to pattern one of the layers with one or more steps to ~1 μm deep. The bonding process is then performed and, immediately after bonding, the layers peel apart locally around each step (Figure 2). The lengths of the resulting cracks are measured with optical microscopy, revealing the bond's toughness. Interfacial cracks are usually shorter than a millimeter, meaning that these test structures can be interspersed with functional devices.

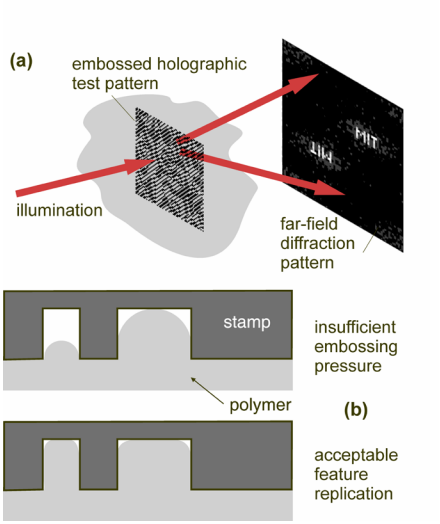

▲ Figure 1: Use of holographic test patterns for contact-free determination of dimensional defects in embossed parts. (a) Overview of scheme: a dedicated test pattern embossed alongside the functional device perturbs the phase of transmitted light, imparting information about the topography. (b) Cross-sections of typical embossed topographies that would need to be distinguished: inadequate embossing pressure would cause different elements of the hologram to be filled to different heights, thereby perturbing phase differently.

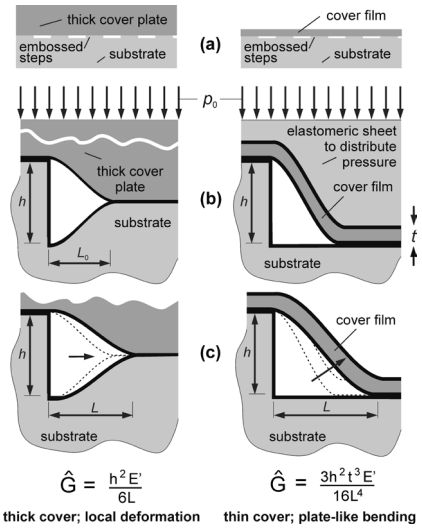

▲ Figure 2: Two configurations of the bonding test method. On the left, both layers are substantially thicker than the length L of the crack, and material deforms locally around the step. On the right, one layer is a film that bends over the step as a plate. (a) Several steps in cross-section. (b) During bonding, pressure p_0 is applied, causing the layers to compress and a bond to form where the layers make contact. In (c), the bonding pressure is released and the cracks extend to an equilibrium length yielding an estimate, $\hat{G}$, of the bond toughness. E' is the plate modulus.

References

[1] H.K. Taylor and D.S. Boning, "Diffraction-based approaches to the *in-situ* measurement of dimensional variations in components produced by thermoplastic micro- and nano-embossing," in *Proc. International Symposium on Nanomanufacturing*, Singapore, Jan. 2008.

[2] A. Bhattacharyya and C.M. Clapperich, "Mechanical and chemical analysis of plasma and ultraviolet–ozone surface treatments for thermal bonding of polymeric microfluidic devices," *Lab on a Chip*, vol. 7, pp. 876–882, 2007.

Relationship between Pad Properties and CMP Planarization

W. Fan, D.S. Boning

Sponsorship: SRC/SEMATECH Engineering Research Center for Environmentally Benign Semiconductor Manufacturing, JSR Micro

Chemical mechanical polishing (CMP) is a key technology in semiconductor and micromachining processes. In previous work, our group proposed semi-empirical and physically-based die-level CMP models to understand and optimize the dielectric planarization process [1]. In this work, we seek to understand how planarization model parameters relate to specific pad properties. In particular, we are interested in how pad bulk stiffness and pad surface properties affect both within-chip planarization and step-height reduction or planarization efficiency.

Our recent work has investigated pad hardness effects on polishing performance by fitting experimental data from the polishing of patterned wafers and by extracting model parameters related to effective pad Young's modulus and height distribution of surface asperities. We polished wafers with the same pattern-density arrays and the same initial oxide thickness using four pads with different hardness (standard, high, low and very low), and measured the oxide thickness and step-height evolution during the process.

From the data fitting and model prediction, we conclude that the standard hardness pad achieves faster planarization and has better linear step-height removal for a longer time than the other pads, as shown in Figure 1. All pads have a pattern-density dependency effect; however, the stiffer pads show less oxide thickness variation across the chip. Figure 2 shows the evolution of step height at the test point on a 50% pattern density array boundary next to a 10% layout pattern density area. This edge planarizes faster than the array center point because of the lower effective pattern density. We also see that the very low hardness pad has substantially different step-height removal behavior than the other pads, indicating that the pad surface asperity height distribution may be substantially different for this pad. Current work is seeking to make direct pad physical measurements in order to verify the relationship between both pad surface (asperities) and bulk effective modulus and the resulting planarization performance.

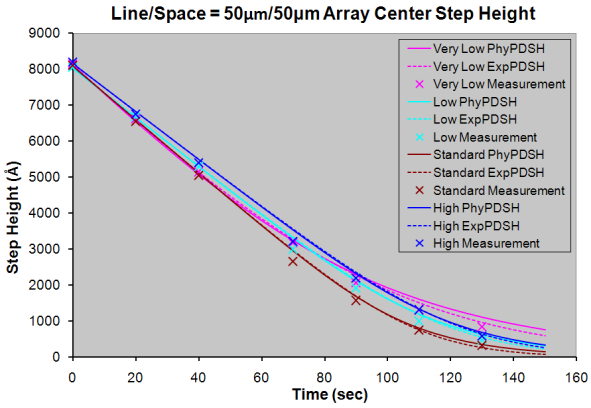

▲ Figure 1: Step height evolution for different pad hardness at the center test point of a 50% pattern density array in the middle region of the wafer. Data points show optical measurements. The line shows physically-based pattern-density/step-height (PDSH) model prediction. Dashed line shows exponential PDSH model prediction.

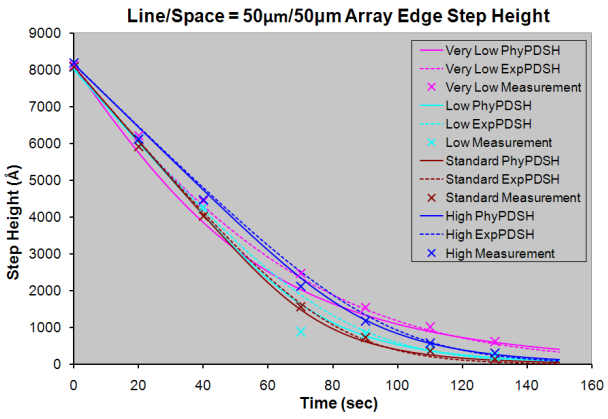

▲ Figure 2: Step-height evolution for different pad hardness at the edge test point of 50% pattern density array in the middle region of the wafer. Data points show optical measurements. Line shows physically-based PDSH model prediction. Dashed line shows exponential PDSH model prediction.

Reference

[1] X. Xie, "Physical understanding and modeling of chemical mechanical planarization in dielectric materials," Ph.D. thesis, Massachusetts Institute of Technology, Cambridge, 2007.

Cascaded Mechanical Alignment for 3D MEMS Assembly

N.S. Shaar, G. Barbastathis, C. Livermore
Sponsorship: ISN

The fabrication of MEMS devices relies, for the most part, on tools and processes developed originally for the fabrication of electronic chips in the IC industry. However, in contrast to electrical circuits, functional micro-electro-mechanical systems need features that are three-dimensional (3D) in structure. To capitalize on the well-developed techniques and equipment of 2D-patterning technologies, we have developed a method to create 3D MEMS devices by folding, aligning and latching 2D micro-fabricated films.

The folding process is relatively well developed. Various methods for bending films out-of-plane have been demonstrated, including thermal contraction [1], stress gradients [2], surface tension [3], and external magnetic forces [4]. However, aligning the folded segments and latching them, while maintaining the structural integrity of the MEMS devices, remain challenges.

We have designed, fabricated, and tested a mechanical alignment mechanism that enables the precise angular positioning of 2D membranes to form 3D structures. The alignment system is based on a cascaded set of triangular protrusions on the *target segment* and rhombic holes on its corresponding *aligning segment*. Upon folding, the protrusion-hole pairs start to engage sequentially, starting with the pair closest to the fold. The alignment progresses in a zipper-like manner, allowing a large range of correction as well as high alignment accuracy (Figure 2). We have demonstrated our alignment mechanism by assembling a corner-cube retro reflector. The alignment system's accuracy was within 16 mrad and the measured range of correction was 0.38 rad [5]. We have also demonstrated the ability to simultaneously align multiple segments at different angles (Figure 2).

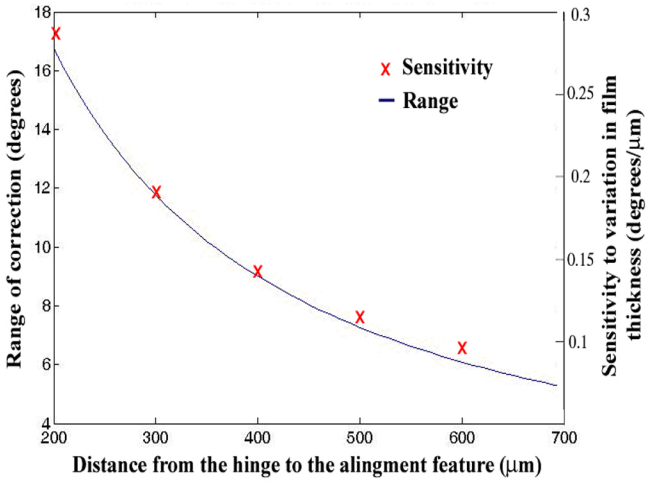

▲ Figure 1: Plot of the predicted range of correction (solid line) and the sensitivity of the alignment to variations in the film thickness ('x' data points) vs. distance from the hinge to the alignment feature.

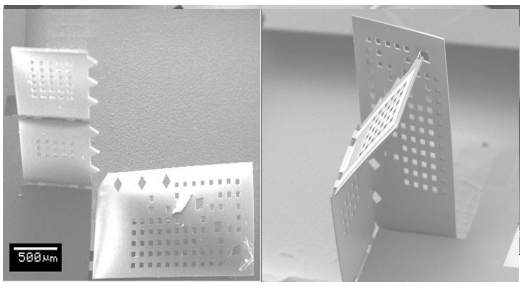

▲ Figure 2: Corner-cube with a base segment fixed to the substrate and two folded segments aligned at 90^0 (top). A sequence of two folded *target segments* aligned by one *aligning segment* to 90° and 45° relative to the substrate surface (bottom).

References

[1] T. Ebefors, E. Kälvesten, and G. Stemme, "New small radius joints based on thermal shrinkage of polyimide in V-grooves for robust Self-assembly 3D microstructures," *Journal of Micromechanical Microengineering*, vol. 8, pp. 188–194, 1988.

[2] W.J. Arora, A.J. Nichol, H.I. Smith, and G. Barbastathis. "Membrane folding to achieve three-dimensional nanostructures: Nanopatterned silicon nitride folded with stressed chromium hinges," *Applied Physics Letters*, vol. 88, no. 5, pp. 053108:1-3, Jan. 2006.

[3] Y.K. Hong, R.R.A. Syms, K.S.J. Pister, and L.X. Zhou. "Design, fabrication and test of self-assembled optical corner cube reflectors," *Journal of Micromechanical Microengineering*, vol. 15, pp. 663-672, 2005.

[4] H.J. In, W. Arora, T. Buchner, S.M. Jurga, H.I. Smith, and G. Barbasathis, "The nanostructured Origami™ 3D fabrication and assembly process for nanomanufacturing," in *Proc. Fourth IEEE Conference on Nanotechnology*, Munich, Germany, Aug. 2004, pp. 358-360.

[5] N.S. Shaar, G. Barbastathis, and C. Livermore, "Cascaded mechanical alignment for assembling 3D MEMS," in *Proc. 21st IEEE International Conference on Microelectomechanical Systems*, Tucson, AZ, Jan. 2008, pp. 1064-1068.

Direct Printing of PZT Thin Films for MEMS

S. Bathurst, H.W. Lee, S.-G. Kim
Sponsorship: DARPA Grant HR0011-06-1-0045, Hewlett-Packard

In 2007-2008, we reported a new method for depositing piezoelectric thin films via thermal ink jet (TIJ) printing of a modified PZT sol-gel [1]. Direct printing of lead zirconate titanate (PZT) thin films eliminates the need for photolithographic patterning and etching, allows for controlled deposition over non-planar topographies, and enables the deposition of films with varied thickness. We developed conditions of deposition and crystallization for high-quality PZT thin films via thermal inkjet printing, including solution chemistry, printing conditions, and thermal processing parameters. The inks developed for this work were based on a commercially available PZT sol gel. Dilution of the sol is required to control the evaporation rate and characteristic dimensionless numbers of the ink, and our work included a jetability study of various solution chemistries. This study resulted in an ink that can be jetted reliably and is made up of 50% isopropanol, 30% 2-methoxyethanol, %15 A6 sol-gel, and 5% ethylhexanoic acid. This work also investigated factors that control the droplet size and the contact angle of the PZT ink deposited on a Pt substrate. The edge roughness of deposited lines was controlled to +/- 10μm. We further investigated the effect of droplet size, spacing, ink boiling point and substrate temperature on the deposited film uniformity. Figure 1 demonstrates the effect of substrate temperature on the film topography. Films between 100-500nm in thickness with a variation of less than 40nm were produced (Figure 1b). A capacitor test device was fabricated with approximately 400 nm of printed PZT between two platinum electrodes. The bottom electrode was 200 nm Pt/20nm Ti/200 nm SiO_2/Si. The capacitor area was $6.25 \cdot 10^{-4}$ cm². Finally, it was determined that the modified ink requires a prolonged drying step to remove added solvents, and pre-dryed films showed a drastically improved polarization performance (Figure 2).

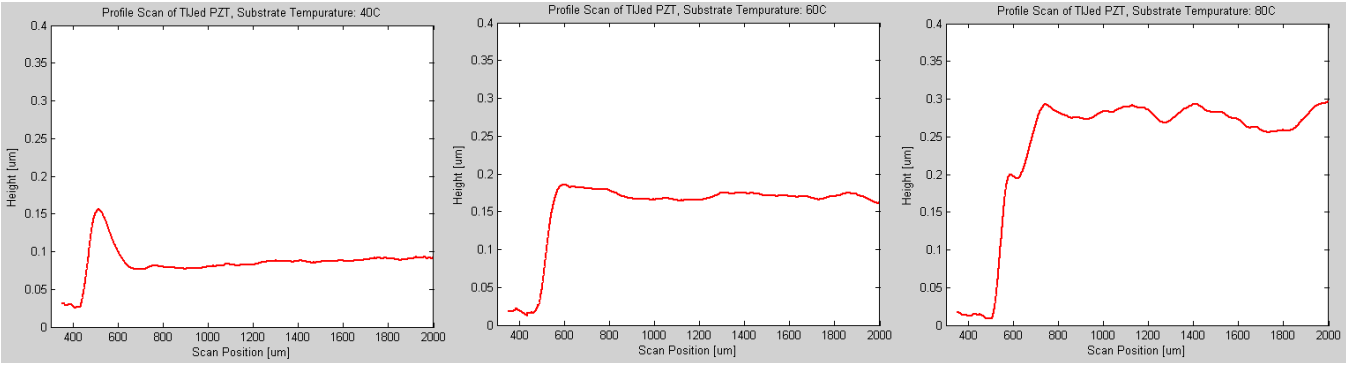

▲ Figure 1: Profilometry of thermal ink jetted PZT, deposited at different substrate temperatures. Ink composition: 6% EHA, 15% PZT sol-gel, 50% IPA, and 29% ME.

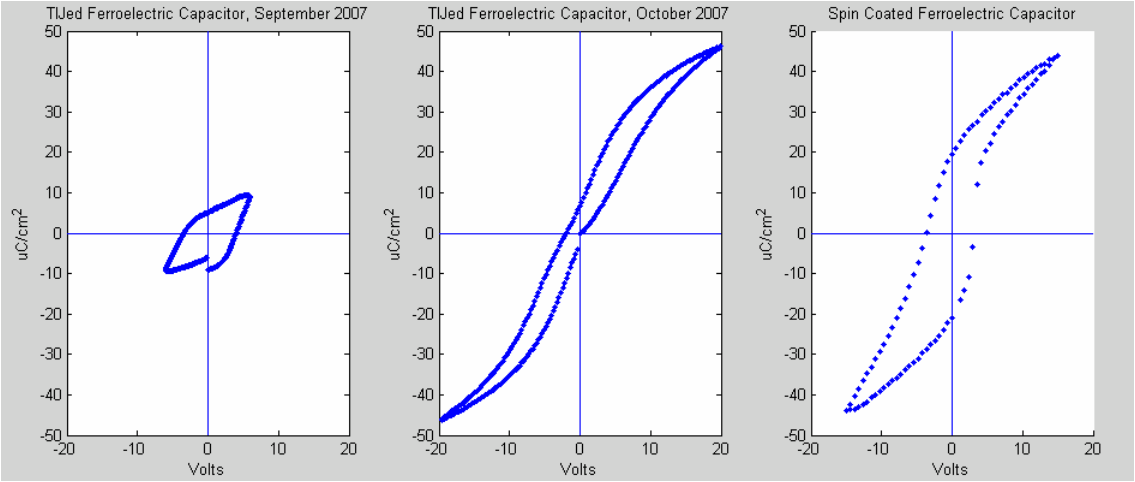

▲ Figure 2: Polarization vs. voltage hysteresis curve for a thermal ink jetted PZT thin film a) after standard pyrolysis and b) after extended pyrolysis as well as c) for a spincoated film after standard pyrolysis.

Reference

[1] S. Bathurst, H.W. Lee, and S.-G. Kim, "Direct printing of lead zirconate titanate thin films," *IEEE MEMS 2008*, Tucson, AZ, 2008.

Printable Microfluidic Valves Composed of Thermosensitive Hydrogels

N.E. Reticker-Flynn, H.W. Lee, S.-G. Kim
Sponsorship: Hewlett-Packard, DARPA

A method for fabricating compact microfluidic valves using thermal inkjet printing is presented. Poly(N-isopropylacrylamide) (poly(NIPAAm)) is a temperature-sensitive hydrogel that shrinks when heated above a Lower Critical Solution Temperature (LCST) (~32°C). With the swelling behavior of poly(NIPAAm) as a flow control mechanism, a compact microfluidic valve has been designed and fabricated. The proposed valve provides a series of benefits over conventional microfluidic valves such as the "Quake" valves [1], in that they allow for the use of single-layer PDMS microchannels. Additionally, the need for a bulky external pump is eliminated by localized electromagnetic heating if the hydrogel valve.

The design of the proposed valve is composed of an SU-8 microwell into which the prepolymer NIPAAm solution is printed (Figure 1). The well contains micro-anchors to ensure that the hydrogel always shrinks downward in order to prevent any unintended blocking of the flow channel. After the prepolymer solution with photoinitiators has been printed into the wells, it is polymerized using ultraviolet light. Finally, the PDMS channel is placed above the well. This channel contains discontinuities at the location of the valves, which block the flow when the hydrogel is in a swollen state. When the poly(NIPAAm) valves are heated above the LCST, the hydrogel plug shrinks and allows flow (Figure 2). The amount by which the gel plug shrinks depends on monomer concentration and UV exposure energy. By fabricating the wells on a separate substrate from the channels, users can use the same valve substrate with a variety of different fluidic circuit designs. Device geometry was chosen using CFD to minimize pressure drops across the valve.

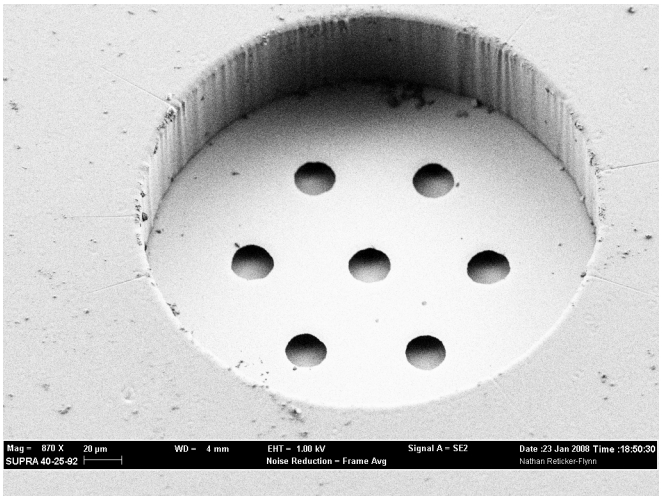

▲ Figure 1: An SEM of a microwell prior to printing NIPAAm prepolymer. The bottom of the well is composed of a metal layer with anchor holes. The underlying pyrex has been etched isotropically with HF to generate significant undercut.

▲ Figure 2: Surface profile of the swollen and shrunken poly(NIPAAm) gel after printing into a 500-µm-diameter well and prior to bonding of PDMS. The heated gel provides an average height difference between the gel surface and the top of the microwell of approximately 35 µm.

Reference

[1] T. Thorsen, S. Maerkl and S. Quake, "Microfluidic large-scale integration," *Science*, vol. 298, pp. 580-584, Oct. 2002.

Integration of Printed Devices and MEMS

H. Li, M.A. Schmidt

Sponsorship: DARPA, Hewlett-Packard

As part of an overall effort on Non-Lithographic Technologies for MEMS and NEMS, we are developing processes for the integration of printed MEMS and devices. The goal of this project is to demonstrate the power of a printed technology for microsystems. We have already developed a surface micromachined cantilever technology that utilizes silver as a structural material and a novel organic spacer. Further, we have developed a family of both inorganic and organic devices that can ultimately be printed. As an initial demonstration, we are building a MEMS capacitive accelerometer that integrates the silver surface micromachined proof mass and spring with a capacitive sense circuit fabricated using organic FETs.

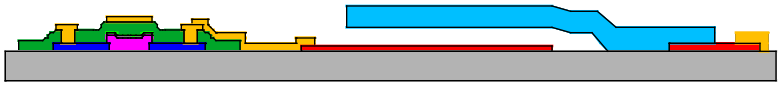

▲ Figure 1: Schematic illustration of the integration of a printed MEMS cantilever with a printed electronic device.

The MIT-OSU-HP Focus Center on Non-lithographic Technologies for MEMS and NEMS

M.A. Schmidt (in coll. with S.-G. Kim, C.G. Sodini, V. Bulović, MIT; D. Keszler, J. Wager, OSU; P. Benning, M. Chaparala, J. Stasiak, Hewlett-Packard)

Sponsorship: DARPA, Hewlett-Packard

This center is part of a set of centers on MEMS/NEMS fundamentals supported by DARPA. The MIT-OSU-HP Focus Center aims to develop new methods for fabrication of MEMS and NEMS that do not use conventional lithographic techniques. The Center leverages the leading expertise of MIT and OSU in MEMS and printed devices, with the printing expertise of HP. The Focus Center is organized into four primary areas: tools, materials and devices, circuits, and demonstration systems.

In the area of tools, we are leveraging the existing thermal inkjet (TIJ) technology of HP and augmenting it with specific additional features, which expand the palette of available materials for printing. We are developing materials and devices over a broad spectrum from active materials and photonic and electronic materials to mechanical materials. In the circuits area, we are studying the behavior of the devices that can be realized in this technology with the goal of developing novel circuit architectures. Lastly, we intend to build several "demonstration" systems that effectively communicate the power of the new technologies that will emerge from this center. In the past year, the center has succeeded in demonstrating a number of the key "building blocks" for a fully printed system. Specifically, we have created printed transistors, printed optical elements (light emitters and photodetectors), printed active materials (piezoelectrics), and a printed MEMS structure (micro-cantilever). Looking forward, we will begin efforts to integrate some of these building blocks.

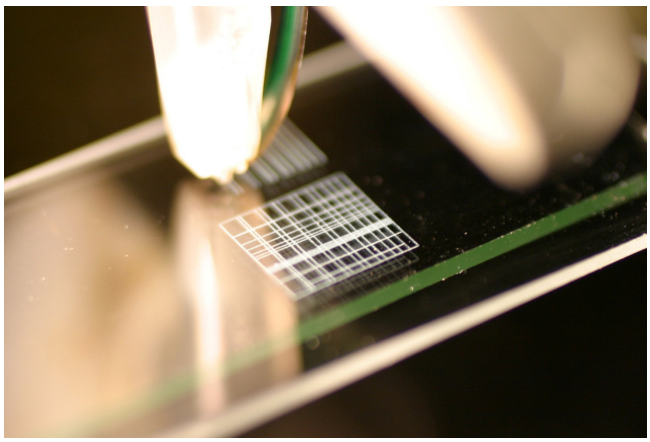

▲ Figure 1: Printing the structural layer of a MEMS cantilever. The printing is performed using a modified thermal inkjet system.

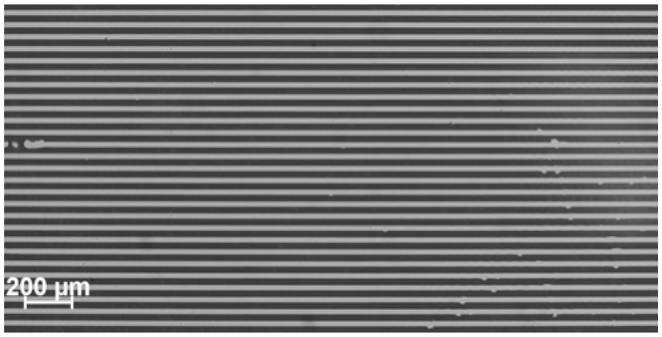

▲ Figure 2: In addition to printing by inkjet, we also explore micro-contact printing. The image shown is an illustration of the micro-contact printing of metal lines from the Bulović group at MIT.

Inkjet-printed Quantum Dot and Polymer Composites for AC-driven Electroluminescent Devices

V. Wood, J. Chen, M.J. Panzer, M.S. Bradley, J.E. Halpert, M.G. Bawendi, V. Bulović

Sponsorship: ISN, PECASE, NDSEG

We introduce a technique for the reliable deposition of intricate, multicolored patterns using a quantum dot (QD) and polymer composite and demonstrate its application for robust AC-driven displays with high brightness and saturated colors. The AC electroluminescent (AC EL) devices are a well-established technology [1]. Their relatively simple fabrication and long operating lifetimes make them desirable for large-area displays; however, a major challenge with AC EL remains finding efficient and stable red phosphors for multicolored displays. Colloidally synthesized QDs are robust, solution-processable lumophores offering tunable and narrowband photoluminescence across the visible spectrum [2]. By integrating QDs into an AC EL device, we demonstrate patterning of saturated red, green, and blue pixels that operate at video brightness.

The concept behind the device operation is optical downconversion: red and green QDs absorb blue electroluminescence from phosphor grains and then emit at longer wavelengths. The device, pictured schematically in Figure 1, is fabricated with a layer-by-layer approach that is compatible with flexible substrates. A QD and polyisobutylene (PIB) solution is printed on conductive indium tin oxide (ITO) using a Hewlett Packard Thermal Inkjet Pico-fluidic dispensing system (TIPs). Figure 2a shows examples of the intricate and multicolored patterns possible. The electroluminescent phosphor paste (ZnS:Cu powder in a transparent binder from Osram-Sylvania) is deposited uniformly over the sample using a disposable mask and doctor-blading to define the device area. Top contacts are made with conductive tape from 3M. This basic device structure is assembled and tested entirely under atmospheric conditions.

When an AC voltage waveform is applied across the device, we measure spectrally pure QD emission in the red and green and ~100 Cd/m^2 brightness. Photographs of the red, green, and blue pixels of a working, AC-driven device appear in Figure 2b. The Commission International d'Eclairage (CIE) coordinates of the pixels device define a color triangle that is comparable to the International Telecommunication Union HDTV standard.

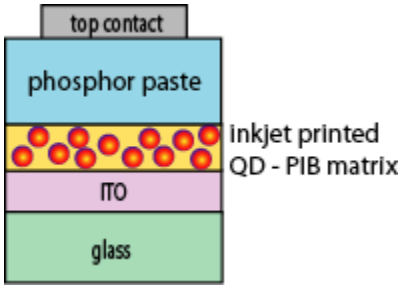

▲ Figure 1: Schematic showing basic device structure.

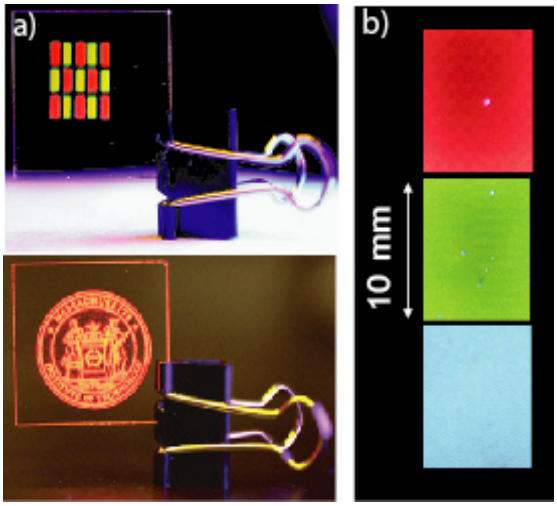

▲ Figure 2: Photographs of a) photoluminescence of QD-PIB composites inkjet-printed on 1 in. x 1 in. indium tin oxide coated glass slides and b) emission from blue, green, and red pixels of completed devices driven at 70 V_{rms} and 50 kHz.

References

[1] Y.A. Ono, *Electroluminescent Displays.* Singapore: World Scientific, 2000.

[2] C.B. Murray, D.J. Norris, and M.G. Bawendi, "Synthesis and characterization of nearly monodispersed CdE (E= S, Se, Te) semiconductor nanocrystallites," *Journal of the American Chemical Society*, vol. 115, pp. 8706-8715, 1993.

Milli-watt Energy-harvesting from Low-frequency Vibrations

S.C. Chang, A.D. Dominguez-Garcia, D. Otten, J.H. Lang
Sponsorship: DARPA

This project is part of the Hybrid Insect Microelectromechanical System MEMS (HI-MEMS) program sponsored by the Defense Advanced Research Projects Agency (DARPA). The main objective of this program is to establish the interface between adult neural systems and appropriate computational and MEMS systems. Here, insects are the first test bed, and they will be directed to fly to specific locations in real time via remote control. In order to support the flight-control systems, a local energy-harvesting power system is required on the moth. The energy-harvesting system has two ports: the mechanical port and the electrical port. Mechanical power is input from moth motion at the mechanical port, and electrical power is output for general consumption at the electrical port. Internal to the harvester between the two ports are an electromechanical energy converter (generator) and the power electronics. In the past 12 months, a 0.1-mW bench-top electromechanical energy converter, which extracts power from low-frequency vibration, was designed and fabricated. Figure 1 shows the harvester.

The electromechanical energy converter has two major components: a resonator with moving magnets and a coil. The magnets serve as a proof mass, and as the resonator vibrates, the magnets sweep past coils through which power will be harvested. In collaboration with the Daniel Group at the University of Washington, we determined the resonating frequency to be 25 Hz by tracking the three-dimensional inertial motion of a moth and taking the Fourier transform of the moth's motion. Figure 2 shows a snapshot of the moth carrying a resonator during flight. The coils are wound on a plexiglass form, such as that shown in Figure 1; future flight-qualified windings will be made with flexible printed-circuit technology. The electromechanical energy converter was tested on a shaker table, which simulates the vibration of a moth, and 0.1 mW of time average power was extracted from the output of the series coil connection.

We are now optimizing a more compact advanced energy-harvester that has flexible printed-circuit windings, neodymium iron boron magnets. Simulations indicate that 1-mW energyharvesting is achievable at a cost of 0.27g. Harvester components including the magnets and windings have been designed and are under fabrication. Currently, we are beginning the analysis and design of the power electronic circuit. The first pass will focus on switched-capacitor power electronics, and the next milestone will be testing the advanced energy-harvester on a shaker table and developing power electronics compatible with radio micro- fabrication.

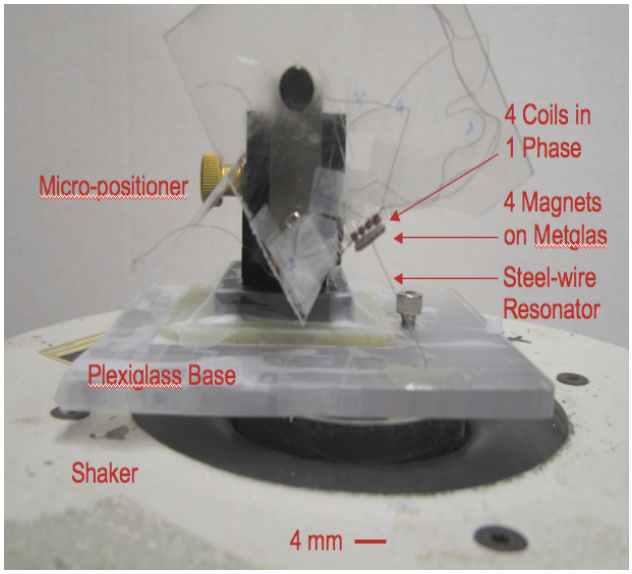

▲ Figure 1: First generation energy-harvester system consisting of 4 magnets and 4 coils in phase on a shaker table capable of generating 0.1mW of power.

▲ Figure 2: A moth carrying a resonator during flight. The fine-tuned resonator will resonate with the moth's vibration frequency of 25 Hz, creating maximum swing amplitude to generate power. (Courtesy of Daniel Group at the University of Washington.)